STREST

D 4.2

DELIVERABLE

PROJECT INFORMATION

Project Title:	**Harmonized approach to stress tests for critical infrastructures against natural hazards**
Acronym:	**STREST**
Project N°:	603389
Call N°:	FP7-ENV-2013-two-stage
Project start:	01 October 2013
Duration:	36 months

DELIVERABLE INFORMATION

Deliverable Title:	**Guidelines for performance and consequences assessment of geographically distributed, non-nuclear critical infrastructures exposed to multiple natural hazards**
Date of issue:	31 September 2015
Work Package:	WP4 – Vulnerability models for the performance and consequences assessment in stress tests of CIs
Editor/Author:	AUTH (Aristotle University of Thessaloniki)
Reviewer:	Matjaž Dolšek (University of Ljubljana)

REVISION: Final

Abstract

Under the framework of the STREST project, the main objective of Task 4.2 is to provide general guidance for performance, loss and consequence assessment of geographically distributed, non-nuclear CIs exposed to multiple natural hazards. To accomplish this, quantitative and standardized procedures and tools for consequence analysis of geographically distributed, non-nuclear CIs exposed to multiple natural hazards are presented while the potential interdependencies in this CI class are investigated in one of the cases (CI-B3 Port Infrastructures of Thessaloniki). In this context, hazard, vulnerability, risk (and multi-risk), interdependencies, resilience and uncertainty issues are addressed. The aim is to contribute, eventually, to the definition of stress tests at a regional scale, accounting also for the consequences of cascading failures. The description of the tools developed and the guidance axis are provided through three selected case studies of geographically distributed CIs, i.e. CI-B1: Major Hydrocarbon Pipelines in Turkey, CI-B2: Gasunie National Gas Storage and Distribution Network in Holland and CI-B3: Port Infrastructures of Thessaloniki in Greece. Thus, apart from general considerations, specifications are provided for each one of them. Finally, a conceptual framework on factors influencing the resilience of geographically distributed CIs is developed and applied in the case of Port Infrastructures of Thessaloniki in Greece.

Keywords: Earthquake, Tsunami, Fault Rupture, Pipelines, Ports, Fragility Models, Vulnerability, Multi-Hazard, Performance Assessment, Uncertainties, Multi-risk, Critical Infrastructures

Acknowledgments

Deliverable Contributors

AUTH	Kalliopi Kakderi
	Stavroula Fotopoulou
	Sotiris Argyroudis
	Stella Karafagka
	Kyriazis Pitilakis
	Anastasios Anastasiadis
	Chiara Smerzini
INGV	Jacopo Selva
JRC	Georgios Giannopoulos
	Luca Galbusera
TNO	Wim Courage
	Johan Reinders
KOERI	Yin Cheng
	Sinan Akkar
	Mustafa Erdik
	Eren Uckan

Table of Contents

List of Figures

List of Tables

1   Introduction

The degree to which our society depends upon the reliable functioning of infrastructural systems is underlined by the ubiquitous term critical infrastructures (CI) with which this set of interconnected systems is indicated (PCCIP, 1997). Critical Infrastructures (CIs) are complex systems composed by many components, which are physically and/or functionally dependent to each other and/or on external supplies. In a complex system, elements are so interconnected and their relationship so multifaceted that their properties cannot be properly understood without assessing their interrelationship with each other as well as their relationship with the wider system and its environment. In this case, the performance of the infrastructure as a whole should be addressed.

Moreover, the hazard assessment of spatially distributed systems with various typologies differs from the point like hazard assessment. If CIs' components are geographically distributed, during the same event, different hazard intensities may be experienced at the different locations where components are located. Thus, in order to achieve realistic distributions of damages, it is necessary to model the potential spatial correlations of the hazard intensities.

Given the spatial extent and the importance of these infrastructures, subjected in many cases to a combination of natural hazards, namely earthquakes, volcanic eruptions, landslides, tsunamis, river floods, wildfires, winter storms, and in some cases to fluvial and coastal flooding the multi risk approach is obligatory. In both their occurrence and their consequences, different hazards are often causally related. Classes of interaction include triggered events, cascade effects and the increase in vulnerability during successive hazards.

The aim of this report is to provide a general guidance paradigm for risk, performance and consequence assessment of geographically distributed, non-nuclear CIs exposed to multiple natural hazards. The paradigm is developed through three case studies of geographically distributed CIs (i.e., STREST CI class B), which are CI-B1: Major Hydrocarbon Pipelines in Turkey, CI-B2: Gasunie National Gas Storage and Distribution Network in Holland and CI-B3: Port Infrastructures of Thessaloniki in Greece. For this, several scientific domains must be encompassed in order to describe the different components and parameters of the problem and provide the basis of the guidance paradigm. Adequate approaches for hazard, vulnerability, risk, interdependencies, resilience and uncertainty should all be adopted in a multi-level framework, in particular for the above geographically distributed CIs.

In the subsequent chapters, apart from general considerations, specifications for potential guidance are provided for each one of them as well. In particular, after few examples of critical infrastructures performance and consequences from past events (Chapter 2), the three representative case studies of geographically distributed CIs examined in the framework of STREST are shortly described in Chapter 3 and their specific features are provided; these will be the basis for the selection of suitable methods to deal with their performance assessment under multiple-hazards. In Chapter 4, hazard assessment methods in a multi-risk environment are specified for the case of geographically distributed systems. Specific methods are proposed in order to provide the seismic input for the fragility models of the vulnerable elements of each infrastructure in a complex interconnected

system of infrastructures, as well as the seismic hazard scenarios for geographically distributed systems. Regarding the vulnerability models used in order to assess the potential physical damages of the components of the systems, a comprehensive review of fragility functions for the most important components of the selected geographically distributed CIs is carried out in Chapter 5 as guidance for the selection of the most appropriate function for the case at hand. New fragility curves are developed where necessary, considering the distinctive features of the selected CIs.

To assess the vulnerability at system level, specific methods for the performance and loss assessment of complex geographically distributed CIs accounting for interdependencies should be used. Specifications on performance and loss assessment for the three spatially distributed CIs are provided in Chapter 6. The challenging issues of loss propagation and cascading effects and multiple hazard loss assessment comprise relatively recent research fields. Provided guidance is mostly built on previous studies and methodologies (Chapter 6). Sequentially, a conceptual framework on factors influencing the resilience of CIs is described in Chapter 7. Focus is given in the evaluation of restorative capacity, and an application of the proposed methodology is demonstrated for the port infrastructures in Thessaloniki based on a recovery scenario after an earthquake event. An interface (GRRASP) for computation and visualization of results is introduced. Finally, a specific procedure to deal with the treatment of epistemic uncertainty at all ST-levels is proposed within STREST (Chapter 8).

It should be noted, that previous knowledge (mainly from completed and on-going research projects) is being exploited and in several cases used as a basis for the development of the Stress Test (ST) methodology within STREST. A strategic selection of projects and know-how that can potentially be transferred from those projects (GEISER, MATRIX, NERA, REAKT, SHARE, SYNER-G) to the STREST project is presented in Deliverable D2.4 "Report on lessons learned from on-going and completed EU projects" (Mignan et al., 2014a). In the following chapters, where the several aspects covering the performance and consequences assessment of geographically distributed, non-nuclear CIs exposed to multiple natural hazards are being presented, reference to past studies/methodologies is made in several cases, and proposals are based on previous research results, after verification and/or testing. In other cases, new methods are developed; while in few aspects of this multi-faced problem available data and desired level of the results' accuracy is the determinant for the selection of the adopted methodology.

2 Examples of critical infrastructures performance and consequences from past events

CIs constitute the backbone of modern society, as they provide essential services, e.g. electrical power, telecommunications, water, etc. Recent events impacting CIs have drawn attention to the vulnerability of these infrastructures to natural hazards, as well as the major risk of cascading effects, either due to accident propagation onto neighboring infrastructures, or because of interconnectedness between CIs. Some of these events have been responsible for widespread infrastructure damage, devastating economic consequences, and significant fatalities. Major past events have shown that these consequences can reach global proportions, resulting in a shortage of raw materials or intermediate products in the manufacturing industry and causing price hikes. Below, a selection of major damages to geographically distributed, non-nuclear CIs exposed to different natural hazards are shortly described.

The **Great East Japan (Tohoku, 11 March 2011)** massive earthquake of magnitude 9.0 and the gigantic tsunami it triggered (in some cases, the height reached more than 15 m, and in some case inland water more than 4 km with a run-up of about 20 m high) both reached unexpected magnitudes of severity and devastated a huge area. This rare case of natural disaster is the worst case scenario with multiple occurrences of different hazards at the same time. Besides the thousands of human fatalities the total economic cost is estimated 150 to 250 billion US dollars, reaching the 4-6% of the Japanese GNP (excluding the mass destruction caused by the Fukushima disaster) according to the projections of the Institute of International Finance, Inc.

The ground shaking itself caused rather limited damage to the port infrastructures. Most damage was caused by the induced phenomena namely the large ground deformations and liquefaction effects that led to the localized failure of wharf structures. Liquefaction occurred in the loose fills during the main shock, and was repeated in subsequent aftershocks, as evidenced by reports of sand boils in the container yards during a major aftershock on 7 April 2011 (Percher, 2014). The most devastating cascading effect was the huge tsunami that hit the ports in a large part of eastern Japan. Many port infrastructures were seriously affected and serious structural and non-structural damage were reported, in several cases total collapses. A total of 14 major ports were affected (PIANC, 2001).

Small and medium sized port facilities suffered major damage to terminal buildings, quays, vehicles in the ports, breakwaters, seawalls and containers, along the Pacific Ocean from Kashima port in south to Kuji port in north where the tsunami waves reached maximum run-up height. Some of quay-walls laterally moved as a result of ground liquefaction (Fig. 3.5) while some piers were cracked due to ground shaking and lateral movements of quays (Aydan 2011). Medium ports at Hachinohe city in Aomori and Kamaishi in Iwate were

severely damaged by the tsunami waves, as they surmounted the ports' breakwater. In Kamaishi port, the world's largest tsunami protection breakwater failed to protect the city as a big part of the breakwater was completely destroyed. In addition, during the tsunami, many ships broke their moorings and collided with port facilities. Smaller breakwaters were also destroyed in Ofunato Port, a smaller scale port in Iwate. Specifically, failing and deformation of quay walls was observed, caused either by the hydrodynamic forces of the waves, or the impact of debris. The intense scour of the foundation materials was also a main reason for the collapse and overturning of quay walls and their accompanying supporting constructions. Moreover, the seaport constructions proved to be especially vulnerable to receding waters, which caused intense deformation and overturning. Finally, the piers constructed in order to protect against tsunami waves could not cope with the observed tsunami, either because of the inadequate structural design, or because of their collapse, resulting in devastating effects on inland areas. In addition, severe failures because of intense erosion (Fig. 2.2) were observed in levees and coastal river regulation constructions (Lekkas et al., 2011).

a) b)

Fig. 2.1 a) Damage in Sendai port, b) Failed quay at Hitachi port (Aydan 2011)

Fig. 2.2 Destroyed port facilities and general alteration of the shoreline in Mizuhama town (Lekkas et al., 2011)

In general terms, breakwaters (including tsunami barriers) were mainly damaged by the tsunami, (including scouring effects) and quay walls were mainly damaged by the seismic motion and liquefaction. The severe damage to warehouses and factories at ports industry areas caused secondary but important impacts. In addition to the sheer impact of the tsunami on structures, damage due to collision with the debris-laden waters was also observed. The debris that was swept along with the tsunami also caused blocking of the

port's access roads. Thousands of containers at Sendai Port floated from their foundations and were scattered by the action of tsunami (Tomita and Yoem, 2012) and added to the tsunami debris. Also, the permanent deformations of the Takasago wharf resulted in differential horizontal movements between the construction joints of the crane rails, in response to the lateral spreading thereby, as shown in Fig. 2.3 (Percher, 2014). While some damage to the cranes of Sendai Port was observed, in general they performed well.

a)   b)

Fig. 2.3 a) Landside crane rails at the eastern side and b) Rotated wharf closure bulkhead at the east end of the Takasago wharf (Percher, 2014)

Despite the port facilities other lifeline infrastructures such as electricity, water supply, sewage systems, and gas lines, they were also seriously damaged. The water supply was interrupted because many of the water distribution pipes along rivers or canals broke, while they suffered extensive damage, since the concrete slabs were lifted, displaced and broken.

The Christchurch earthquake (New Zealand, 22 February 2011) resulted in widespread liquefaction damage throughout the affected area, leading to significant damage and substantial disruption of lifeline systems, such as underground water and wastewater pipelines. The more flexible gas network behaved much better. This event was unprecedented in terms of repeated strong earthquake shocks with substantial levels of ground motion affecting a major city with modern infrastructure. Underground pipe networks such as the potable water, wastewater and storm water systems were hit particularly hard in the areas severely affected by the large ground movements and deformation resulting from the severe liquefaction and lateral spreading. Loss of grade, joint failures, cracks in pipes and failure of laterals were the most commonly observed types of failures. Buoyancy of concrete vaults at potable water and wastewater pump stations, compounded by liquefaction-induced settlement, caused pipeline breaks at their connections with the vaults. In contrast, the gas system, which was only 10 to 15 years old, showed an excellent level of robustness, remaining undamaged despite the high level of ground shaking and liquefaction-induced ground damage. As reported by O'Rourke et al. (2014), there was virtually no damage in the gas pipeline network. Damage was documented in only one service line, which was tied into a concrete block subjected to ground settlement. There were two minor flange leaks on steel pipe work at one of the gas terminals. There were no gas related fires.

The Darfield Earthquake (New Zealand, 4 September 2010) inflicted extensive damage to lifelines and residential houses due to widespread liquefaction and lateral spreading in areas close to major streams, rivers and wetlands throughout Christchurch and Kaiapoi. Regarding Lyttelton Port of Christchurch, which is the main port for the Canterbury region, port officials were quite satisfied with its performance, but acknowledged that there would be significant repairs and rebuilding. While some Port facilities sustained significant damage, most of them were operational within few hours after the earthquake and no scheduled shipments were missed. No interruption in fuel from Lyttelton Port of Christchurch was also observed. In addition, while there was some lateral (seaward) displacement of the deck for the container terminal, no damage to the cranes was noted and they were still performing as intended after the earthquake. The crane rails are closely enough spaced that both rails fit on the wharf deck. Having both rails on the deck appears to have avoided differential movement of the rails and contributed to the good performance of the Port facilities. Fig. 2.4 shows typical damage from settlement and lateral deformation. The limited wharf movements did open up cracks in the asphalt pavement sections of the wharf deck. The underground 11kV electric power network remained in service following the earthquake, though the single sub-station at the port did sustain some minor damage (Cubrinovski et. al., 2010).

Fig. 2.4 Settlement and lateral deformation at fuel transfer facility (Cubrinovski et. al., 2010).

By far the greatest impact on the community was the performance of water and wastewater systems in the Canterbury region. Many Districts experienced damage to the pipe networks in areas affected by liquefaction, resulting in loss of service and discharge of untreated wastewater into the groundwater and surface water

The Kocaeli Earthquake (Turkey, 17 August 1999), which caused the damage of a large number of waterfront structures, utilities and tanks, indicated that port facilities are particularly susceptible to submarine landslides or ground settlement due to the liquefaction that may occur during an earthquake. The water transmission network suffered heavy damage due to earthquake loading. According to Durukal and Erdik (2008), there was some damage to major welded steel water transmission lines especially where they cross the fault zone or in areas of severe permanent ground movement. Water supply to some plants (e.g. Tupras Refinery, Petkim petrochemical facility) was disrupted due to damage to the water pump station and pipeline at the Sapanca Lake. The failure of several concrete piles supporting structures at the TUPRAS refinery prevented the loading and unloading of all fuel-oil products at the refinery. Pipes installed over a concrete embankment had fallen towards the sea-side as seen in Fig. 2.5 a) due to the tilting of the supporting device as in

Fig. 2.5b) and a 71 cm (28 in.) pipeline supplying water to the refinery was damaged (Suzuki, 2002). The failure of the water supply eventually caused problems in controlling the fires at the Tupras refinery. Ground failure also caused damage to wastewater pipelines in all regions; in Izmit at least 10 km of reinforced concrete pipes had breaks. In contrast, the natural gas transmission system performed well in the vicinity of the earthquake and IZGAS reported no damage to the 380-km long gas pipelines. However, 860 m gas pipelines were damaged due to collapsed buildings. Fortunately, there were no fires associated with gas leaks due to the very limited residential gas use in summer. While the design and construction of natural gas system appears to be rather well resistant to strong levels of earthquake shaking, which has been also observed in the 1999 Kocaeli earthquake, for pipelines crossing active faults or in regions susceptible to permanent ground displacements the failure is more likely (Durukal and Erdik, 2008).

a)   b)
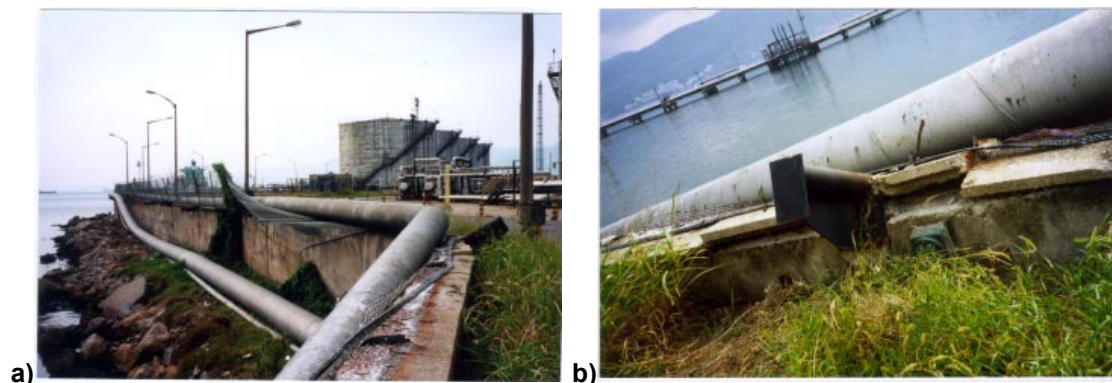
Fig. 2.5 a) Piping fallen from the embankment wall, b) Tilted pipe support on the embankment wall (Suzuki, 2002)

Most of the ports sustained damage that ranged from minor to extensive. Damage included failure of piers, mechanical equipment, piping and the collapse of cranes. Particularly, the port in Derince suffered heavy damage to docks, cranes and warehouses, including cracks and severe subsidence. The concrete caisson type bulkhead, with a length of about 1.5 km, shifted away from the wharf up to 0.7 m horizontally and 1 m vertically, due to liquefaction-induced deformations, settlements and lateral spreading. Two of the three rail mounted main portal cranes were nonfunctional and some old steel warehouses were damaged. A new wharf constructed on piles had no problems. Haydarpasa Port in Istanbul, located about 60 km away from the closest fault break, received minor damage to quay walls. Finally, ground failure was observed near the jetty entrance of the port facility of the Petkim petrochemical plant. This port was not operational afterwards, as many of the battered piles beneath the jetty were badly damaged and some of the pipelines along the pier fell off their supports and were damaged too. Ground cracking and deformations were observed along the shoreline near the pier (Durukal and Erdik, 2008).

The Italian blackout (28 September 2013), is a clear example of the interdependence between large scale interconnected critical systems and their vulnerability to local events that may trigger cascading effects that extend in wide geographical areas. A sequence of critical events took place during the night of 28 of September 2013 that led to one of the biggest – if not the biggest – blackout in Europe that left in dark almost the whole Italy for several hours and in several areas almost a whole day, leading to multi-million euro damages both in destroyed equipment as well as in unrealized production.

The event started with the tripping of a high voltage electrical line that interconnects Switzerland with Italy due to a flashover of a tree. That led to an overload the remaining lines of the Swiss high voltage grid, which can be allowed for a very short period of time. Communication between Italy and Switzerland led to a series of correcting measures (e.g. Italy reduced the demand from Switzerland by 300 MW) but everything took place too slow and that led to a second line tripping. The consequence of that was that the situation was out of control and the Italian grid had to be disconnected from the Swiss grid. Due to the lack power to cover consumption, a series of power generators in Italy tripped as well and after a few seconds a blackout took place.

The blackout took place more or less within 30 minutes from the first line tripping, which can be considered the triggering event. In fact from the moment that the Italian power grid was disconnected from the main European grid the cascading events took place within 2 minutes and 30 seconds. On the contrary the recovery process with lengthy and cumbersome. In fact areas in the north of Italy were back in normal conditions after 3 hours whereas areas in the south returned to normal even after 17 hours from the blackout with obvious economic costs. This shows clearly the importance of measures to speed-up the recovery of critical systems and that in several cases it these must be considered at the same level of priority with prevention. In any case resilience is a matter of absorbing an impact and bouncing back which means that lack of restorative capacity may very well outperform a sound protection plan.

Slovenia had serious problems due to sleet (February 2014). The damage caused by heavy snow and icy rain was the greatest natural disaster in Slovenian forests. Hoar frost and glaze ice across most part of Slovenia caused major disruption in electricity supply. Some regions (approximately 100.000 people) were without electricity for 14 days. Road and railway traffic was disturbed due to heavy snow and sleet, while electricity outages caused disruption in mobile phone services. Due to unfavourable weather elements, about 75 per cent of schools and nurseries were closed. International support via the European Union Civil Protection Mechanism was provided. The combined estimated damage was over 430 million €.

All the aforementioned as well as many other recent events impacting critical spatially distributed infrastructures have highlighted the necessity for the development of guidelines for the performance and consequences assessment of geographically distributed, non-nuclear CIs exposed to multiple natural hazards.

3   Critical Infrastructure

In the framework of STREST three representative case studies of geographically distributed CIs are examined, i.e. CI-B1: Major Hydrocarbon Pipelines in Turkey, CI-B2: Gasunie National Gas Storage and Distribution Network in Holland and CI-B3: Port Infrastructures of Thessaloniki in Greece. In the following, a short description of each case study is provided. The typology of components and their intra-dependencies for each CI are given in STREST D4.4.

3.1   CI-B1: MAJOR HYDROCARBON PIPELINES, TURKEY

There are 2 on-shore and 2 off-shore major hydrocarbon pipeline projects in Turkey. Among these, one project is at construction, one offshore project is at proposal stages and the remaining two are currently under operation.

3.1.1   Onshore pipelines

The Southern Caucasus-Eastern Turkey energy corridors are formed by two critical on-shore pipeline projects carrying crude oil and natural gas from Caucasus to Mediterranean coast and Europe.

3.1.1.1   BTC -Baku Tbilisi Ceyhan (operating):

The 1,758 km long BTC pipeline daily transports about 1% of the world's daily petroleum output, about 1 million barrels (Fig. 3.1). The BTE pipeline has excess capacity today, with 30 billion cubic meters of natural gas a year (https://de.wikipedia.org/wiki/Baku-Tiflis-Ceyhan-Pipeline). The diameter of the pipeline is 42 inches throughout most of Azerbaijan and Turkey. In Georgia the pipeline diameter is 46 inches. The pipeline diameter reduces to 34-inches for the last downhill section to the Ceyhan Marine Terminal in Turkey. The BTC pipeline facilities include: 8 pump stations (2 in Azerbaijan, 2 in Georgia, 4 in Turkey), 2 intermediate pigging stations, 1 pressure reduction station and 101 small block valves.

Fig. 3.1 BTC pipeline to south coast

Fig. 3.2 TANAP pipeline to Europe

3.1.1.2 *TANAP- Trans Anatolian Pipeline (Under construction)*

Trans Anatolian Natural Gas Pipeline Project (TANAP) will connect with the expanded South Caucasus Pipeline (SCP) and be linked to the Trans Adriatic Natural Gas Pipeline (TAP), to supply gas to Europe via Greece, Albania, and Italy by early 2020. The three pipelines together will form the Southern Gas Corridor. It involves the construction of a 1,850km-long pipeline to supply gas from Azerbaijan to Turkey and Europe (Fig. 3.2).

The pipeline construction was started in March 2015. Southern Gas Corridor Closed Joint Stock Company (SGC - 58%), BOTAS (30%) and BP (12%) are the partners in the project development. The overall investment on the project is estimated to reach $11.7bn. It will be one of the world's longest gas pipelines upon completion. There will be 2 outlet connections in Turkish to be connected to the gas transmission system in Turkey. The submarine pipeline length for the Marmara Sea crossing will be 19 km. The project will consist of seven compressor stations, four metering stations, 11 pigging stations, 49 block valve stations and two outlet points to support the local gas supply system in Turkey.

3.1.2 Off shore pipelines

The Northern energy corridor is formed by two critical pipeline projects carrying natural gas from Russia to Turkey, shown in Fig. 3.3.

3.1.2.1 *Blue Stream (Operating)*

The Blue Stream is a submarine pipeline in the Black Sea having a capacity of 16 billion cubic meters (bcma) of natural gas per annum. Total length of the pipeline is 1,213 kilometers (754 mi). It consists of a 380 km section on the bottom of the Black Sea connecting Dzhugba to Samsun on the Turkish coast (submarine section), and a further 483 km link from Samsun to Ankara (Turkish onshore section).

(http://www.gazprom.com/about/production/projects/pipelines/blue-stream/)
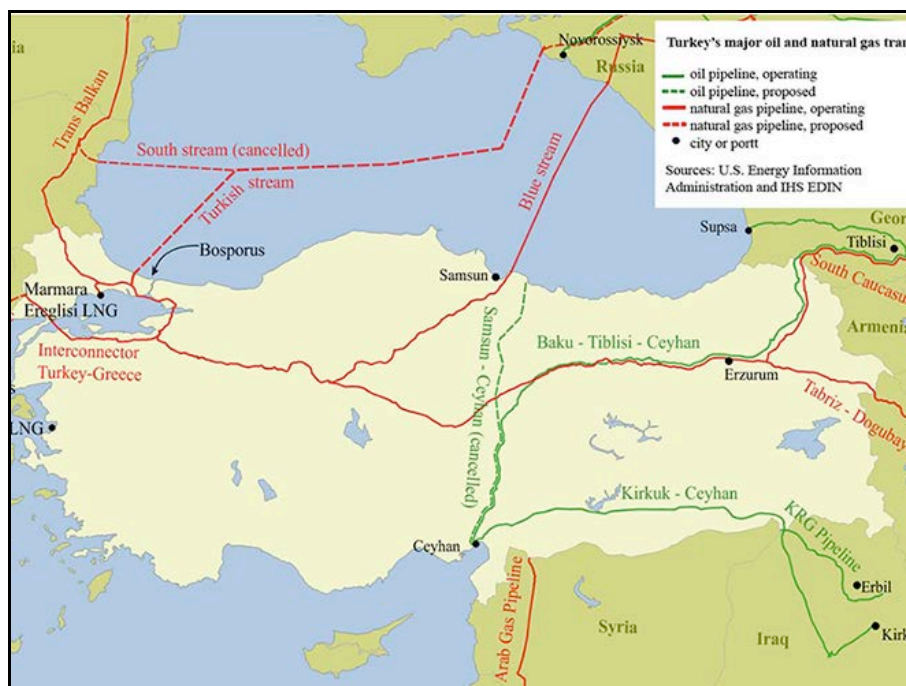
Fig. 3.3 Off shore pipeline projects in Turkey (Blue stream and Turkish Stream)

The pipeline uses pipes with different diameters: mainland section 1,400 millimeters (55 in), mountainous section 1,200 millimeters (47 in) and submarine section 610 millimeters (24 in). The gas pressure in submarine section is 25 MPa (250 atm). It is considered yet one of the deepest pipelines in the world. It is laid in depths as low as 2.2 kilometers (1.4 mi) which

exceeds the average depths of well-known subsea pipelines. https://en.wikipedia.org/wiki/Blue_Stream - cite_note-8

3.1.2.2 *Turkish Stream/South Stream (Proposed)*

The Turkish Stream should replace the cancelled South Stream project. The pipeline would start at the Russkaya compressor station near Anapa. The tentative landing point in Turkey is Kıyıköy, a village in the district of Vize in Kırklareli Province at northwestern Turkey. The offshore part of the pipeline will cross the Black Sea bed. Maximal depth along the route will reach 2,200 m. The length of the offshore part will be about 910 km long. The length of Turkish onshore section will total 180 km. The capacity of four strings totals up to 63 bcma, including 47 bcma to be supplied to the Turkish-Greek border.

3.2 CI-B2: GASUNIE NATIONAL GAS STORAGE AND DISTRIBUTION NETWORK, HOLLAND

The Groningen field is a large natural gas field located in the northern Netherlands, contributing to approximately half of the natural gas production in the Netherlands. On- and off-shore natural gas production and distribution is the key component of the national energy supply in the Netherlands. The gas distribution relies on a major gas pipeline infrastructure, with a total length of over 12'000km of installed pipes in. The production from the Groningen field and other natural gas fields mostly located in the north east part of the country supply the Dutch economy and major export across Europe, via cross-border long distance gas pipelines (European Natural Gas Round-About). Located in an area of very low tectonic seismicity, gas extraction in the region has led to an increase in seismicity since the early 1990s. Additionally, Holland has a long history of catastrophic inundations and provides a text-book case of defense, preparation and construction of water infrastructures to protect against future repetition of such events.

For the use case a sub-network is selected located in the induced earthquake prone area, directly above the main gas field, see Fig. 3.4. The sub-network selected covers an area of approximately 3360 km^2. It contains 4 MPa (40 bar) and 8 MPa (80 bar) main gas transmission pipes, with a total length in the order of 1000 km. Different pipe diameters are present within this sub-network ranging from 108 millimeters (4 in) to 1220 mm (48 in). Apart from 426 valve stations, it contains compressor stations, measure and regulations stations, reducing stations and a mixing station (13 in total). With respect to the end nodes of the sub-network: 16 feeding stations and 95 receiving stations are accounted for, the latter being sub-divided into 38 industrial, 56 municipal and 1 export.
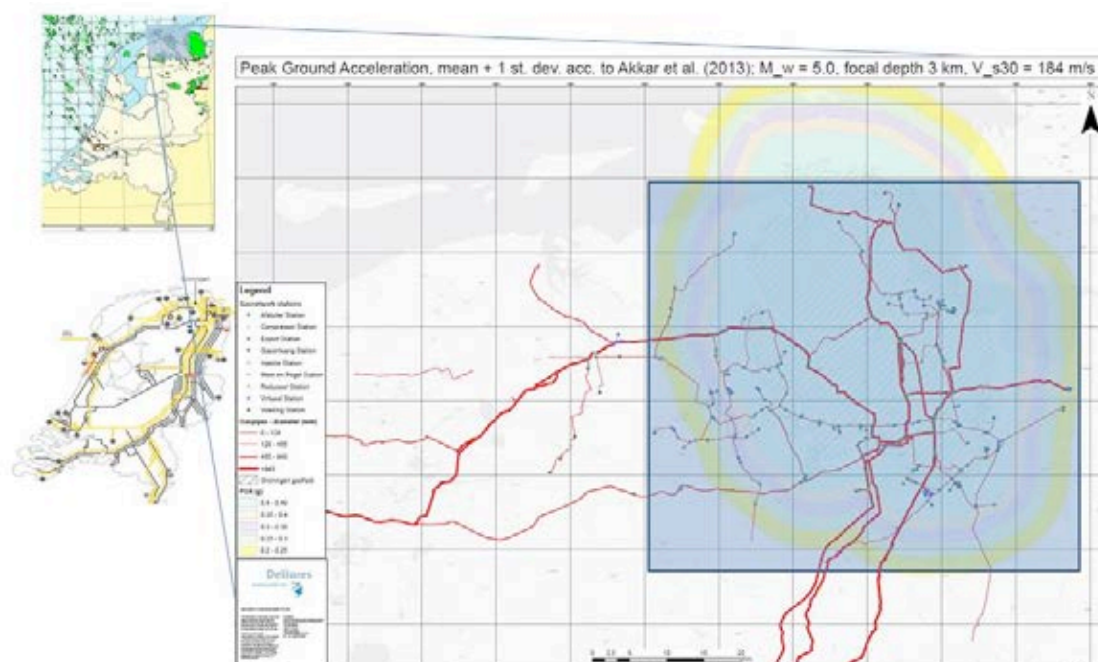
Fig. 3.4 Selected sub system of gas distribution network (right) located above main natural gas field (top left).

3.3 CI-B3: PORT INFRASTRUCTURES OF THESSALONIKI, GREECE

3.3.1 General description

The port of Thessaloniki constitutes the most important port in Northern Greece and one of the most important ports in Southeast Europe. It is the largest transit-trade port in the country and it services the needs of approximately 15 million inhabitants of its international mainland. It is located on the inner part of the Bay of Thermaikos, on the northern section of the Eastern Mediterranean Sea, to the west of the center of the city of Thessaloniki. Approach of the ships is accomplished through a natural channel of substantial depth, not needing thus any further deepening. It occupies a total space of 1.5 million square meters and it spreads across a length of 3.5 km (Fig. 3.5).

The installations include 6 piers spreading on a 6,200 meter-long quay and a sea depth down to 12 meters, with open and indoors storage areas spreading on a total of 600,000 square meters, suitable for servicing all types of cargo as well as passenger traffic. The port also has installations suitable for liquid fuel storage and it is located in proximity to the international, natural-gas pipeline. It annually trades approximately 14,500,000 tons of cargo, and 350,000 TEU's containers (as per year 2014). The loading and unloading of cargoes as well as the embarkation/disembarkation of passengers on the ships are taking place unhindered, throughout the year.

The Free Zone (control type I: fencing, customs' supervision and cargo inspection on the points of entrance – exit, inspection of persons and vehicles) is also part of the port of

Thessaloniki and it is operating since 1995 in accordance with the Community Customs Code. It is linked to a dense, traffic network that is directly linked to the national and international road network. All the port quays are linked to the national and international railroad network.

It has been characterized as a Port of National Interest in the Country's Coast-guard System and one of the five Greek ports, which belongs to the Core Network of Trans-European Transport Networks. It is located at a distance of 1 km from the Passenger Railway Station and 16 km from the city's International Airport.

Various data are available for the construction, typological and functional characteristics of port facilities, including cargo and handling equipment, waterfront structures, electric power (transmission and distribution lines, substations), potable and waste water (pipelines), telecommunication (lines and stations), railway (tracks) and roadway (roads and bridge) systems as well as buildings and critical facilities.

The various components and systems existing inside the port facilities are illustrated in Figures 3.6 and 3.7.

Fig. 3.5 Thessaloniki's port.

——	Port Boundaries	——	Quay Walls
△	Entrances	——	Telecom. Lines
——	Buildings Lines	●	Tel. Cabins – Tel. Center
■	Buildings	●	Tel. Manholes
●	Cranes	——	Railway Lines
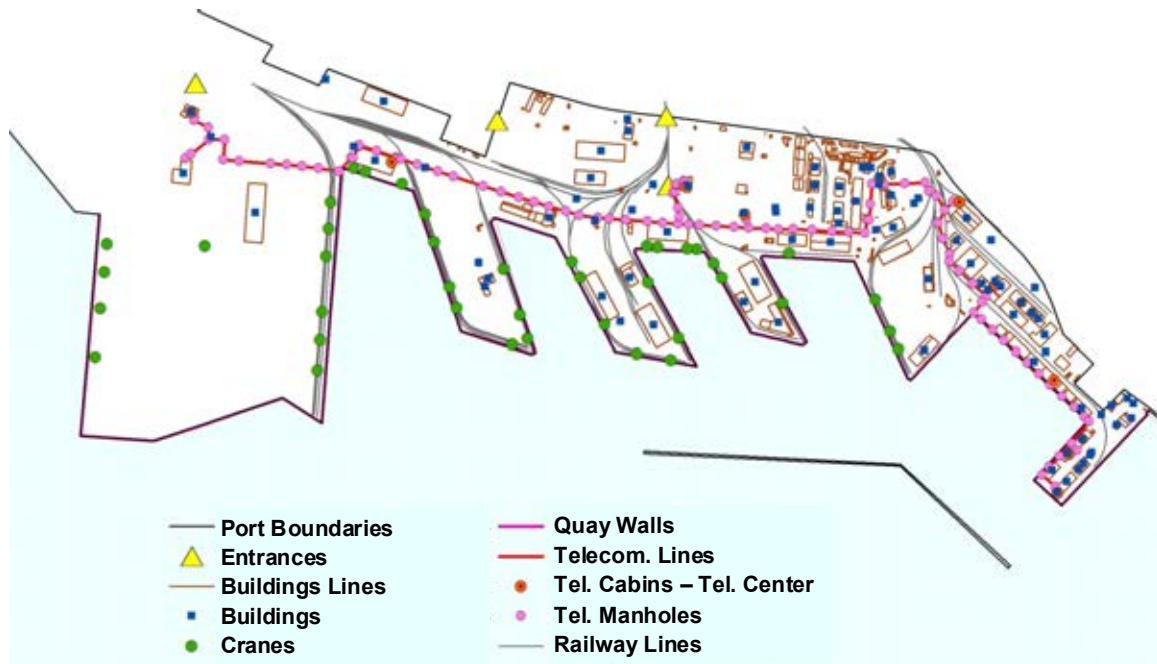
Fig. 3.6 Building facilities, waterfront structures, cargo handling equipment, telecommunication system and railway network of Thessaloniki's port.

——	Water Pipes	——	Electric Power Lines
◉	Water Manholes	●	Electric Power Substation
●	Tanks	▲	Power Gen.
■	Water Netw. Conn.	◉	Fuel Tanks
●	Fire Faucets	■	Fuel Pump. St.
——	Waste-water Pipes	——	Port Boundaries
◙	Waste-water Pump. St.		
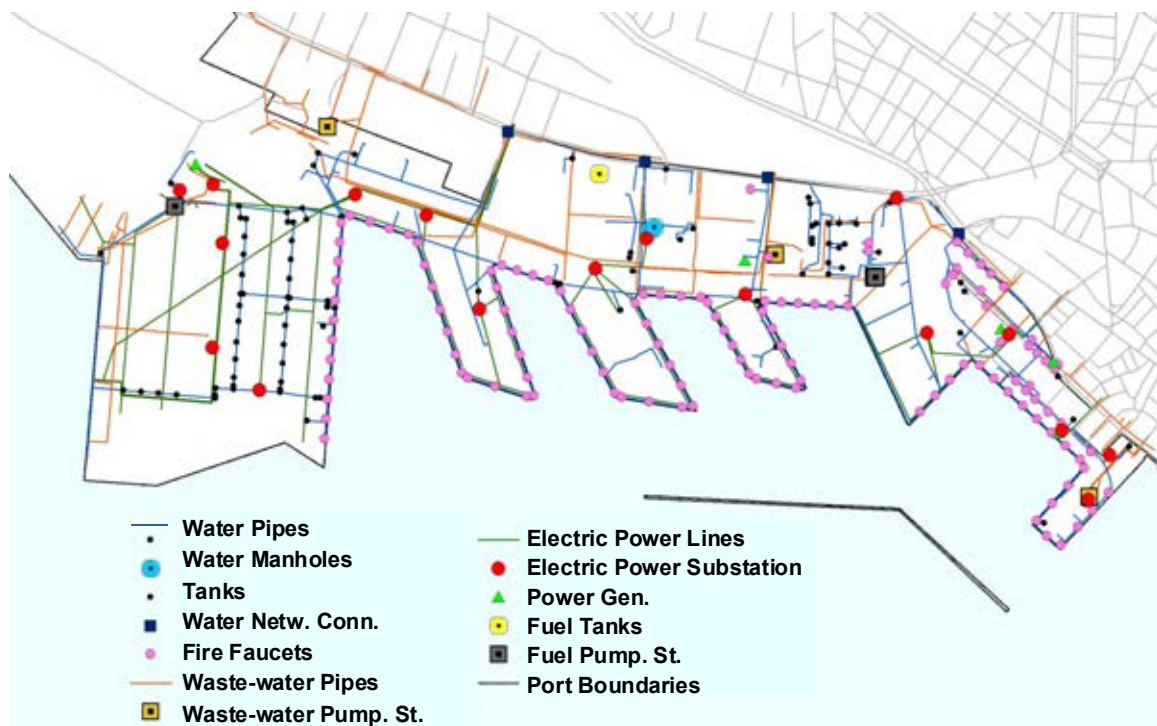
Fig. 3.7 Water supply, waste-water, fire-fighting, electric power and fuel supply systems of Thessaloniki's port.

3.3.2 System and components interactions

The main characteristic of port systems is the multiple interactions existing within their elements and with the external supplying or/and supplied systems and infrastructures. The

ports' functionality is dependent on the functioning of each system/component, taking also into consideration the interactions between them.

The **inter-dependencies** between port facilities and the other systems are described in Table 3.1. They are distinguished in physical (direct) and informational, geographic, restoration, substitute (indirect) inter-dependencies. Furthermore, they are classified as crucial, important and secondary.

The **intra-dependencies** between port facilities and infrastructures are described in detail in the Dependencies Fact Sheet given in STREST D4.4. Some characteristics examples include the supply of electric power to cranes, traffic control infrastructures, building facilities, utility systems' and transportation infrastructures' components, possible road closures in case of building collapses or the transfer of restoration material through roadway/railway system.

Table 3.1 Inter-dependencies between harbour facilities and other networks

Impacts →		BDG	EPN	WSS	WWN	GAS	OIL	RDN	HBR	HCS	FFS
Buildings	**BDG**								3-Geo		
Electric power network	**EPN**								1-Phy		
Potable water network	**WSS**								1-Phy, 3-Res		
Waste-water network	**WWN**								1-Phy, 3-Res		
Gas network	**GAS**								1-Phy/ Geo, 3-Res		
Oil network	**OIL**								3-Phy		
Road network	**RDN**								1-Phy, 3-Res		
Port	**HBR**	3-Res	3-Res	3-Res	3-Res	3-Res	3-Res	3-Phy, 3-Res		3-Res	3-Phy, 3-Res
Health-care system	**HCS**										
Fire-fighting system	**FFS**										
Shelter model	**SHM**										
Health impact model	**HIM**										

Priority definitions:

1. Crucial dependencies (that MUST be both well described and implemented).

2. Important dependencies [that NEED to be well described and that SHOULD be implemented (if possible, using simplifications if necessary)].

3. Optional/secondary dependencies (that should be mentioned, but whose implementation is not necessary).

Types of interactions:

Direct:

Phy: Physical, functional interdependency - functional damage propagation.

Indirect:

Inf: Cyber, informational interdependency

Geo: Collocation, geographic, space interdependency - physical damage propagation.

Res: Restoration - recovery interdependency.

Sub: Substitute interdependency.

Seq: Sequential interdependency - scaling effects.

Log: Logical interdependency, financial markets - policy/procedural interdependency.

Gen: General interaction.

Soc: Societal interdependency.

4 Hazard assessment methods in a multi-risk environment

Critical Infrastructures (CIs) are systems composed by many components, which are physically and/or functionally dependent to each other. In addition, the functionality of such components may be dependent on external supplies (from other systems, like for example the supply of electric power). Thus, a complete risk assessment for CIs requires first analysing potential damages and consequent non-functionality of each single component, and then modelling the impact on the system of such potential non-functionalities. Of course, more than one component may be damaged during the same event, increasing the potentiality of systems' failures. If CIs' components are geographically distributed, during the same event, different hazard intensities may be experienced at the different locations where components are located. In addition, different components may be sensible to different intensity measures related to the same hazard (e.g. for ground shaking, to PGA and PGV), or to secondary induced hazards (e.g. geotechnical hazards). Given that different components have different roles within the system, it is critical to consider realistic distributions of damages induced by each potential source event. Such intensities cannot be assumed independent, since they are caused by the same source event (e.g. one earthquake) that may induce important spatial correlations. In this case, it is clear that it is necessary to model the potential spatial correlations of the hazard intensities (SYNER-G, 2010-2014).

In general, in order to model spatial correlations in hazard intensities, it is required i) to model separately the propagation of the hazard intensity due to one single hazardous event (e.g. an earthquake), ii) to evaluate the intensity of potentially secondary intensity measures and induced hazards, iii) to evaluate the potential damages and non-functionalities for all the components caused by the spatially correlated hazard intensities of such event, iv) to evaluate the impact on the CI performance given the obtained configuration of damages, v) to combine statistically the CI performance results for all the possible events that may cause damages in the target area (e.g. Cavalieri et al, 2012; Argyroudis et al., 2015), in order to compute a risk/performance curve for the CI (reporting the probability of exceedance of different performance loss within a given exposure time).

Adopting this approach, hazard results are not considered in the form of hazard curves (reporting the probability of exceedance of different levels of intensity in each location), since each potential source event is treated separately. Even if this approach can be adopted to evaluate the hazard in all cases, it is generally very expensive from a computational point of view. Therefore, when this is possible, several simplifications are adopted, in order to significantly decrease the computational effort. The possibility of adopting such simplifications completely depend on the characteristics of the hazard intensity propagation (e.g. ground shaking) from a source event (e.g. an earthquake) to the component location.

For several natural hazards, it is typically required to model all the single events. For example, this happens when the propagation of the hazard intensities around the source event is highly directional. Examples of this are tsunami and volcanic hazards (e.g. for tsunami hazard: Geist and Parsons, 2006; Sørensen et al., 2012; Lorito et al., 2015, Selva et al., submitted; for volcanic hazard: Costa et al., 2009; Selva et al. 2010; Neri et al., 2015). In these cases, independently on the geographical extension of the target CI, the propagation

of hazard intensities for all the potential source events are explicitly jointly modelled for all the target area. For each simulated event, the potential spatial correlations on the hazards are automatically accounted for. If necessary, hazard curves are evaluated only at the very end of the process, by statistically combining all the single intensity fields.

On the opposite, for other natural hazards, it is possible to reduce the computational effort of the hazard assessment adopting specific simplification strategies. One example of this is seismic hazard. Since the propagation of seismic waves in the medium-far field is not strongly directional, empirical models like Ground Motion Prediction Equations (GMPEs) can be adopted. Such laws statistically correlate the hazard intensity with the distance from the source (and its energy). This allows reducing by far the computational effort for Probabilistic Seismic Hazard Analysis (PSHA), since hazard curves may be obtained directly through an integral formulation. However, adopting GMPEs, spatial correlations on seismic intensities are completely lost. Therefore, if their evaluation is required by the application, such correlations must be re-introduced *ex-post*, for example sampling spatially correlated residuals with respect to the GMPE's mean value (e.g. Jayaram and Baker, 2009). Since this process is subject to large uncertainties (see D3.3, Iervolino et al., 2015), it must be evaluated carefully when it is possible to avoid this step. For example, sensitivity tests can be performed to quantify the importance of spatial correlations of hazard intensities for a given geographically extended CI (see D3.1, Selva et al., 2015).

In the following, a short description of a general framework for hazard analysis of spatially distributed systems for the seismic hazard case, i.e. the "Shakefield" method (Weatherill et al., 2014) developed in the framework of SYNER-G project (2010-2014) and the seismic hazard scenarios for geographically distributed systems developed in the framework of STREST, are provided. For the later the multi-scale random fields (MSRFs) hierarchically characterizing the randomness of a physical process at different resolution levels has been used together with MC simulations to generate spatially correlated intra-event residuals by following Chen et al. (2012) approach for behavior of heterogeneous soil medium under different levels of uncertainty.

4.1   THE "SHAKEFIELD" APPROACH

The Shakefield process (Weatherill et al., 2014) is intended to provide the seismic input for the fragility models of the vulnerable elements of each infrastructure in a complex interconnected system of infrastructures. Each Shakefield represents a simulated strong ground motion field for a given rupture scenario. Shakefields can be adopted for single earthquake scenarios or can be applied within a probabilistic seismic hazard analysis. They allow the spatial correlation of the ground motion fields for different measures of the ground motion intensity to be incorporated into the simulation procedure. This is extended further to consider spatial cross-correlation between different measures of ground motion intensity.

The "Shakefield" approach may be summarized in the following steps (Fig. 4.1):

1. First, a source event with a given magnitude and source geometry is generated. The geometry may take the form of a point or a finite rupture surface, the latter being preferred for consistency with the physical properties of the earthquake source. The source event may be a single scenario event (e.g. a historical earthquake or a hypothetical adverse case), or may be a sample from a probability distribution representing the total magnitude frequency distribution of the seismogenic source and the set of potential seismogenic sources under

consideration. In the framework of STREST, the determination of low-probability-high-consequence earthquake scenarios for critical geographically distributed infrastructures, possibly corresponding to full rupture of a fault segment or rupture cascade across multiple segments, may allow the evaluation of the performance and loss of the systems under extreme conditions.
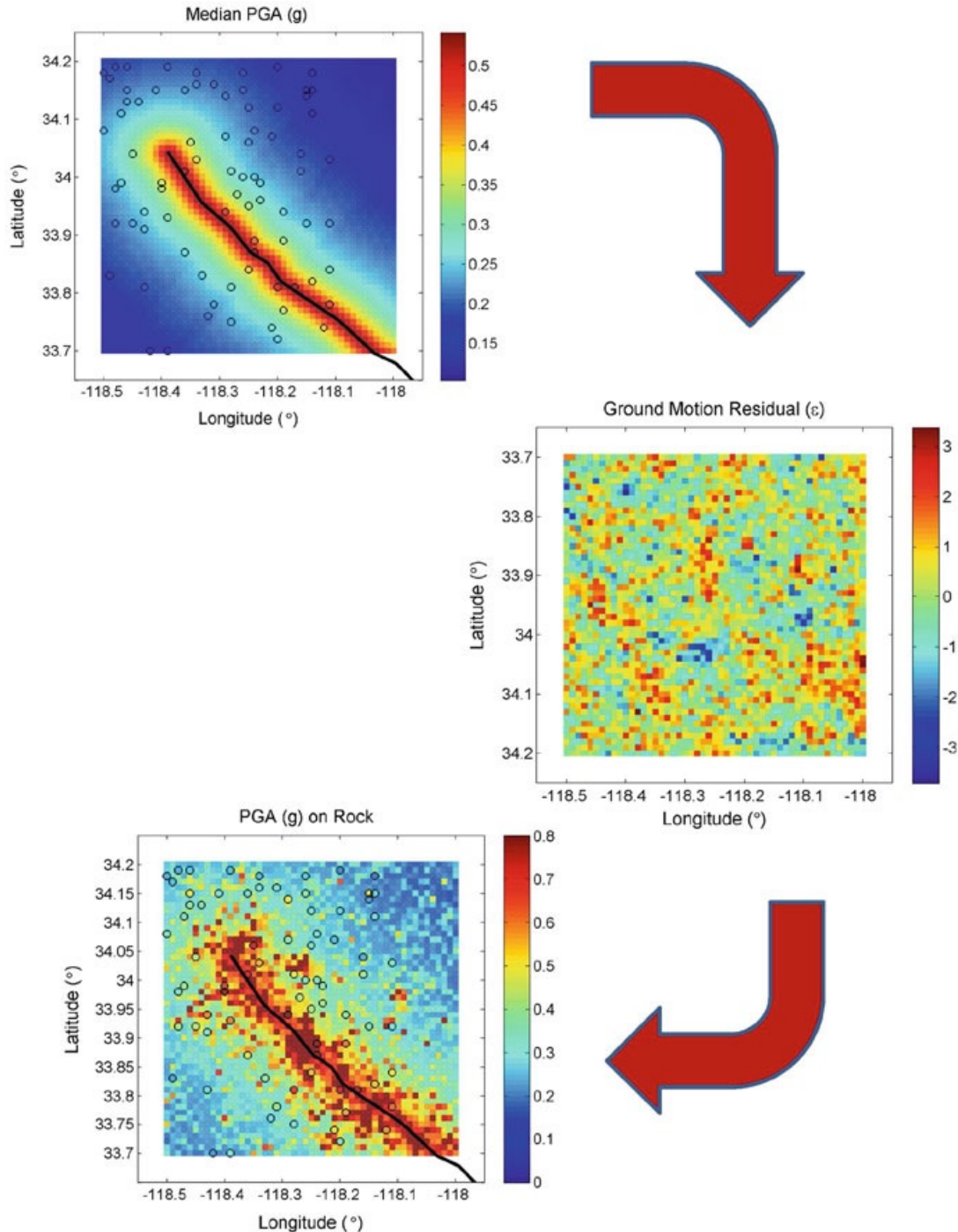
Fig. 4.1 Overview of the Shakefield process for strong motion on rock: attenuation of median ground motion (top), generation of field of spatially correlated ground motion residuals (middle) and calculation of ground motion on rock (bottom). Fault source indicated by black line, target sites indicated by black circles (Weatherill et al., 2014)

2. For seismic sources defined according to simple rupture geometry, the most common method of generating a "Shakefield" is via the use of empirical ground motion prediction equations (GMPEs). With the use of the appropriate GMPE, the median ground motion field across spatial grid of locations considered in the system is attenuated from the source. Depending on the context and the number of locations under consideration, the nodes of the field may be the locations of the elements themselves, or a regularly spaced grid of points from which the ground motions at the element locations can be interpolated.

3. A realisation of a standard Gaussian field representing the spatial correlation structure of a required intensity measure is generated. For each site these variants are multiplied by the uncertainty terms of the GMPE and added to the median value on rock, thus sampling the ground motion uncertainty.

4. For each site, the ground motion values for the secondary intensity measures, conditional upon the simulated ground motion intensity measure of the primary IM are generated.

5. The ground motions are scaled to give the ground motion field on soil using an amplification factor appropriate to the soil conditions and earthquake intensity at each site.

6. If required (e.g. for infrastructures with buried linear elements, which may traverse different geological formations within the interconnected system), estimates of permanent ground displacement due to liquefaction, slope displacement and co-seismic fault rupture conditional upon the intensity of ground motion at the site may be provided.

An example shake map following the Shakefield approach for a particular simulation is shown in Fig. 4.2 (PGA on rock) for the city of Thessaloniki (Argyroudis et al. 2014). The higher residuals are observed in the area with darker colours. This sample event is representative for the specific epicenter, magnitude as well as the specific realization of the spatially correlated ground motion field.
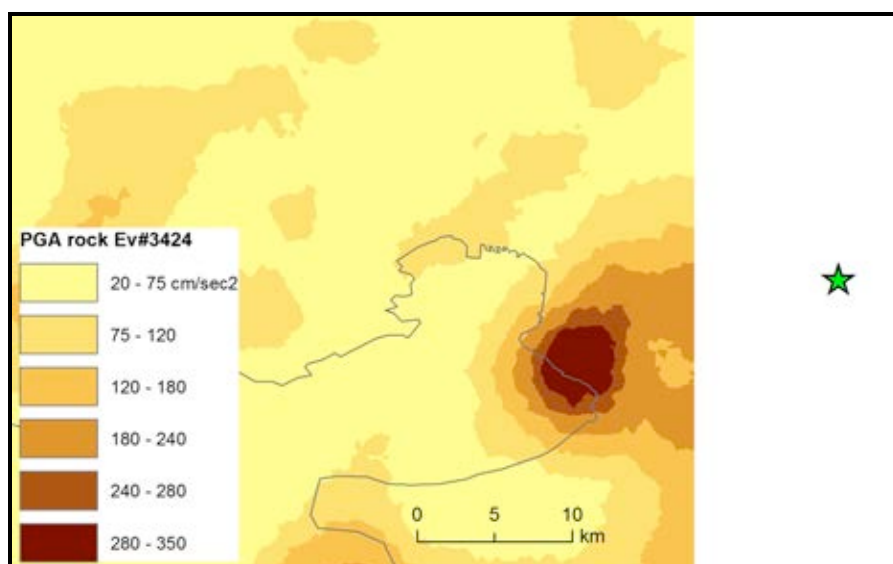
Fig. 4.2 Example of shake map in terms of PGA on rock for a sample event (M=6.5, R=15 km) near the city of Thessaloniki.

A comparison between the "shakefield" approach and 3D physics-based numerical simulations of seismic wave propagation is presented in STREST deliverable D3.4. The study has pointed out that improved results can be achieved in terms of spatial

correlation of ground motion using physics-based 3D numerical simulations of ground motion owing to a more accurate and detailed characterization of the wavefield from the seismic source up to the site of interest (fault rupture process, focal mechanism, directivity effects, topographic effects, earth propagation path and 3D site effects, if included), which are not taken into account by standard tools based on GMPEs. In particular, it was found that the 3D model can predict larger median PGV values than shakefield approach, by a factor up to 1.6 owing to a more accurate characterization of the wavefield in the near field region (focal mechanism and up-dip directivity effects) while the 3D model results can be significantly lower, up to a factor of one fourth, in the hangingwall of the fault. However, 3D physics-based numerical simulations have limitations due to the computational cost, the limited frequency range (up to 2-3Hz), and the geological and geotechnical data required to build the 3D physical model.

4.2 SEISMIC HAZARD SCENARIOS FOR GEOGRAPHICALLY DISTRIBUTED SYSTEMS

The consideration of site-to-site variation (spatial correlation) in dynamic Ground Motion Intensity Measures, GMIMs (e.g. PGA, Sa) is important for realistic probabilistic seismic hazard and risk assessment of geographically distributed building portfolios and lifeline systems. The interdependency between the GMIMs (cross-correlation) is also important for such structural systems because the vulnerability of some of their components are sensitive to the conditional occurrence of multiple GMIMs. Apart from these two phenomena, the proper amplitude estimations of static (permanent fault displacement) and dynamic GMIMs is crucial for geographically distributed buildings or lifelines located in the close proximity to fault segments.

Studies to model spatial correlation (e.g. Boore et al., 2003; Wang and Takada, 2005; Goda and Hong, 2008; Jayaram and Baker, 2009; Esposito and Iervolino 2011l; Goda and Atkinson; 2009), cross-correlation (e.g. Baker and Jayaram, 2008; Bradley, 2011, 2012a, 2012b; Cimellaro, 2013; Akkar et al. 2014a, 2014b; Cheng et al. 2015), combined effects of spatial- and cross-correlation (e.g. Goda and Hong 2008; Loth and Baker, 2013) as well as near-fault effects on dynamic GMIMs (Somerville, 2003; Tothong et al. 2007; Shahi and Baker, 2011; Bayless and Somerville, 2013; Chiou and Spudich, 2013; Rowshandel, 2013) and fault displacements (e.g. Stepp et al., 2001; Youngs et al., 2003; Petersen et al., 2011) are abundant in the literature. There are also several papers showing their implementations by using conventional PSHA Cornell, 1968 (e.g. Shahi and Baker, 2011; Stepp et al., 2001; Youngs et al., 2003; Petersen et al., 2011; Iervolino et al., 2010; Chioccarelli et al., 2012). Alternative to conventional PSHA, Monte Carlo (MC) simulation techniques have become appealing in probabilistic hazard calculations as they provide some flexibility, transparency and robustness (Crowley and Bommer, 2006) while considering the above stated complex features in earthquake phenomenon (e.g. Musson, 1999, 2000; Assatourians and Atkinson, 2013). Monte Carlo simulations are also used in probabilistic risk assessment of geographically distributed systems (e.g. Crowley and Bommer, 2006; Sokolov and Wenzel, 2011a, 2001b; Atkinson and Goda, 2013; Bal et al. 2010). Crowley and Bommer (2006) demonstrated that the use of MC simulations leads to lesser conservatism in probabilistic risk assessment at multiple sites as the former could easily adopt the spatial correlation in

GMIMs. Bal et al. (2010) investigated the influence of geographical resolution (grid sizes) of the ground motion field and exposure data on the assessment of earthquake losses in urban areas. Sokolov and Wenzel (2011a, 2011b) used MC simulations to emphasize the significance of proper modeling in between-earthquake and site-to-site (spatial) correlations for seismic loss estimation of distributed portfolios. Based on MC simulations, Jayaram and Baker (2010) proposed an efficient simulation-based framework for developing a small but stochastically representative catalog of earthquake ground-motion intensity maps that can be used for lifeline risk assessment. Wang et al. (2010) used MC simulations to assess the seismic risk of the water supply systems by identifying the most critical links that would affect their seismic performance. In a similar manner, Esposito et al. (2015) assessed the performance of gas distribution network of the L'Aquila city both for dynamic GMIMs and fault displacements by applying MC simulations. Recently, Weatherill et al. (2015) explored the effect of spatially cross-correlated random fields of different GMIMs on seismic risk analysis for the Tuscany region in Italy.

This chapter implements MC simulation technique together with the multi-scale random fields (MSRFs) approach (Chen et al. 2012) to account for spatial correlation in estimating the joint hazard of dynamic GMIMs for PSHA of geographically distributed structural systems. The proposed approach differs from the other MC-based seismic hazard procedures that generate normally distributed and spatially correlated GMIMs via Cholesky decomposition (e.g. Weatherill et al. 2015). As indicated above we propagate its application into PSHA as an alternative to Cholesky decomposition technique. At the expense of increased computational burden (which is the case in all MC-based methods), MSRFs technique can account for spatial correlation at different precision levels in order to fine-tune the accuracy of hazard curves at the mesh grids critical to design and risk assessment of geographically distributed structures. Using particular properties of MSRFs technique and flexibility provided by MC simulations, we further implemented the near-fault directivity effects on the hazard computations. The MC-based simulations are also used in the permanent fault displacement hazard by adopting the probabilistic model provided in Petersen et al. (2011). To our knowledge, this is one of the few studies (e.g. Weatherill et al., 2014) that presents MC-based hazard calculation for probabilistic fault displacement hazard assessment. The chapter first describes the PSHA of dynamic GMIMs through the application of MC-based MSRFs approach. This part is followed by the discussions about the implementation of MC simulations in probabilistic fault displacement hazard. We demonstrate several examples to discuss the strengths of the proposed procedures for the hazard assessment of geographically distributed building portfolios and lifeline systems.

4.2.1 Monte-Carlo based Multi-Scale random fields for dynamic GMIMs

The multi-scale random fields (MSRFs) hierarchically characterize the randomness of a physical process at different resolution levels. We use this concept together with MC simulations to generate spatially correlated intra-event residuals by following Chen et al. (2012) who studied the mechanical behavior of heterogeneous soil medium under different levels of uncertainty. The spatially correlated intra-event residuals leads to the sampling of spatially correlated GMIMs over the region of interest. MSRFs method is based on regular grids of cells. The residuals as well as the GMIMs are sampled at the centroids of the cells. Therefore, the separation distances used in the spatial correlations are centroidal distances. The sampled GMIMs can account for near-fault directivity effects depending on the relative

locations of the sites with respect to the fault. Our procedure also considers cross-correlation of sampled primary and secondary GMIMs to assess conditional hazard.

We implement 2 scale levels (coarse-scale and fine-scale) while generating spatially correlated intra-event residuals. Fig. 4.3 illustrates the coarse-scale and fine-scale random fields (coarse-scale and fine-scale cells). The center-to-center distances between the cells are used in spatial correlation as the sampled residuals are located at the mid points of the grids. The sampled intra-event residual in a coarse-scale cell is the average of sampled intra-event residuals of fine-scale cells within the corresponding coarse-scale cell. This relationship is given in Equation 4.1 where Z stands for the sampled intra-event residual. The indices "1" and "2" designate coarse-scale and fine-scale cells, respectively. n is the number of fine-scale cells within the coarse-scale cell and b represents the index number of the coarse-scale cell.

$$Z_{1,b} = \frac{1}{n} \sum_{i=1}^{n} Z_{2,bi} \qquad (4.1)$$

The intra-event residuals are sampled via MC simulation and we make use of the intra-event standard deviation of the GMPE used in the entire process. The intra-event standard deviation accounts for the variability in sampled intra-event residuals. Spatial correlation is considered while sampling the intra-event residuals to mimic the interdependency of generated GMIMs at closely spaced sites (cells) because the waveform radiation patterns are coherent at close sites under a given earthquake. The intra-event residual sampling starts from coarse-scale fields and extends into fine-scale as well as coarse-to-fine scale cells through sequential conditional simulation. The sequential conditional simulation transfers the knowledge of previously sampled intra-event residuals to the next sampled intra-event residual.
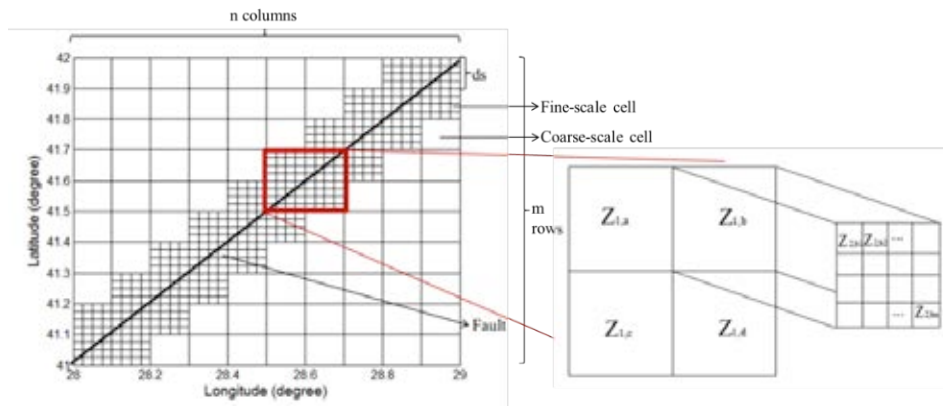
Fig. 4.3 Graphical representation of coarse-scale and fine scale cells. The solid diagonal line is the fault. The area enclosing the fault segment is divided into *m×n* coarse-scale cells. Some of the coarse-scale cells are further refined into *ds×ds* fine scale cells. The right panel is the close-up view of 4 coarse scale cells located in the vicinity of the fault and, for illustration purposes, we show one of these coarse scale cells refined into 4×4 fine-scale cells

Although MC-based intra-event residual sampling starts at coarse-scale level, the sampling distributions of coarse-scale and fine-scale cells are directly related to each other. The intra-event residual distribution at fine-scale level is normal with zero mean and standard deviation σ_{Z2}. σ_{Z2} is the intra-event standard deviation of the pertaining GMPE used in the calculations. Equation 4.1 leads to the below expressions to compute the mean (μ_{Z1}) and standard deviation (σ_{Z1}) of normally distributed intra-event residuals for coarse-scale cells.

$$\mu_{Z1} = E(Z_1) = E(\frac{1}{n}\sum\nolimits_{i=1}^{n} Z_{2i}) = \frac{1}{n}E(\sum\nolimits_{i=1}^{n} Z_{2i}) = \frac{1}{n}\sum\nolimits_{i=1}^{n} E[Z_{2i}] = 0 \tag{4.2}$$

$$\sigma_{Z1}^2 = E[Z_1^2] - E[Z_1]^2 = E[Z_1^2] - 0 = \frac{1}{n^2}\sum\nolimits_{i=1}^{n}\sum\nolimits_{j=1}^{n}\rho_{Z2i,Z2j}\cdot\sigma_{Z2i}\cdot\sigma_{Z2j} \tag{4.3}$$

In Equation 4.3, $\rho_{Z2i,Z2j}$ is the spatial correlation coefficient between two fine-scale cells that is controlled by the separation distance between them. As discussed in the introduction, there are handful spatial correlation models in the literature for calculating $\rho_{Z2i,Z2j}$ (e.g.Goda and Hong, 2008). σ_{Z2i} and σ_{Z2j} are the intra-event residual standard deviations of the *ith* and *jth* fine-scale cells, respectively. Z is the sampled intra-event residual, n is the number of fine-scale cells in the corresponding coarse-scale cell and indices *1* and *2* indicate coarse-scale and fine-scale cells, respectively. E denotes the expected value operator. The spatial correlation coefficient between two fine-scale cells, $\rho_{Z2i,Z2j}$, is used to derive spatial correlation coefficients for coarse-to-coarse scale and coarse-to-fine scale cells. These expressions are given in Equations 4.4 and 4.5 and are used to sample intra-event residuals by sequential conditional simulation.

$$
\begin{aligned}
\rho_{Z1a,Z1b} &= \frac{\text{cov}[Z_{1a},Z_{1b}]}{\sigma_{Z1a}\sigma_{Z1b}} \\
&= \frac{\text{cov}[1/n\sum_{i=1}^{n}Z_{2ai},1/n\sum_{k=1}^{n}Z_{2bk}]}{\sqrt{1/n^2\sum_{i=1}^{n}\sum_{j=1}^{n}\rho_{Z2ai,Z2aj}\cdot\sigma_{Z2ai}\cdot\sigma_{Z2aj}}\sqrt{1/n^2\sum_{i=1}^{n}\sum_{j=1}^{n}\rho_{Z2bi,Z2bj}\cdot\sigma_{Z2bi}\cdot\sigma_{Z2bj}}} \\
&= \frac{\sum_{i=1}^{n}\sum_{k=1}^{n}\text{cov}(Z_{2bi},Z_{2ak})}{\sqrt{\sum_{i=1}^{n}\sum_{j=1}^{n}\rho_{Z2ai,Z2aj}\cdot\sigma_{Z2ai}\cdot\sigma_{Z2aj}}\cdot\sqrt{\sum_{i=1}^{n}\sum_{j=1}^{n}\rho_{Z2bi,Z2bj}\cdot\sigma_{Z2bi}\cdot\sigma_{Z2bj}}} \\
&= \frac{\sum_{i=1}^{n}\sum_{k=1}^{n}\rho_{z_{2ai},z_{2bk}}\cdot\sigma_{z_{2ai}}\cdot\sigma_{z_{2bk}}}{\sqrt{\sum_{i=1}^{n}\sum_{j=1}^{n}\rho_{Z2ai,Z2aj}\cdot\sigma_{Z2ai}\cdot\sigma_{Z2aj}}\cdot\sqrt{\sum_{i=1}^{n}\sum_{j=1}^{n}\rho_{Z2bi,Z2bj}\cdot\sigma_{Z2bi}\cdot\sigma_{Z2bj}}}
\end{aligned}
\tag{4.4}
$$

$$
\begin{aligned}
\rho_{Z2,Z1a} &= \frac{\text{cov}[Z_2,Z_{1a}]}{\sigma_{Z2}\sigma_{Z1a}} = \frac{\text{cov}[Z_2,1/n\sum_{i=1}^{n}Z_{2ai}]}{\sigma_{Z2}\sqrt{1/n^2\sum_{i=1}^{n}\sum_{j=1}^{n}\rho_{Z2ai,Z2aj}\cdot\sigma_{Z2ai}\cdot\sigma_{Z2aj}}} \\
&= \frac{\sum_{i=1}^{n}\text{cov}(Z_2,Z_{2ai})}{\sigma_{Z2}\sqrt{\sum_{i=1}^{n}\sum_{j=1}^{n}\rho_{Z2ai,Z2aj}\cdot\sigma_{Z2ai}\cdot\sigma_{Z2aj}}} = \frac{\sum_{i=1}^{n}\rho_{Z2,Z2ai}\cdot\sigma_{Z2ai}}{\sqrt{\sum_{i=1}^{n}\sum_{j=1}^{n}\rho_{Z2ai,Z2aj}\cdot\sigma_{Z2ai}\cdot\sigma_{Z2aj}}}
\end{aligned}
\tag{4.5}
$$

In the above expressions, $\rho_{Z1a,Z1b}$ and $\rho_{Z2,Z1a}$ refer to coarse-to-coarse scale and fine-to-coarse scale correlation coefficients, respectively. The parameters *a* and *b* indicate the index numbers of coarse-scale cells. Equation 4.6 shows the joint distribution expression used in the spatially correlated intra-event sampling by conditional sequential simulation.

$$\begin{bmatrix} Z_n \\ Z_p \end{bmatrix} \sim N(\boldsymbol{\mu},\boldsymbol{\Sigma}) = N\left(\begin{bmatrix} 0 \\ 0 \end{bmatrix}, \begin{bmatrix} \sigma_n^2 & \boldsymbol{\Sigma}_{np} \\ \boldsymbol{\Sigma}_{pn} & \boldsymbol{\Sigma}_{pp} \end{bmatrix}\right) \tag{4.6}$$

The subscripts n and p describe the "next" and "previously" generated intra-event residuals, respectively in Equation 4.6. The vector $\boldsymbol{Z}=[Z_n\ \boldsymbol{Z_p}]$ follows a joint normal distribution with a vector of zero mean and covariance matrix, Σ. The distribution of the next sampled data (Z_n) is a univariate normal distribution conditioned on the previously sampled realizations ($\boldsymbol{Z_p}$) that is given in Equations 4.7 and 4.8.

$$\left[Z_n \mid \boldsymbol{Z}_p = z\right] \sim N\left(\boldsymbol{\Sigma}_{np}\cdot\boldsymbol{\Sigma}_{pp}^{-1}\cdot z, \sigma^2 - \boldsymbol{\Sigma}_{np}\cdot\boldsymbol{\Sigma}_{pp}^{-1}\cdot\boldsymbol{\Sigma}_{pn}\right) \tag{4.7}$$

$$\mathrm{COV}\left[Z_i, Z_j\right] = \rho_{Z_i, Z_j} \cdot \sigma_{Z_i} \cdot \sigma_{Z_j} \tag{4.8}$$

While sampling the intra-event residuals of coarse-scale cells, the covariance matrix ($\sum$) given in Equation 4.8 considers the spatial correlation between two coarse-scale cells as shown in Equation 4.4. The corresponding intra-event standard deviations σ_{Zi} and σ_{Zj} can be calculated from Equation 4.3. If the intra-event residual sampling is for fine-scale cells, the covariance matrix considers the spatial correlation between two fine-scale cells ($\rho_{Z2i,Z2j}$), two coarse-scale cells (Equation 4.4) as well as one coarse-scale cell and one fine-scale cell (Equation 4.5). Accordingly, the intra-event standard deviations in Equation 4.8 would correspond to one of these three cases for the intra-event residual sampling of fine scale cells. These concepts are further clarified in the following paragraphs.
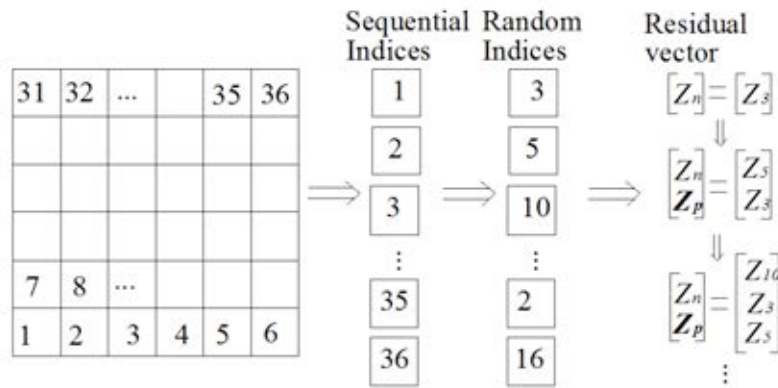
Fig. 4.4 Illustrative example for intra-event residual sampling at coarse-scale level

Fig.4.3 illustrates the generation of intra-event residuals at coarse-scale level. The area of interest is divided into a number of coarse-scale cells and indexed from left-to-right and bottom-to-top as given in the leftmost side of Fig. 4.4. The sequential indices are resorted in a random manner to generate a new sequence of indices (middle part in Fig. 4.4). Following the new order of randomized coarse-scale cells, the intra-event residuals are generated for each cell at the coarse-scale level by using the sequential conditional simulation procedure as summarized in Equations 4.6, 4.7 and 4.8. The intra-event residual of first coarse-scale cell (Z_3 in the illustrative example as given in the rightmost part in Fig. 4.4) is sampled as a univariate normal distribution. The intra-event residual of coarse-scale cell following the first one (Z_5 in Fig. 4.4) is sampled by using the sampled intra-event residual of first coarse-cell (Z_3). In essence, while generating the intra-event residual of the "next" cell, Z_n, the previously generated intra-event residuals become the entries in $\mathbf{Z_p}$. The procedure is recursively repeated until all the intra-event residuals in the coarse-scale cells are sampled.

The intra-event residual simulation of coarse-scale cells is followed by a similar set of simulations at fine-scale level. This process is illustrated in Fig. 4.5 as the continuation of the example case in Fig. 4.4. Although the entire coarse-scale cells can be refined into fine-scale cells to generate the intra-event residuals at the fine-scale level, this process may bring computational burden depending on the size of the area of interest, the number of coarse-scale cells as well as the level of mesh gridding at the fine-scale level (i.e., the number of fine-scale cells in coarse-scale cells). We prefer pre-defining the coarse-scale cells to be refined into fine-scale cells in our procedure. The level of precision in observing the near-fault effects on hazard computations or requirements to be fulfilled in the development of conditional hazard curves can play a role on the number of pre-defined coarse-scale cells for fine-scale mesh gridding. The order of coarse-scale cells to be refined

into fine-scale cells should follow the random indexing used while generating the intra-event residuals of coarse-scale cells. In the follow-up example given in Fig. 4.5, the coarse-scale cells indexed as #2 and #3 are chosen to be refined into fine-scale cells (Fig. 4.5a). Note that the random coarse-scale cell indexing given in Fig. 4.4 indicates that conditional sequential simulation for fine-scale cells should start from coarse-scale cell #3 and should be followed by refining the coarse-scale cell #2. Similar to the indexing technique given in Fig. 4.4, the fine-scale cells in the #2 and #3 coarse-scale cells are numbered from left-to-right and from bottom-to-top as shown in Fig. 4.5a. For this illustrative case, each coarse-scale cell is mesh gridded into 2×2 fine-scale cells. The fine-scale cell indices are then randomized (leftmost part in Fig. 4.5b) to start sequential conditional simulation. For example, the randomized indices of fine-scale cells in the #3 coarse-scale cell are [4, 2, 3, 1]. As presented in the illustrative case in Fig. 4.5, the intra-event residual of the #4 fine-scale cell in the #3 coarse-scale cell ($Z_{3,4}$) is sampled by using Equations 4.6 to 4.8 where Z_p contains all previously sampled coarse-scale cell intra-event residuals. The intra-event residual sampling $Z_{3,2}$, $Z_{3,3}$ and $Z_{3,1}$ is followed after $Z_{3,4}$. After each realization, the corresponding sampled intra-event residual is an entry in Z_p. Upon the sampling of all intra-event residuals in the fine-scale cells of a coarse-scale cell (e.g. #3 coarse-scale cell in Fig. 4.5), it is removed from the previously sampled realizations vector, Z_p. The entire process is repeated until the sampling of all intra-event residuals at fine-scale level is finished in the pre-defined coarse-scale random fields. The following section extends our approach to include near-fault forward directivity effects on the spatially correlated dynamic GMIMs generated via MC-based MSRFs approach.
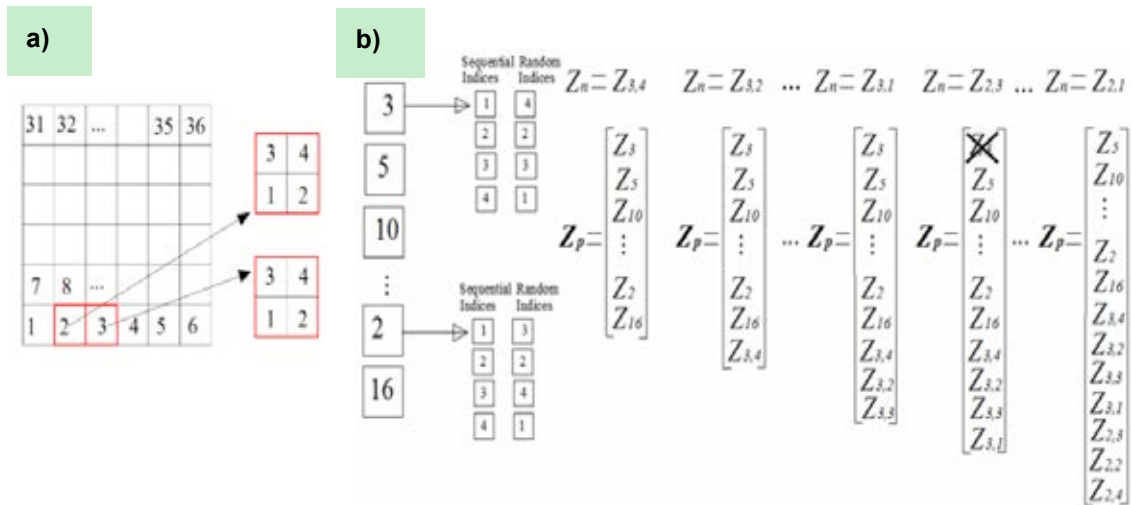
Fig. 4.5 Generation of intra-event residuals for fine-scale cells: a) pre-selected coarse-scale cells for refining into fine-scale cells (designated by red boxes) and numbering of fine-scale cells in these coarse-scale cells, b) sequential conditional simulation process

We note that the MSRFs approach sample the spatially correlated residuals and GMIMs at the centroids of the grids. Therefore, the computation of GMIMs at locations within the grids require additional computational effort and assumptions. One can assume that the central GMIMs apply uniformly within the grids that imply a perfect spatial correlation within the cell. The accuracy of hazard computed under this assumption is related to the grid size: smaller grid sizes would increase the accuracy of hazard at sites far from the centroids of the grids. Smaller grids would also allow the expert to use a proper interpolation method (inverse

distance weighting, kriging, etc.) to interpolate the central GMIMs for other sites within the grids. Alternatively, one can use grid-to-grid correlation and grid variance (Stafford, 2012) instead of point-to-point correlation or GMPE variance as presented in Equations 4.3 to 4.5. Our analysis from the implementation of Stafford's (Stafford, 2012) grid variance expression indicate that a grid size of 1km × 1km would yield almost equal point and grid variances. Thus, the use of such a grid dimension for the computation of central hazard in a cell would resemble the hazard for sites anywhere within that cell. Needless to say these alternative methods to estimate GMIM distribution at sites other than the centers of the cells would increase the computational burden that is also valid for any MC-based probabilistic hazard assessment method. In their paper, Bal et al. (2010) discuss the trade-offs between grid size, hazard accuracy and computer time that highlight important points for an efficient and accurate computation in MC-based hazard studies. The case studies in this chapter only consider the hazard computed at the center of the cells.

4.2.1.1 *Near-fault directivity effects*

When the rupture and slip direction relative to a site coincide and a significant portion of the fault ruptures towards the site, the ground motion can exhibit the effects of forward directivity (short duration ground motions that consist of one or more pulses). Most of the conventional GMPEs do not model forward directivity so seismic hazard assessment via conventional ground-motion characterization may fail to estimate the near-fault ground-motion amplitudes for future earthquakes. We implemented the near-fault directivity model of Shahi and Baker (2011) to account for the likely change of ground-motion amplitudes in the vicinity of faults. The Shahi and Baker model predicts the probability of pulse-like ground motions occurring at a site by considering the orientations of induced seismic waveforms relative to the strike of the fault. It amplifies the spectral ordinates in the vicinity of pulse period, T_p, by empirically calibrating the median and standard deviations of ground-motion estimates from conventional GMPEs. Strictly speaking the Shahi and Baker (2011) model requires a spatial correlation function that is explicitly developed for near-fault effects. To our knowledge, there is no such spatial correlation function to explicitly account for the near-fault effects. Thus, the simultaneous use of a spatial correlation function that disregards near-fault effects and a forward directivity model to tailor spectral ordinates for forward directivity pulses would overemphasize the spatial correlation in the vicinity of the fault. The reader should consider this fact while implementing the proposed approach for the assessment of hazard in the close proximity of faults.

Fig. 4.6 shows the overall algorithm for incorporating the near-fault directivity effects to the spatially correlated GMIMs generated via MSRFs approach. In essence, we modify the intra-event standard deviation of the conventional GMPE to sample the spatially correlated intra-event residuals for sites (coarse and fine-scale cells) located in the near-fault region. Considering T_p, we also modify the median estimates of GMIMs for these sites obtained from the conventional GMPE. For each realization of MC simulations (i.e., for each scenario event), we determine the probability of observing a pulse at a certain orientation α [P(pulse at α|pulse)] for the mid-point of the cells that are located in the vicinity of fault. P(pulse at α|pulse) is related to the relative location of the centroid of the cell with respect to the fault strike. We sample this value using binomial distribution. If the forward directivity is more likely to occur (Pulse case), we sample T_p assuming log-normal distribution. The value of sampled T_p leads to the calibration of median ground motion and associated standard

deviation of conventional GMPE to generate spatially correlated random fields. The Shahi and Baker (2011) model disregards the calibration of median ground motion and associated standard deviation if $T_p < 0.6$s. If no pulse case is dominant, then depending on the spectral period (T) of GMIM, this model either uses the median ground-motion estimates and standard deviation of conventional GMPE ($T \leq 1.0$s case) or modifies these parameters. The calibrated standard deviations and median ground-motion estimates are used for generating spatially correlated GMIMs at coarse- and fine-scale levels. As the MSRFs method considers the centers of the cells for sampling GMIMs, the distribution of GMIMs due to near-fault effects would be more accurate with smaller grid sizes at the expense of increased computational burden.
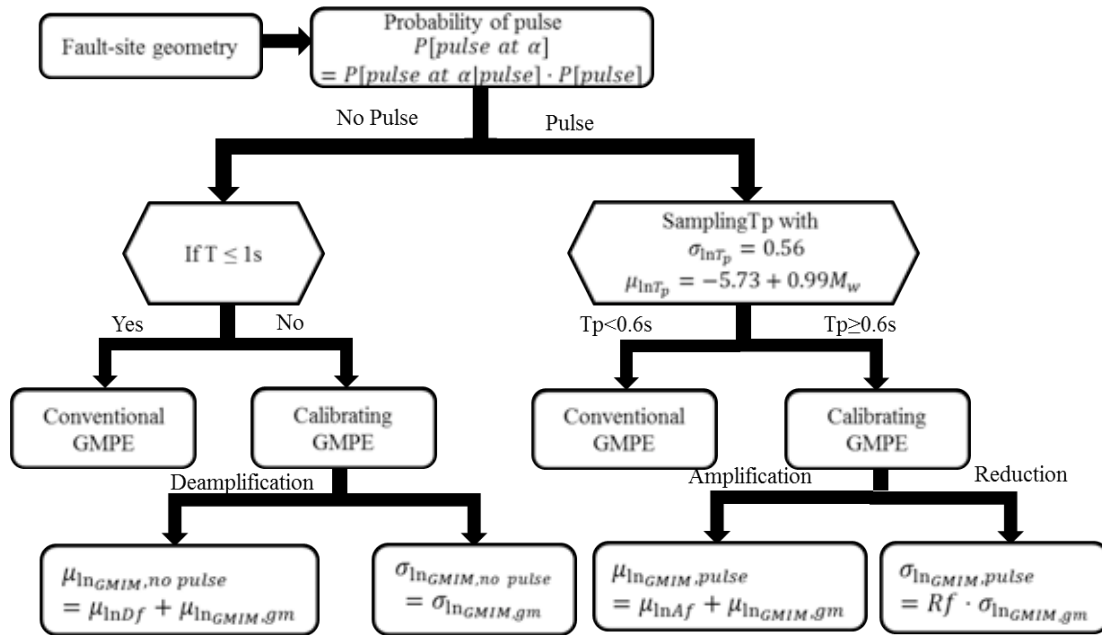
Fig. 4.6 Algorithm for considering near-fault forward directivity effects on the spatially correlated GMIMs generated from MSRFs approach. $\mu_{lnGMIM,pulse}$ **is the calibrated mean GMIM in logarithmic space due to pulse-like ground motions (forward directivity).** μ_{lnAF} **is the logarithmic calibration factor for forward directivity effects and** $\mu_{lnGMIM,gm}$ **is the mean GMIM in logarithmic space computed from conventional GMPE. In a similar manner,** $\sigma_{lnGMIM,pulse}$ **and** $\sigma_{lnGMIM,gm}$ **are the calibrated and original standard deviations of conventional GMPE, respectively.** *Rf* **is the calibration factor for standard deviation for forward directivity effects. For non-pulse case,** $\mu_{lnGMIM,nonpulse}$ **is the calibrated mean GMIM in logarithmic space due to non-pulse-like ground motions.** μ_{lnAF} **and** $\sigma_{lnGMIM,nonpulse}$ **are the logarithmic calibration factor and standard deviation of GMPE for backward directivity effects, respectively.**

The Shahi and Baker model provides calibration factors for the total standard deviation of a conventional GMPE that can be used for generating total residuals. Since the MSRFs approach requires intra-event standard deviation ($\sigma_{\varepsilon,gm}$) to sample intra-event residuals, we modify the calibration factor proposed in Shahi and Baker as given in Equations 4.9 and 4.10. We assume that the inter-event standard deviation ($\sigma_{\eta,gm}$) does not change for any given simulated scenario earthquake. This assumption is rational as inter-event standard deviation is constant for a specific earthquake. The modified calibration factor is indicated as

$Rf_{\varepsilon,\ pulse}$ in the derivations and replaces R_f (see the last row of "Pulse" case in Fig. 4.6) while considering the near-fault directivity effects in the MSRFs approach. Note that $\sigma_{\eta,gm}$ and $\sigma_{\eta,pulse}$ are equal to each other in the derivations under constant inter-event standard deviation assumption.

$$Rf^2 = \frac{\sigma^2_{t,pulse}}{\sigma^2_{t,gm}} = \frac{\sigma^2_{\varepsilon,pulse} + \sigma^2_{\eta,pulse}}{\sigma^2_{\varepsilon,gm} + \sigma^2_{\eta,gm}} = \frac{\sigma^2_{\varepsilon,pulse}/\sigma^2_{\varepsilon,gm} + \sigma^2_{\eta,pulse}/\sigma^2_{\varepsilon,gm}}{1 + \sigma^2_{\eta,gm}/\sigma^2_{\varepsilon,gm}} \tag{4.9}$$

$$= \frac{Rf^2_{\varepsilon,pulse} + \sigma^2_{\eta,pulse}/\sigma^2_{\varepsilon,gm}}{1 + \sigma^2_{\eta,gm}/\sigma^2_{\varepsilon,gm}} = \frac{Rf^2_{\varepsilon,pulse} + \sigma^2_{\eta,gm}/\sigma^2_{\varepsilon,gm}}{1 + \sigma^2_{\eta,gm}/\sigma^2_{\varepsilon,gm}}$$

$$\Rightarrow Rf_{\varepsilon,pulse} = \sqrt{(1 + \sigma^2_{\eta,gm}/\sigma^2_{\varepsilon,gm}) \cdot Rf^2 - \sigma^2_{\eta,gm}/\sigma^2_{\varepsilon,gm}} \tag{4.10}$$

The spatial correlation expression, $\rho_{\eta,gm}$, (Sokolov and Wenzel, 2011; Wesson and Perkins, 2001) in Equation 4.11 can be used together with Equation 4.10 to express $Rf_{\varepsilon,\ pulse}$ as given in Equation 4.12.

$$\rho_{\eta,gm} = \sigma^2_{\eta,gm}/(\sigma^2_{\varepsilon,gm} + \sigma^2_{\eta,gm}) \tag{4.11}$$

$$Rf_{\varepsilon,pulse} = \sqrt{(Rf^2 - \rho_{\eta,gm})/(1 - \rho_{\eta,gm})} \tag{4.12}$$

4.2.1.2   Development of hazard curves from MC-based MSRFs approach

We generate a suite of synthetic earthquake catalogs for a given fault located in the area of interest. The synthetic catalogs are based on a specific earthquake recurrence model that represents the temporal distribution of seismic activity in the considered fault for a certain catalog period. In essence, simulating a suite of synthetic earthquake catalogs having magnitude frequency distributions similar to the one dictated by the earthquake recurrence model and covering a long time span sufficiently addresses the low annual exceedance rates of earthquakes originating from the considered fault. This approach has been used by Musson (2000) and Assatourias and Atkinson (2013) in MC-based PSHA. Musson (2000) indicated that a suite of 1000 synthetic catalogs, each spanning a 100-year time interval (i.e., a total duration of 100,000 years) would yield reliable estimates of GMIMs for annual exceedance rates of 10^{-3}. When the total catalog duration is extended to 1,000,000 years (i.e., 10000 synthetic catalog, each covering 100-year period), the accurate annual exceedance rates for GMIMs become 10^{-4}. Similar findings are also published by Assatourias and Atkinson (2013) as well as Crowley and Bommer (2006). The latter paper considers all stochastic events in a single earthquake catalog with a very long time interval.

Our synthetic catalog simulations assume Poissonian process for earthquake occurrence. The earthquakes generated in each artificial catalog are assumed to occur randomly on the fault with a uniform distribution along the fault strike and within the seismogenic depth. For each scenario event in the artificial earthquake catalogs, we implement MSRFs approach to sample spatially correlated intra-event residuals at coarse- and fine-scale levels. The intra-event residuals are sampled at the centers of coarse-scale and fine-scale cells and consider the near-fault directivity effects depending on the relative location of the site (centroid of the cell) with respect to fault geometry. We obtain the total residual at each cell by considering the contribution of inter-event residual specific to the scenario event. The inter-event residuals are computed from the inter-event standard deviation of the GMPE used in the computations. They are sampled as normal varieties in our procedure. The logarithmic mean

(median) predictions of GMIMs that are computed at the centers of coarse-scale and fine-scale cells are superposed with the total residuals to obtain the spatially correlated GMIM distribution within the entire random field. As in the case of intra-event residual sampling, the median GMIM predictions are modified for near-fault directivity effects depending on the center point of the cell and fault locations at coarse- and fine-scale levels.

The procedure described in the above paragraph is itemized in the following steps.

1. Define the area of interest together with the fault segment that affects the seismicity in the entire area. Subdivide the area into coarse-scale and fine-scale cells. The decision on the cell resolution (size) depends on many factors as MSRFs approach sample the GMIMs at the centroids of the cells. The clustering of geographically distributed portfolio and precision required to address the near-fault directivity effects are among the important factors that affect the cell size.

2. Chose a GMPE that is suitable for the tectonic environment as well as the seismicity in the area of interest. Equation 4.13 shows the essential components of a GMPE that are of relevance to our discussions.

$$\ln\left(GMIM_{i,j}\right) = f\left(M_i, R_{i,j}, \boldsymbol{\theta}\right) + \eta_i + \varepsilon_{i,j}; \qquad i = 1, \dots m, \ j = 1, \dots n \qquad (4.13)$$

The first term on the left-hand-side predicts the logarithmic mean of the $GMIM_{i,j}$ of interest for the *ith* earthquake and *jth* site (designated as $\mu_{lnGMIM,gm}$ in the previous discussions). M_i and $R_{i,j}$ are the magnitude and source-to-site distance terms of the *ith* earthquake and the *jth* site (centroid of the cell). The vector $\boldsymbol{\theta}$ contains other seismological estimator parameters to define, for example, site conditions at the *jth* site and style-of-faulting specific to the *ith* earthquake. The random varieties η_i and $\varepsilon_{i,j}$ represent the inter-event and intra-event variability in the predicted $GMIM_{i,j}$, respectively. They are normally distributed with inter-event ($\sigma_{\eta,gm}$) and intra-event ($\sigma_{\varepsilon,gm}$) standard deviations. Note that *m* and *n* in Equation 4.13, represent the total number of simulations and sites (cells) at coarse- and fine-scale levels, respectively. The total number of simulations is related to the number of earthquakes in the artificially generated earthquake catalogs.

3. Generate a suite of earthquake catalogs by following the properties of earthquake recurrence specific to the fault. The number of earthquake catalogs should be sufficient enough to consider the occurrence of rare events (low annual exceedance rates) for proper temporal distribution of earthquakes. Currently, the spatial distribution of earthquakes is defined by the uniformly distributed rupture planes and the hypocentral location of each earthquake is assumed to be at the center of the ruptured surface. The multi-segment or bending ruptures are disregarded in the implementation of the proposed approach.

4. For scenario event i, sample spatially correlated $\varepsilon_{i,j}$ using MSRFs approach. Make necessary calibrations for near-fault directivity effects at coarse-scale and fine-scale levels whenever necessary.

5. For scenario event i, compute the logarithmic mean of $GMIM_{i,j}$ ($\mu_{lnGMIM,gm}$) at coarse-scale and fine-scale levels. Make necessary calibrations for near-fault directivity effects (i.e., modify $GMIM_{i,j}$ either for $\mu_{lnGMIM,pulse}$ or $\mu_{lnGMIM,nonpulse}$) depending on the location of the centroid of the cell with respect to the fault, T_p and spectral period (T) of $GMIM_{i,j}$.

6. For scenario event i, compute η_i.

7. Combine the spatially correlated $\varepsilon_{i,j}$, $GMIM_{i,j}$ and η_i using Equation 4.13. The product is the spatially correlated $GMIM_{i,j}$ in the logarithmic domain at coarse- and fine-scale levels.

8. Repeat steps 4 to 7 for the simulated suite of earthquake catalogs and compute the hazard curves for the cells at coarse- and fine-scale levels from Equation 4.14.

$$\lambda_j(GMIM \geq GMIM_0) = \frac{total\ number\ of\ GMIM \geq GMIM_0\ at\ cell\ j}{total\ number\ of\ simulated\ earthquake\ catalogs \times catalog\ period} \tag{4.14}$$

In Equation 4.14, $\lambda_j(GMIM \geq GMIM_0)$ is the mean annual rate of GMIM of interest exceeding a threshold level $GMIM_0$ for cell j. Computation of $\lambda_j(GMIM \geq GMIM_0)$ for a range of $GMIM_0$ will yield the hazard curve at cell j. We note that the computation of hazard curves by MC-based MSRFs approach is described by considering a single fault source. If the area of interest is exposed to k multiple faults, this procedure is repeated for the other faults. The mean annual exceedance rates computed from all sources are then summed up to obtain the final mean annual exceedance rate at cell j.

$$\lambda_j(GMIM \geq GMIM_0) = \sum_{l=1}^{k} \lambda_{l,j}(GMIM \geq GMIM_0) \tag{4.15}$$

The concept introduced by Equation 4.15 can form the basis of MC-based hazard for areal sources. The uncertainty in the location and orientation of faults in areal sources can be represented by a set of virtual fault ruptures at which MC-based simulations can be repeated for each fictitiously oriented fault rupture. The total mean annual exceedance is computed at each cell by summing the contribution of hazard from each fictitious rupture.

Computation of conditional hazard

The discussions in the previous sections describe the theory and implementation of MC-based MSRFs approach for the seismic hazard assessment of a single GMIM. The conditional seismic hazard assessment, however, is sometimes more critical for geographically distributed structural portfolio and infrastructures because the seismic performance of some of their components require the consideration of multiple GMIMs. The conditional hazard assesses the exceedance rate of the secondary GMIMs conditioned on the occurrence of primary GMIM. The secondary GMIMs can be either single or multiple. In case there are multiple secondary GMIMs, they are called as first-secondary GMIM, second-secondary GMIM and so forth. The primary and secondary GMIMs are related to each other by cross-correlation coefficients, $\rho_{IMi,IMj}$ (e.g. Baker and Jayaram, 2008; Akkar et al., 2014a, 2014b).

The conventional conditional hazard assessment cross-correlates each secondary GMIM with the primary GMIM to compute the conditional exceedance rate of the secondary GMIM (Iervolino et al., 2010). The proposed procedure herein establishes a different structure: each secondary GMIM is cross-correlated with the primary and previously generated secondary GMIMs for the conditional exceedance rate of the secondary GMIMs. This way the interdependence of primary and secondary GMIMs is more realistically mapped on to the conditional exceedance rates. The procedure does not change for the primary GMIM. We

generate the spatially correlated intra-event residuals and sum them up with the independently sampled inter-event residuals to obtain the total residual distribution at coarse- and fine-scale levels for the entire earthquake scenarios of the simulated earthquake catalogs. The total residual sampling of secondary GMIMs is based on the total residual distribution of the primary GMIM and they are generated via sequential conditional simulation. The total residuals of the primary and secondary GMIMs have joint multivariate normal distribution as described in Equations 4.16 and 4.17.

$$\begin{bmatrix} Z_{IMn} \\ \boldsymbol{Z}_{IMp} \end{bmatrix} \sim N\left(\boldsymbol{\mu}, \boldsymbol{\Sigma}\right) = N\left(\begin{bmatrix} 0 \\ \mathbf{0} \end{bmatrix}, \begin{bmatrix} \sigma^2_{IMn} & \boldsymbol{\Sigma}_{IMnp} \\ \boldsymbol{\Sigma}_{IMpn} & \boldsymbol{\Sigma}_{IMpp} \end{bmatrix} \right) \tag{4.16}$$

$$\mathrm{COV}\left[Z_{IMi}, Z_{IMj} \right] \sim \rho_{Z_{IMi}, Z_{IMj}} \cdot \sigma_{Z_{IMi}} \cdot \sigma_{Z_{IMj}} \tag{4.17}$$

Equations 4.16 and 4.17 have a format similar to Equations 4.6 and 4.8, respectively. Z_{IMn} refers to the next generated total residual of secondary GMIM whereas $\boldsymbol{Z}_{IMp}$ is the vector of previously generated primary and secondary GMIMs. In a similar manner, σ_{IMn} is the total standard deviation of the next generated secondary GMIM and $\sum_{IMnp}$ as well as $\sum_{IMpn}$ are the covariance vectors of the previous and next GMIMs, respectively. The covariance matrix of the previously generated GMIMs is designated as $\sum_{IMpp}$. Note that the covariance terms in Equation 4.16 contain the previously generated primary and secondary GMIMs as the proposed approach accounts for the interdependency between these varieties. The covariance relationship to be used between the secondary and primary, primary and primary as well as secondary and secondary GMIMs are given in Equation 4.17. In this expression, $\rho_{IMi,IMj}$ is the cross-correlation coefficient between GMIM_i and GMIM_j where they can be primary and secondary, both secondary or both primary GMIMs. σ_{ZIMi} and σ_{ZIMi} refer to the corresponding total standard deviations. As explained in the previous sections the standard deviation information comes from the GMPE used in the overall process. The total residual distribution can further be expressed as a univariate normal distribution for the next generated GMIM as given in Equation 4.18, which is analogous to Equation 4.7 used in the inter-event residual sampling of primary GMIM.

$$\left[Z_{IMn} \mid \boldsymbol{Z}_{IMp} = z \right] \sim N\left(\boldsymbol{\Sigma}_{IMnp} \cdot \boldsymbol{\Sigma}^{-1}_{IMpp} \cdot z, \sigma_{IMn}^{2} - \boldsymbol{\Sigma}_{IMnp} \cdot \boldsymbol{\Sigma}^{-1}_{IMpp} \cdot \boldsymbol{\Sigma}_{IMpn} \right) \tag{4.18}$$

In Equation 4.18 $\boldsymbol{Z}_{IMp}$ is the total residual realizations of the previous GMIMs. Note that we describe the proposed procedure to sample cross-correlated total residuals. If the considered GMPE provides information about the cross-correlation models of intra- and inter-event residuals separately, it can be modified to sample the cross-correlated intra- and inter-event residuals simultaneously to obtain the hazard rate of secondary GMIMs conditioned on the primary GMIM.

In essence, our procedure for conditional hazard assessment uses the previously generated primary GMIM to sample the total residuals of secondary GMIMs. If there is a second-secondary GMIM, its total residuals are sampled by the cross-correlations of primary, first-secondary and second-secondary GMIMs. This process continues for the entire set of secondary GMIMs. The conditional hazard of each secondary GMIM is then developed by following the conventional approach given in Equation 4.14. If there is one secondary GMIM, the normal distribution of total residuals of the secondary GMIM will have the following mean ($\mu_{IM2|IM1}$) and standard deviation ($\sigma_{IM2|IM1}$):

$$\mu_{IM2|IM1} = \rho_{IM1,IM2} \sigma_{IM2} \frac{\varepsilon}{\sigma_{IM1}} \tag{4.19}$$

$$\sigma_{IM2|IM1} = \sigma_{IM2}\sqrt{1-\rho_{IM1,IM2}^2} \tag{4.20}$$

In Equation 4.19, ε is the previously sampled total residual of primary GMIM and $\rho_{IM1,IM2}$ is the cross-correlation coefficient between the primary and secondary GMIMs. Fig. 4.7 illustrates this specific case to develop the hazard curve of the secondary GMIM conditioned on the primary GMIM for the centroid of each cell. We note that the proposed procedure assumes that the correlation distances of the secondary IMs are the same as that of primary IM. Therefore, it is suggested to choose the primary IM as the one with larger correlation length with respect to the correlation distances of secondary IMs (Weatherill et al., 2015).
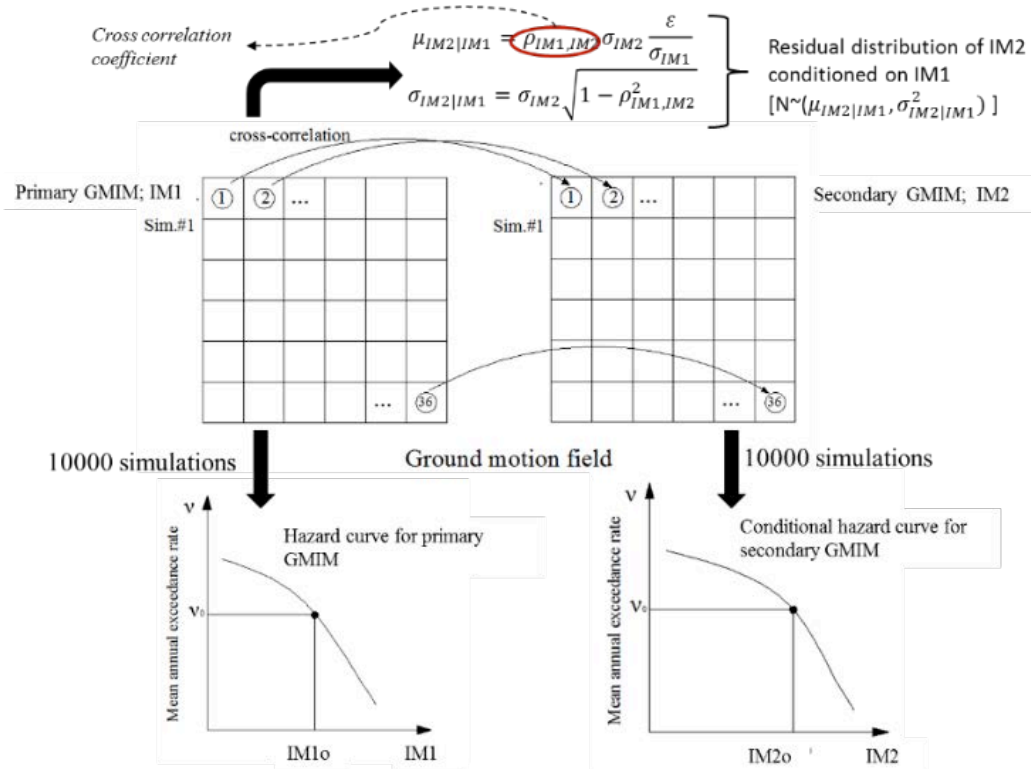
Fig. 4.7 Graphical illustration of conditional hazard assessment for one secondary GMIM

4.2.2 Monte-Carlo based hazard for permanent fault displacement

Geographically distributed systems (e.g. gas, water, oil pipelines, highway networks, large span bridges or large building stocks covering a wide geographical area) can be exposed to severe damage if the faults crossing their footprints rupture at the surface leaving permanent deformations. The permanent fault displacements are generally estimated deterministically from empirical surface rupture vs. magnitude relationships (e.g. Wells and Coppersmith, 1994). Inspiring from conventional PSHA, Youngs et al. (2003) conducted the first pioneering study for assessing probabilistic fault displacement hazard (PFDHA) to expresses the annual exceedance rates of fault displacements at different thresholds. This approach is improved by Petersen et al. (2011) for strike-slip faults by including the mapping accuracy and complexity of the fault trace. Petersen et al. (2011) model considers the likely occurrence of on-fault (*D*) and off-fault (*d*) displacements where the former displacement occurs on the major ruptured fault and the latter displacement typically represents discontinuous shear-failures at locations far from the principal fault.

The ruptured fault segment and site geometry used in Petersen et al. (2011) model are presented in Fig. 4.8. The site is represented as a square cell having a dimension of z and x, y denote the coordinates of the center of the site. r is the perpendicular distance from the rupture length, L. l denotes the distance measured from the nearest point on the rupture to the closest end of the rupture whereas s is the distance from the end of the rupture to the end of the fault. The dashed lines in Fig. 4.8 mimic the potential deviations in the rupture from the mapped fault due to mapping inaccuracy and complexity of the main fault trace. The deviations from the mapped fault trace can be represented either as a single or multiple offsets normal to the strike of the mapped fault. An alternative way of modeling the mapping accuracy is to use distributed offsets on both sides of the mapped fault trace. The former approach assumes a full spatial correlation between the mapped and inferred fault trace that may fail to represent the actual fault rupture pattern. Therefore, the latter method can be considered as more realistic. However, we prefer implementing the former mapping inaccuracy model because the lack of a proper correlation expression to address the ruptured fault deviations from the mapped fault may lead to unrealistic patterns in ruptured fault traces. Besides the surface rupture of strike-slip faults (faulting style considered by Petersen et al., 2011) are generally straight with small deviations that is comparable to our simple model. Therefore, until the development of reliable correlation models about surface rupture patterns, we prefer assuming a full spatial correlation to account for mapping inaccuracy.
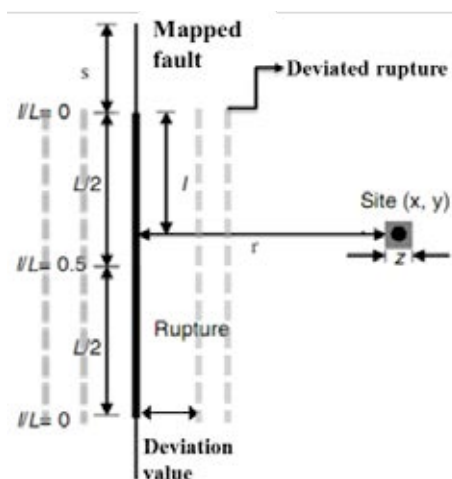
Fig. 4.8 Ruptured fault and site geometry in Petersen et al. 2011 for their proposed PFDHA model for strike-slip events.

The annual exceedance rate of on-fault displacement $\gamma(D \geq D_0)$ is considered by integrating different probabilities in Petersen et al. (2011). These probabilistic terms include (1) the uncertainty in rupture location due to random variation of rupture along the fault as well as the fault complexity and mapping inaccuracy, $f(r)$; (2) the joint probability to characterize the relation between earthquake magnitude (m) and rupture location (s), $f_{M,S}(m,s)$; (3) the probability of observing surface rupture (sr) conditioned on earthquake magnitude, $P(sr \neq 0|_m)$; (4) given a nonzero surface rupture the probability of observing a nonzero on-fault displacement at a site of dimension z, $P(D \neq 0|_{z, sr \neq 0})$ and (5) the probability of on-fault displacement exceeding a threshold D_0 conditioned on rupture geometry and earthquake size, $P(D \geq D_0|_{l/L, m, D \neq 0})$. The last conditional probability is lognormal and is developed from a predictive model that estimates on-fault displacements from empirical data. The annual

exceedance rate of off-fault displacement $\gamma(d \geq d_0)$ is computed in a similar manner. The first three probabilities described for $\gamma(D \geq D_0)$ are also considered in $\gamma(d \geq d_0)$. In the computation of $\gamma(d \geq d_0)$, the probability of nonzero off-fault displacement given a nonzero surface rupture $[P(d \neq 0|_{r, z, sr \neq 0})]$ not only depends on the size of the site (z) but also on the perpendicular distance, r, between the site and the rupture. This is because the discontinuous off-fault displacements are expected to occur away from the fault due to shears and fractures in the vicinity of principle rupture. The empirical GMPE to describe the probability of off-fault displacement exceeding a threshold d_0 $[P(d \geq d_0|_{r, m, d \neq 0})]$ is a function of r and m for $\gamma(d \geq d_0)$. The next paragraph explains the integration of these probabilities to MC-based permanent fault displacement hazard. The reader is referred to Petersen et al. (2011) and Youngs et al. (2003) to compare our approach with the probabilistic fault displacement hazard integral presented in the above cited publications.
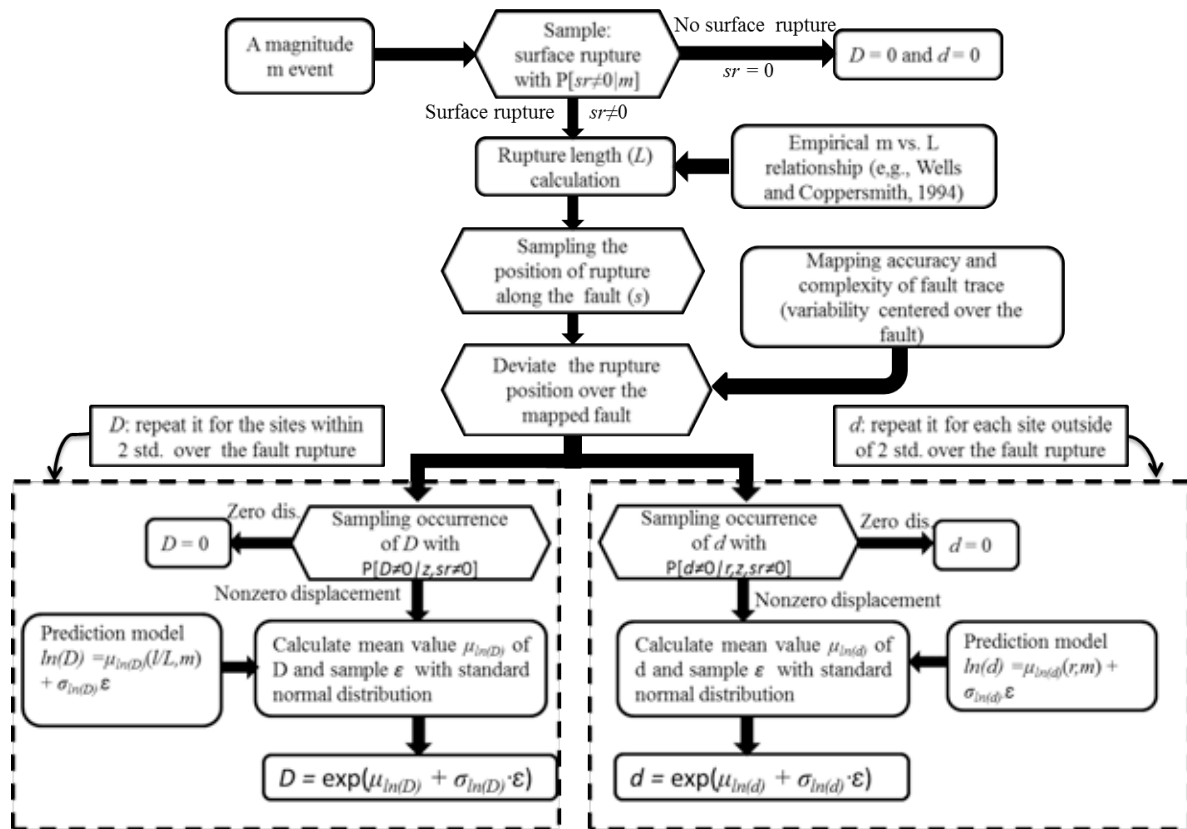
Fig. 4.9 Proposed MC-based permanent fault displacement hazard assessment procedure

Our MC-based permanent fault displacement hazard assessment starts with the generation of synthetic earthquake catalogs to reflect the temporal seismicity of the subject fault. The procedure for generating synthetic catalogs is the same as described in Section 4.2.1.2: each synthetic catalog contains a series of events that follows the designated magnitude recurrence model within the predefined catalog period. For each event in the synthetic catalog, Fig. 4.9 shows the proposed procedure to generate probabilistic on-fault and off-fault displacements at the centroids of the cells covered by the region of interest. The grid size is z (varying from 25 m to 200 m in Petersen et al. (2011) to account for different levels of accuracy in rupture probability) and mesh gridding is done within several hundred meters (e.g. 150 m) from each side of the fault because fault displacements decay rapidly with increasing distance from the ruptured fault segment. Thus, we do not generate grids for the entire region as in the case of MC-based MSRFs implemented for dynamic GMIMs.

We first compute the conditional probability of observing surface rupture on the fault, $P(sr \neq 0|_m)$, for each scenario event with a designated magnitude m in the earthquake catalog (Equation 4.21).

$$P(sr \neq 0|_m) = \frac{e^{(-12.51+2.053m)}}{1+e^{(-12.51+2.053m)}} \tag{4.21}$$

The conditional probability follows Bernoulli distribution that samples the "success" ($sr \neq 0$) or "failure" ($sr = 0$) of a random event under the computed probability given in Equation 4.21. If Bernoulli distribution samples "failure", both on- and off-fault displacements are zero for that scenario event. If the earthquake with surface rupture is sampled, an empirical m vs. L scaling relationship is used (e.g. Wells and Coppersmith, 1994) to determine the rupture length, L. The rupture position (s) is randomly placed along the entire fault assuming a uniform distribution. The likely deviation in the rupture location from the mapped fault trace due to mapping uncertainty and fault complexity is determined from a two-sided normal probability distribution proposed by Petersen et al. (2011) (see Tables 2 and 3 in the referred article). After determining the final location of the ruptured segment, the on- and off-fault displacements are generated as given in the dashed boxes in Fig. 4.9. The random generation of on- and off-fault displacements start with the consideration of probabilities $P(D \neq 0|_{z, sr \neq 0})$ and $P(d \neq 0|_{r, z, sr \neq 0})$. These probabilities are expressed as power functions and are given in a tabular format in Petersen et al. (2011) for different grid sizes. They also follow Bernoulli distribution and if the Bernoulli distribution samples "failure" for any one of these probabilities, the corresponding fault displacement is taken as zero. (In practice, $P(D \neq 0|_{z, sr \neq 0})$ can be taken as unity and Bernoulli distribution samples "success" whenever a non-zero surface rupture is generated). Otherwise, the on- and off-fault displacements are estimated from the proposed empirical GMPEs by Petersen et al. (2011). The generic forms of these GMPEs are given in Equations 4.22 and 4.23.

$$\ln(D) = \mu_{ln(D)}(l/L, m) + \varepsilon \sigma_{ln(D)}) \tag{4.22}$$

$$\ln(d) = \mu_{ln(D)}(r, m) + \varepsilon \sigma_{ln(d)}) \tag{4.23}$$

$\mu_{ln(D)}$ and $\mu_{ln(d)}$ are the logarithmic mean estimates of on- and off-fault displacements, respectively. $\sigma_{ln(D)}$ and $\sigma_{ln(d)}$ describe the logarithmic standard deviations associated with the on- and off-fault displacement GMPEs, respectively. ε designates the number of standard deviations above or below the logarithmic mean estimates. Consistent with the conventional wisdom in GMPEs, D and d are log-normal varieties whereas ε is normally distributed in the above expressions. Petersen et al. (2011) propose three alternative predictive equations to estimate on-fault displacements depending on the observed data from the past strike-slip earthquakes. These equations are strictly valid for on-fault sites (cells) after considering the mapping uncertainty and fault complexity while determining the location of ruptured segment on the principal fault. The off-fault displacement predictive model is used at the sites (cells) encircling the major ruptured fault segment. The off-fault sites are only within few hundred meters from both sides of the ruptured fault segment due to rapid decay of fault displacements with distance.

The procedure given in Fig. 4.9 is repeated for all the earthquakes in the generated synthetic catalogs to compute the on- and off-fault displacement distributions at the centroid of each cell. The annual exceedance rates of on-fault and off-fault displacements at each cell for predefined threshold levels are determined from the following expressions that are similar to Equation 4.14.

$$\lambda_j(D \geq D_0) = \frac{total\ number\ of\ D \geq D_0\ at\ site\ j}{total\ number\ of\ simulated\ earthquake\ catalogs \times catalog\ period} \qquad (4.24)$$

$$\lambda_j(d \geq d_0) = \frac{total\ number\ of\ d \geq d_0\ at\ site\ j}{total\ number\ of\ simulated\ earthquake\ catalogs \times catalog\ period} \qquad (4.25)$$

In Equations 4.24 and 4.25 j refers to the cell index whereas D_0 and d_0 are the threshold on-fault and off-fault displacements, respectively. The on-fault and off-fault displacement hazard curves at cell j are obtained from the computation of $\lambda_j(D \geq D_0)$ and $\lambda_j(d \geq d_0)$ for a set of D_0 and d_0, respectively. The total permanent displacement hazard curve at cell j is the sum of on- and off-fault hazard curves corresponding to cell j.

4.2.3 Case studies

We present several case studies to show the implementation and implications of the theory discussed in this article. The case studies intend to emphasize the flexibility and robustness of MC-based simulations for probabilistic hazard assessment of dynamic GMIMs and permanent fault displacement. We used our own Matlab^{TM} codes while running the case studies. We validated our codes by comparisons with the results of open-source seismic hazard software, OpenQuake (http://www.globalquakemodel.org/openquake) and journal papers (by contacting their authors). The details of case studies are given in the following subsections. The seismic sources are represented as fault segments in the case studies although they could also be chosen as area sources with some modifications in the procedures discussed in Section 4.2.1.

4.2.3.1 Case studies concerning dynamic GMIMs

Fig. 4.10 shows the results of the validation of our codes for a fictitious 90° dipping strike-slip fault segment of length 85 km. We consider pure-characteristic earthquake recurrence model with characteristic magnitudes ranging between M_w 7 and M_w 7.5 (uniformly distributed probabilities of occurrence between M_w 7 and M_w 7.5). The annual slip rate is assumed as 15 mm/year for the fictitious fault. We ran 10,000 simulations with a 100-year catalog period (total catalog period is 1,000,000 years) to obtain reliable hazard results for mean annual exceedance rates of about10^{-4} (Musson, 2000). We used Akkar et al. (2014a, 2014b) GMPE to characterize the ground-motion amplitudes in the hazard analyses. The same fictitious scenario is modeled in OpenQuake using the conventional PSHA (Cornell1968; McGuire, 1976) to validate the reliability of our computations. OpenQuake is recognized as one of the trustworthy software in PSHA among its counterparts (Pagani et al., 2014). Our results and the results from OpenQuake are compared for PGA hazard curves at the randomly selected rock sites (see upper right corner in Fig. 4.10 for the relative locations of sites with respect to the fault). The results computed by our codes agree well with OpenQuake for mean annual exceedance rates up to 10^{-4}. We repeated similar verification studies for different dynamic GMIMs and sites with locations different than those given in this exercise. These comparisons advocate the reliability of our codes to discuss how different levels of complexity (directivity, spatial correlation, conditional hazard etc.) are treated by MC-based approaches for probabilistic hazard assessment.

Similar to the above validation example, the following case studies use a 90° dipping strike-slip fault although our codes can run hazard analyses for other styles of faulting. The fault

length is 85 km and its seismogenic depth is taken as 15 km. The fictitious fault is assumed to have a slip rate of 15 mm/year producing characteristic earthquakes of M_w 7.0 to M_w 7.5. In all case studies, we used a 100-year catalog period and ran 10,000 simulations that results in a total catalog interval of 1,000,000 years. The spatial correlation model of Jayaram and Baker (2009) is utilized for the interdependency of dynamic GMIMs at closely spaced sites. The Akkar et al. (2014c, 2014d) GMPE and the Akkar et al. (2014a, 2014b) cross-correlation coefficients are used for ground-motion characterization and conditional hazard computations, respectively. These two studies use the same strong-motion database to develop the ground-motion predictive model and the correlations between the spectral ordinates. The site condition is fixed in all case studies and is represented by V_{S30} = 720 m/s. The size of coarse cells is chosen as 0.1°×0.1° and they are refined by 4×4 fine scale cells at sites closer to the fault.
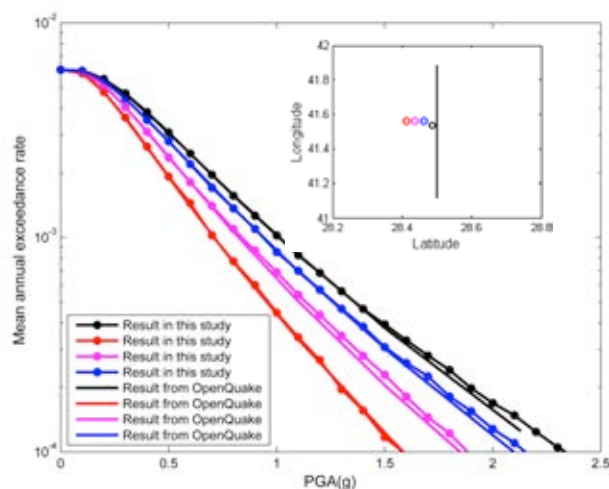
Fig. 4.10 Comparisons of OpenQuake PGA hazard curves with those computed from in-house Matlab^{TM} codes developed for running MC-based MSRFs technique. The site conditions are characterized by V_{S30} = 720m/s
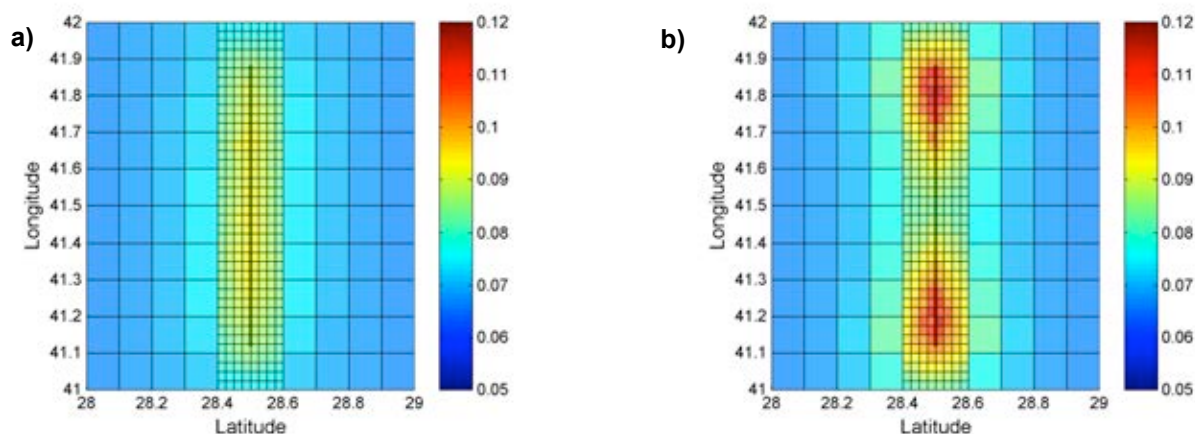
Fig. 4.11 Distribution of S_a(3s) amplitudes for 475-year return period a) without and b) with near-fault directivity effects. The fault segment is shown as a dark solid line on the plots.

Fig. 4.11 shows the influence of near-fault directivity effects on the distribution of 475-year return period spectral acceleration at T = 3.0s [S_a(3s)]. Fig. 4.11a displays the distribution of S_a(3s) when the near-fault directivity effects are disregarded in the hazard assessment. The spectral amplitude distribution follows a uniform pattern attaining its maximum in the vicinity

of entire fault length and decreases gradually towards distant sites from the fault. The spectral amplitude distribution in Fig. 4.11b considers the directivity effects for the same case. The maximum spectral amplitudes are observed at the ends of the fault segment. They are approximately 20% to 25% larger with respect to those that disregard the forward directivity. The spectral amplitudes in the middle portion of the fault segment are smaller in Fig. 4.11b when compared to the corresponding spectral values in Fig. 4.11a. These observations emphasize the importance of site location with respect to fault orientation when near-fault effects are mapped on to the hazard. The spectral amplitude comparisons between Fig. 4.11a-b suggest the insignificance of directivity effects for distances greater than 10 km from the fault segment. We note that these observations are confined to a specific source configuration and return period (i.e., 475-year return period). The influence of forward directivity on spectral amplitudes increases for larger return periods and higher seismic activity (i.e., larger slip rates).
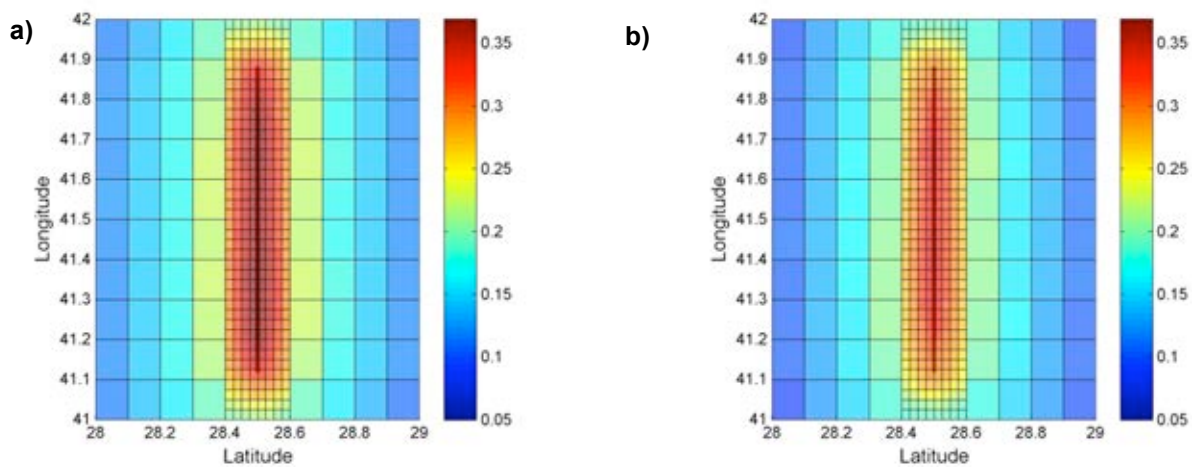
Fig. 4.12 Distribution of a) $S_a(1.0s)$ and $S_a(1.0s)|S_a(3.0s)$ for 475-year return period. The fault segment is shown as dark solid line on the plots

The left and right panels in Fig. 4.12 display the significance of conditional hazard on dynamic GMIMs and how it is accounted for by MC-based MSRFs approach. The plots show the distributions of $S_a(1.0s)$ (Fig. 4.12a) and $S_a(1.0)|S_a(3s)$ (Fig. 4.12b) for 475-year return period. The distribution of $S_a(1.0s)$ conditioned on $S_a(3.0s)$ displays 10% to 15% lower spectral amplitudes with respect to the distribution of $S_a(1.0s)$ at sites closer to the fault. Such spectral differences can be important for the design or performance assessment of high-rise buildings under the influence of higher mode effects. For example, $S_a(1.0s)|S_a(3.0s)$ distribution could be important for a tall building of 3.0s fundamental period (T_1) whose second mode (T_2 = 1.0s) has a considerable effect on its dynamic response. To this end, the approach presented in this article would yield useful information for the spatial variation of such vector GMIMs for the probabilistic risk and loss assessment of geographically distributed building inventories (e.g. Weatherill et al., 2015).

Fig. 4.13 illustrates a more sophisticated case study in which the significance of spatial correlation (SC) and near-fault forward directivity (NF) effects is discussed for three spectral periods at three different locations relative to the fault segment (Fig. 4.13a). We consider a pair of sites at each location for spatial correlation effects. The pairs are closely spaced at locations 2 and 3 whereas the separation distance between the sites at location 1 is larger. The chosen spectral ordinates represent very short-period (PGA-T = 0.0s; Fig. 4.13b), intermediate-period (T = 0.5s; Fig. 4.13c) and long-period (T = 3.0s; Fig. 4.13d) ground-motion demands. The comparative plots in Fig. 4.13 suggest that consideration of spatial

correlation has negligible influence at location 1 due to large separation distance between the sites. This observation particularly holds for very short period (Fig. 4.13b) and intermediate period (Fig. 4.13c) spectral ordinates. For longer periods (Fig. 4.13d), disregarding SC effects at location 1 yields slightly lower spectral amplitudes with respect to the case when this effect is considered. We note that the NF effects are insignificant for PGA as well as for $S_a(0.5s)$ at all sites because they become effective after $T = 0.6s$ in the Shahi and Baker (2011) model. Disregarding spatial correlation has more pronounced effects for the 2nd and 3rd locations as the sites are closely spaced at these locations. Seismic hazard assessment that overlooks SC always underestimates spectral amplitudes that increases with increasing annual exceedance rate and spectral period. The consideration of NF effects has different implications for the three locations considered for periods shifting to longer spectral period bands (Fig. 4.13c). The NF effects are immaterial at the first location as it is far from the fault segment (~ 25 km). Consideration of NF effects amplifies $S_a(3.0s)$ at location 3 and de-amplifies it at location 2. As discussed in Fig. 4.11, the near-fault forward directivity effects are pronounced at the ends of the fault segments (e.g. location 3) and become minimum at the mid segment of the fault (e.g. location 2).
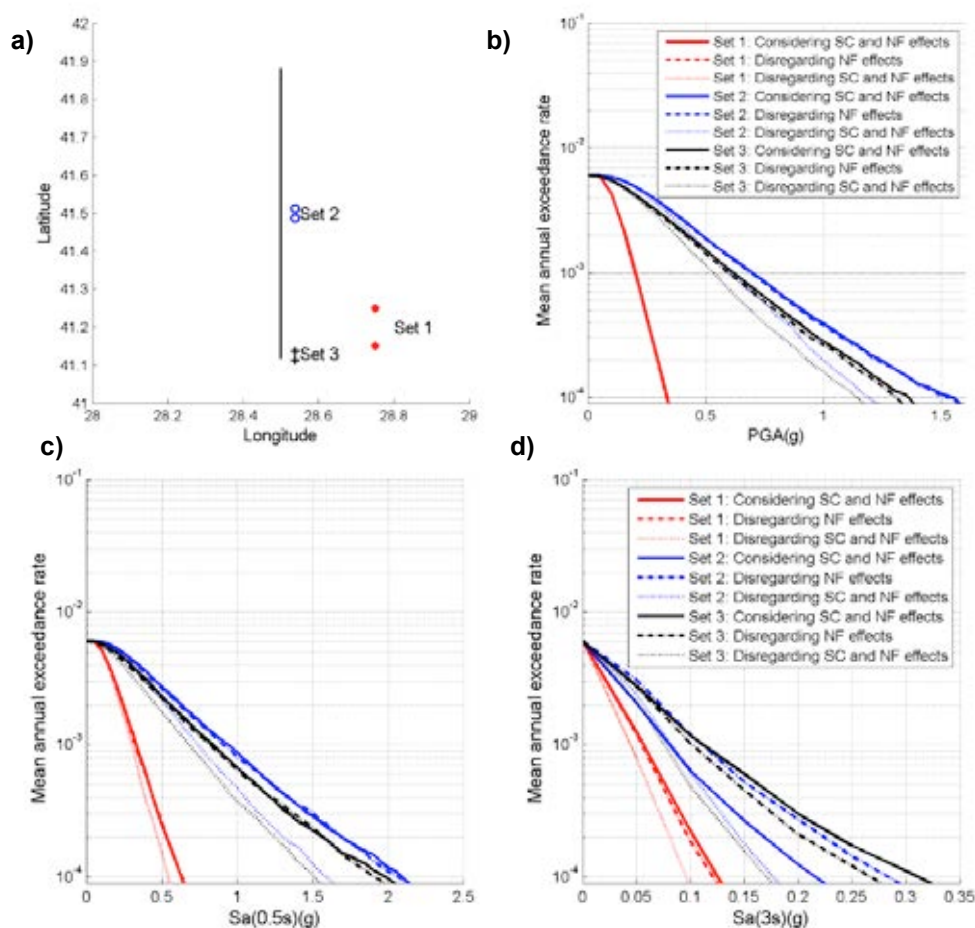
Fig. 4.13 Effect of spatial correlation (SC) and near-fault forward directivity (NF) effects at three different locations for three spectral periods a) Plan-view of locations, sites and the fault segment, b) joint hazard curves for PGA, c) joint hazard curves for $S_a(0.5s)$, and d) joint hazard curves for $S_a(3s)$.

4.2.3.2 Case studies concerning permanent fault displacement

We duplicated the case study in Petersen et al. (2011) to validate our codes that are developed for MC-based probabilistic fault displacement hazard assessment. The case study in Petersen et al. (2011) assumes a strike-slip fault with a characteristic magnitude of M_w 7 occurring, on average, every 140 years. The authors assume nonzero permanent fault displacement whenever there is a surface rupture on the fault (i.e., $P(D \neq 0|_{z,\,sr \neq 0}) = 1$). They also adopt accurately mapped fault trace scenario in their example. We used the same assumptions and ran the probabilistic fault displacement hazard by generating 40,000 simulations with a catalog period of 100-year. We considered a stripe of 150m from each side of the fault segment and computed the variation of permanent ground displacement along the entire fault length at every 100m. The sizes of cells on each side of the fault segment are taken as 25m × 25m. The variation of permanent fault displacement is computed at every 1m within the 150m-stripe. Fig. 4.14a shows the distribution of permanent fault displacement along the fault trace for a 475-year return period. The permanent fault displacements are maximum on the ruptured fault trace and attenuates very rapidly as one moves away from the fault in the perpendicular direction. Fig. 4.14b compares the MC-based probabilistic permanent on-fault displacement at the center of the fault with the results of Petersen et al. (2011). The variation in the displacement profile is given along the 150m stripe from each side of the fault. Our MC-based probabilistic approach yields very similar permanent displacements to those of Petersen et al. (2011).
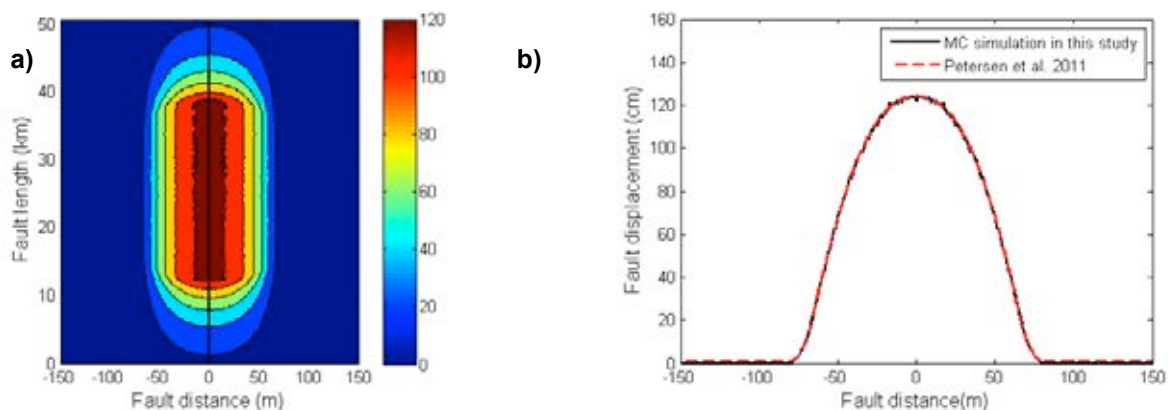
Fig. 4.14 Validation of MC-based probabilistic permanent fault displacement method by using the case study in Petersen et al. (2011): a) distribution of 475-year permanent fault displacement along the fault strike, b) comparison of computed 475-year on-fault displacement at the center of the fault with Petersen et al. (2011).

The next case discusses how the location uncertainty in pipe crossings along the fault affect the design and performance assessment of continuous pipelines subjected to permanent fault displacement. The axial strains (tensile or compression) developed in the pipeline due to fault rupture emerging at the surface result in various failure modes (e.g. pipe rupture or buckling) at the segments crossing the fault. The nature and level of stress concentrations at such critical pipe segments depend on the pipeline orientation, location of pipe crossing along the fault segment and the dominant component of fault displacement (normal, reverse, left-lateral or right-lateral slip). Fig. 4.15a shows a pipeline-fault (strike-slip) configuration: α is the pipe crossing angle and pipe crossing location is designated by x measured from the left end of the representative configuration. The annual exceedance rates corresponding to the permanent fault displacements of 70cm and 250cm are computed for $0 \leq x \leq L$ after

running 40,000 MC simulations for a 100-year catalog period (i.e., 4,000,000 years of total catalog duration). The imposed permanent ground displacements grossly represent tensile strains developed on the butt-welded continuous pipelines for onset of yielding (70cm) and 10% probability of tensile rupture (250cm) when pipeline orientation is perpendicular to the fault (i.e., α = 90°). The former performance level represents the normal operability (pipeline serviceability under frequent events) whereas the later displacement limit is used for pressure integrity: an important condition to be satisfied under design level ground motions. The mean annual exceedance rates as a function of pipe crossing location (i.e., *x*) along the fault segment are given in Fig. 4.15b for a fictitious fault rupturing with characteristic magnitudes between M_w 7 and M_w 7.5 with an average slip rate of 20 mm/year. Fig. 4.15b depicts the sensitivity of annual exceedance rates to the location of pipe crossing. Given any one of the performance levels, the mean annual exceedance rates are very low for pipe crossing locations close to the ends of the fault segment. The exceedance rates are significantly high towards the center of the fault segment. In essence, the permanent fault displacements for the designated pipe performance levels will be the result of very rare events (low consequence) for continuous pipelines crossing at locations close to the edges of the fault segment. The same plots suggest that relatively more frequent earthquakes should be of concern for performance evaluation of continuous pipelines when their fault crossings are more likely to occur at the middle portion of the fault segments. Currently, the seismic design of continuous pipelines is based on fixed mean annual exceedance rates (e.g. IITK-GSDMA, 2007; ALA, 2005; ASCE. 1984; O'Rourke and Liu, 2012; JSCE, 2000; CEN, 2006]). Our simple case study suggests that this approach would yield non-uniform risk and loss assessment for their performance verification.
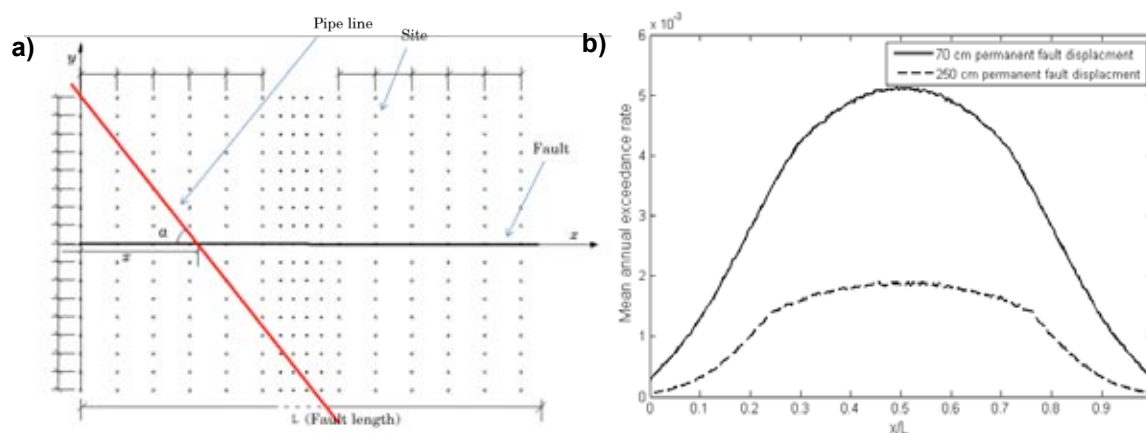
Fig. 4.15 a) Fault, pipeline and site lay out: *x* denotes the pipe crossing location along the fault, *α* is the crossing angle between the pipeline and fault, *L* is the fault length; b) Mean annual exceedance rates as a function of pipe crossing location for permanent ground displacement of 70cm and 250cm. (α = 90° in the given example)

4.2.4 Conclusions

We present the implementation of MC-based simulation techniques for PSHA of dynamic GMIMs and permanent fault displacement. The MC-based simulations are incorporated with multi-scale random fields (MSRFs) approach to account for the spatial correlation, near-fault forward directivity and conditional hazard (cross-correlation) in the variation of dynamic intensity measures. The multi-scale random fields provide flexibility for instant modification of intra-event aleatory variability whenever it is necessary (e.g. near-fault forward directivity effect). Our probabilistic permanent fault displacement method considers the uncertainty in

the location of the fault segment. Consideration of all these factors via conventional (integral) PSHA can be computationally a challenging task.

The theoretical aspects presented herein are validated by a limited number of case studies. These exercises suggest the reliability of our MC-based probabilistic hazard results when compared to their counterparts obtained from conventional PSHA. Other case studies showing the influence of near-fault directivity, spatial correlation and conditional hazard advocate that each one of these complexities can effectively modify the hazard upon their deliberate implementation. We also show that the location of pipeline crossings along the fault length may affect the decisions on the probabilistic risk assessment of continuous pipelines. In essence the MC-based techniques discussed in the chapter provide flexibility to observe the effects of such specific features on hazard without running complicated probabilistic hazard integrals.

5 Vulnerability models

5.1 VULNERABILITY ASSESSMENT METHODS

Vulnerability is defined as the extent to which an element at risk can withstand the impact of the hazard comprises a key element for effective risk assessment. The concept of vulnerability may change according to the element at risk that is taken into consideration to estimate exposure. For example, the vulnerability of the economic system will be different and measured differently from that of the building stock. Vulnerabilities of the elements at risk may change over time, during the disaster cycle, and also if faced with multiple coinciding events (time dependency issues).

The evaluation of vulnerability is generally made through the computation of fragility and/or vulnerability functions enabling to assess the distribution of the expected damage in each typology of buildings or infrastructures for each expected phenomenon. They should be estimated both for single adverse events and for cascades of adverse events.

While the evaluation of the seismic vulnerability has received over the past years a significant attention (e.g. Calvi et al., 2006; Pitilakis et al., 2014a), the vulnerability assessment of structures related to other hazards (e.g. tsunamis, floods, landslides etc.) is still limited (e.g. Fotopoulou and Pitilakis, 2013). Therefore there is a clear need to expand the vulnerability and risk assessment methods developed for seismic hazard to other hazards. In addition while work has been done considering individual hazards, there has been very limited work towards a uniform vulnerability model of infrastructures considering multiple hazards as well as interactions between them.

In the seismic case, vulnerability functions describe the probability of losses (such as social or economic losses) given a level of ground shaking. They relate the level of ground shaking with the mean damage ratio (e.g. ratio of cost of repair to cost of replacement). Fragility functions provide the probability of exceeding different limit states (such as physical damage or injury levels) given a level of ground shaking. They relate the seismic intensity to the probability of reaching or exceeding a level of damage (e.g. minor, moderate, extensive, collapse) for the elements at risk. The number of damage states and the type of intensity measure vary depending on the method and the element at risk. They are often described by two-parameter lognormal probability distribution functions. Vulnerability functions can be derived from fragility functions using consequence functions, which describe the probability of loss, conditional on the damage state.

Several approaches are used to establish fragility functions stemming principally from the significant advances in earthquake engineering. They are grouped into four general categories: empirical, judgmental or expert elicitation, analytical and hybrid (e.g. Pitilakis et al., 2014a).

Empirical fragility curves are based on post-event surveys and observations of actual damage. They are specific to particular sites and seismotectonic, geological and geotechnical conditions, as well as the properties of the damaged structures. Consequently, there are limitations in their general application because the curves are derived for a specific seismic region and a sample that is not necessarily similar to that sought. Rossetto et al. (2013) provided an extensive review of the state-of-art in the construction of empirical fragility functions for buildings while Shinozuka et al. (2003) presented methods of empirical fragility curve development for bridges.

Expert judgment fragility curves are developed based on expert opinion. Therefore, they are versatile and relatively fast to establish, but their reliability is questionable because of their

dependence on the experiences of the experts consulted. Expert opinion is used by most rehabilitation codes in the United States of America (ATC, 1985; ATC, 1991) while a recent effort to revive the judgment-based methods has been carried out within the Global Earthquake Model (www.globalquakemodel.org).

Analytical fragility curves adopt damage distributions simulated from the analyses of structural models under increasing earthquake loads. In general they result in a reduced bias and increased reliability of the vulnerability estimates for different structures compared to expert opinion and thus they are becoming ever more attractive in terms of the ease and efficiency by which data can be generated. On the other hand, their application is limited to the specific type of structure analyzed, while the analysis itself is most of the time data-demanding and time-consuming, thus designated only for special or very important structures.

Hybrid fragility curves combine any of the above-mentioned techniques in order to compensate for their respective drawbacks.

It is noted that with the above functions only the potential physical damages of the components of the systems are considered, with no consideration of functionality of either the elements or the whole system. To assess the vulnerability at system level, except for the previously described methods, different complementary approaches should be followed (Pitilakis et al., 2014b), i.e. a connectivity analysis, a capacity analysis or a fault-tree analysis. A short description of these methods is provided in Chapter 6.

In the framework of D4.2 of STREST a comprehensive review of fragility functions for most important components of the selected geographically distributed CIs (CI-B1: Major hydrocarbon pipelines, Turkey, CI-B2: Gasunie national gas storage and distribution network, Holland, CI-B3: Port infrastructures of Thessaloniki, Greece) is carried out. New fragility curves are developed where necessary, considering the distinctive features of the selected CIs (e.g. STREST Deliverable D4.1; Salzano et al., 2015).

5.2 REVIEW OF FRAGILITY CURVES FOR MAJOR HYDROCARBON PIPELINES (CI-B1)

Buried pipeline systems are commonly used to transport water, sewage, oil natural gas and other materials. They are considered as lifelines since they carry materials essential to the support of human life.

Buried pipes are classified as segmented and continuous. Segmented pipes are commonly used in water and sewage networks. Typically, they consist of rigid pipe segments and flexible joints with bell-spigot and rubber gasket type of connections. Damage in segmented pipes happens at joints in the forms of pullout or joint crushing. On other hand continuous pipes usually consist of steel pipes with welded connections. They are widely used in major hydrocarbon or water transmission lines to transport oil, gas and water from the sources to the end points. In contrast to segmented pipes the joint stiffness in continuous pipes is not much different than the rest of the pipe segment. Typical damage is in the form of local buckling due to beam bending (in normal burial depths) and global (beam) buckling (in shallow burial depths) or in submarine pipelines.

5.2.1 Fragility expressions for buried pipes

Seismic fragility relations for buried pipe are particularly useful for estimating the likely amount of pipe damage in future events. The potential damages of pipelines can be

assessed by fragility curves, which relate the pipeline damage rates to different level of seismic intensity. Pipelines suffer damage during earthquakes generally reduced by two classes of seismic hazards: the ground shaking due to wave propagation (WP) and permanent ground deformation (PGD) due to ground failure (O'Rourke and Liu, 1999). WP damage is effective in large areas but the damage rates are low. Whereas PGD damage is effective in localised areas but damage rates are high as compared to WP. Up to this point most of the damage is available for segmented pipes. However, such relations have been empirical, typically a regression line through data points from observation. As such, they are not particularly useful in estimating damage to pipe materials, pipe diameters or pipe joints that differ significantly from the pipe characteristics in the observational data set. This is unfortunate since the observational data set corresponds primarily small to moderate pipe diameters while larger diameter pipes and other hazard types (fault crossing) of greater interest.

In some current relations, both wave propagation (WP) and Permanent Ground Deformations (PGD) can be included simultaneously. The damage rates of buried pipes are often defined as the number of pipe repairs (RR) per unit length of pipeline, while the seismic intensity is quantified via a series of ground motion parameters calculated with seismic records. Therefore, some ground motions parameters representing the strong ground shaking, such as PGA, PGV, spectral intensity (SI), maximum ground strain, and composite parameters PGV^2/PGA, are used to define pipeline fragility curves describing the damage of pipelines due to transient deformation of the soil induced by wave propagation (WP). On the other hand, active fault displacement, lateral spread and seismic settlement due to liquefaction, and earthquake-induced landslide, are applied for the pipeline fragility curves for assessing the pipeline damage induced by permanent ground deformation (PGD) of the surrounding soil during earthquakes.

Continuous pipelines usually consist of welded-joint continuous steel pipes. Such high quality are not much sensitive to WP hazard as the induced strains due to wave passage is very low as compared to the PGD hazard. Eguchi (1983, 1991) concluded that the repair rate of X grade steel pipes with arc-welded joints was approximately 100 times smaller than the worst performing pipes studied. The fragility relation for welded-joint continuous steel pipeline are few and described with Equation (5.1), in which the values for the parameters in the literatures are listed in Table 5.1.

$$RR\text{(repair number/km)} = a \cdot \text{IM}^b \tag{5.1}$$

It should be noticed that although studies, e.g. listed in Table 5.1, provide empirical fragility relations for steel welded joints continuous pipelines developed from the collected data of their damages during the past earthquakes, the evaluation of seismic performance of pipelines induced by active fault displacements is not suitable to these fragility relations.

Table 5.1 Empirical pipelines fragility relation based on Eq. (5.1); *D* is diameter of the pipelines; *a* and *b* are variables in Eq. (5.1); prob [liq] is probability of liquefaction.

IM	*a*	*b*	Reference
PGV	$0.83 \cdot 10^{-4}$ (small D) $0.25 \cdot 10^{-4}$ (large D)	1.98	Eidinger, 1998
PGV	$14.5 \cdot 10^{-4}$ (small D) $3.62 \cdot 10^{-4}$ (large D)	1	ALA, 2001
PGV	$3 \cdot 10^{-5}$	2.25	O'Rourke and Ayala (1993) HAZUS (NIBS, 2004)
PGD	3.55	0.53	Eidinger and Avila, 1999
PGD	1.68	0.32	ALA, 2001
PGD	0.3 Prob [liq]	0.56	Honegger and Eguchi, 1992 HAZUS (NIBS, 2004)

5.2.1.1 *Fragility expressions for large diameter continuous pipes at abrupt lateral fault offsets*

Permanent ground deformation (PGD) is a significant hazard for water, gas, oil and sewer pipelines. The principal forms of PGD are surface faulting, landsliding, seismic settlement and lateral spreading due to soil liquefaction. PGD frequently involves differential ground movement wherein two sides move either horizontally or vertically with respect to each other, across a slip or fault. Fault crossing is considered as abrupt lateral PGD hazard in which the displacement field changes immediately within the fault surface and remains constant outside the fault line. As a result of fault offsets axial strains are induced in pipes. The amount of strain depends on the orientation of the pipe with to the fault line (crossing angle), slip direction as well as on the soil and pipe properties.

Whether the differential ground movement results in a pipe primarily in tension or compression depends on the relative orientation of the fault and the pipe as well as the direction of faulting. For example, right lateral strike slip faulting with a negative intersection angle (which is measured with the pipe moving clockwise around the pipe-fault intersection point toward faulting direction; the angle is larger than -90°) results in axial tension and bending in the pipe. However, left lateral strike slip with a positive crossing angle (which is measured with the pipe moving anticlockwise around the pipe-fault intersection point toward faulting direction; the angle is less than 90°) results in axial compression and bending.

When suffering the fault displacement, the pipeline behaviour is significantly influenced by many factors which these fragility relations do not account for, such as pipeline-fault intersection angles, pipeline surround soil properties, pipeline buried depth, and etc. However, these factors at fault crossings are relatively known by engineering, although their uncertainties, to some extent, still exist. Therefore in order to access the seismic performance of buried hydrocarbon pipelines due to fault offset, the numerical analysis and the development of new fragility relations are necessary (see also STREST Deliverable D4.1, Salzano et al. 2015).

Pipe response to transverse fault offsets is a complex problem. The pipe as well as the surrounding soil needs to be modelled considering the nonlinearities in soil and pipe (Uckan et al. 2015). The response of the pipe (pipe axial strain) to ground displacement is calculated. In small offsets both axial and bending strains are important and both increase with fault offsets. Bending strains are large enough that there are nonzero net compressive in intermediate offsets, the axial strain is beyond yield, the bending strains are decreasing and net compressive strains approach zero. In large offsets, the bending strain remains constant while axial strains increase with fault offsets.

5.3 REVIEW OF FRAGILITY CURVES FOR GASUNIE NATIONAL GAS STORAGE AND DISTRIBUTION NETWORK (CI-B2)

A recent overview with respect to fragility functions for oil and gas networks can be found in Gehl et al., 2014. Pipelines, storage tanks as well as processing stations are reviewed and put in a European context.

5.3.1 Pipelines

For the pipelines, empirical based fragility functions are discusses in Gehl et al., 2014, leading to a selection that is consistent with the ones cited in Table 5.1. Refinements are possible by introducing corrective parameters K on the backbone curve eq. (5.1), depicting higher respectively lower fragilities as a function of the material, the connection type, the soil type and the pipe diameter. Based on datasets used, a preference is expressed for the expressions of ALA 2001.

For the Groningen gas field, with man induced earthquake hazards, the specific mechanism of soil liquefaction and corresponding lateral displacements is to be investigated as this is identified as one of the main failure mechanisms for the pipelines.

With scarce data obtainable for these conditions, it is decided to perform model calculations in order to obtain dedicated fragility functions. The procedure is described in Miraglia et al., 2015 and is summarised in the following.

The Dutch Metereological Institute (Dost et al. 2013), performed the data analysis and a Probabilistic Seismic Hazard Analysis (PSHA) with all data available until 2013. The Ground Motion Prediction Equation (GMPE) used for the prediction of the ground motion characteristics (peak ground acceleration and peak ground velocity), as function of the magnitude Mw and source-site distance R, is the GMPE of Akkar et al. (2013) recently derived on a large dataset that includes shallow and low magnitude events and a correction factor to take into account the faults typology and amplification for local seismic response in soft soil that makes it more suitable for the typology of the events in the Groningen area.

The general expression of the GMPE of Akkar et al. (2013) is shown in eq. (5.2), while reference is made to Dost et al. (2013) for the specific expressions and the coefficients to be used. In eq. (5.2), the ground motion characteristics X (peak ground acceleration or peak ground velocity) is a function of the ground motion parameter X_{ref} at bedrock (that depends on magnitude, fault geometry and source-site distance), of the parameter S function of velocity of propagation of shear waves at the considered site, of σ, the standard deviation of the lognormal distribution of X and ε a standard normal error. The standard normal error

between peak ground acceleration and peak ground velocity is herein considered strongly correlated.

$$\ln X = \ln\left(X_{ref}\right) + \ln(S) + \epsilon\sigma \tag{5.2}$$

Generally, the behaviour of a pipeline segment during an earthquake event, depends on the earthquake intensity and on the material and geometry characteristics of the pipe but also on pipe placement technique and soil property of the more superficial layers.

Buried pipelines are subject to deformations due to the effect of the shear waves (s-waves) generating mainly horizontal oscillation with a certain period and amplitude. The soil deformation is transferred to the pipe to a degree that depends on the soil-pipe interaction and interface. However, the dynamic effect of the s-waves is not so severe for a large pipe section of high steel grade, while more severe effects can be generated by permanent ground deformations due to soil liquefaction.

The term "liquefaction" indicates a phenomenon for which a saturated and zero cohesion soil loses its shear resistance due to the accumulation of plastic deformations caused by transient and cyclic force actions in un-drained conditions. Indeed, the development of excess pore water -pressure reduces the effect of in situ confinement of the soil. Sand boils, cracks and lateral spread phenomena are a sign of liquefaction. When liquefaction occurs the strength of the soil has nearly vanished.

Liquefaction is a phenomenon that arises only when a seismic event has an intensity that can induce such deformations in the soil that can generate a significant increase of the neutral pressure and when the soil shows significant degradation of resistance properties under cyclic load. Therefore, liquefaction occurs only for earthquake events of certain magnitude and durations. In addition, it can occur only in saturated non-cohesive soils (sand), with low plasticity index and low relative density.

The most used approach to evaluate if a soil at a certain location can show liquefaction due to seismic shake was developed in 1971 by Seed and Idriss (see Idriss et al. 2008). This simplified method is of semi-empirical nature and was developed on the basis of the comparison between mechanical properties of the soil and the occurrence of the liquefaction event. The mechanical properties of the soil are evaluated by means of in-situ tests. The effect of the earthquake is modelled through the expected maximum acceleration at the ground-level with a certain probability of exceedance for a certain return period. The acceleration needs to be multiplied by the importance factor of the structure to obtain the design value of the peak acceleration.

The method is based on the comparison between the effect of the seismic shake, expressed as Cyclic Stress Ratio (CSR), and the capacity of the soil given by the Cyclic Resistance Ratio (CRR). Both can be derived from graphical abacuses or computed with semi-empirical equations (e.g. see Fig. 5.1).
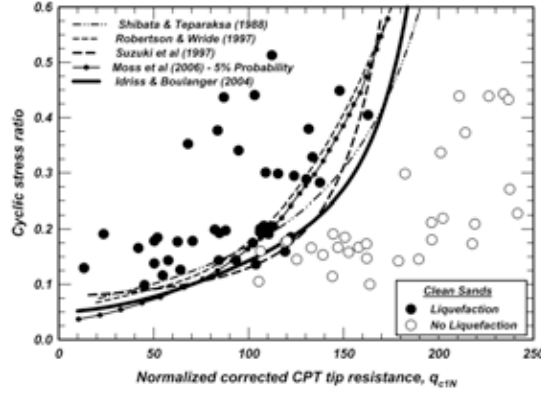
Fig. 5.1 Abacus for CSR vs normalized CPT resistance from Idriss-Boulangier (2008).

The cyclic stress ratio at the depth z_i is computed according to the expression in eq. (5.3):

$$CSR = 0.65 \frac{a_{max}}{g} \frac{\sigma_v}{\sigma'_v} r_d \frac{1}{MSF} \tag{5.3}$$

Where a_{max} is the peak acceleration at ground level, g is the gravity acceleration, σ_v and σ'_v are respectively the total static vertical stress and the effective vertical stress at depth z_i, 0.65 is a reduction for the irregularity of the seismic record. The factor r_d is a reduction factor that takes into account the reduction of the effect of the seismic shake with the depth of the layer and deformability of the soil and is a function of both depth and (moment) magnitude of the seismic event. The semi-empirical expression for r_d is given in Eq.(5.4).

$$r_d = \exp\left[\left(-1.012 - 1.126\sin\left(\frac{z}{11.73} + 5.133\right)\right) + \left(0.106 + 0.118\sin\left(\frac{z}{11.73} + 5.142\right)\right)M\right] \tag{5.4}$$

The factor MSF is a Magnitude Scaling Factor that corrects the CSR value for events of moment magnitude different from M=7.5. Indeed, the expression of CSR was derived on a dataset collecting events of magnitude between 5.9 and 8.3. A correction was applied to get an equivalent value for Mw=7.5. The expression for MSF is in Eq.(5.5).

$$MSF = \begin{cases} 6.9 \exp\left[\frac{-M}{4}\right] - 0.058 \\ MSF \leq 1.8 \end{cases} \tag{5.5}$$

The evaluation of the resistance of the soil in the method of Seed-Idriss is based on in-situ tests such as SPT (standard penetration test) and CPT (cone penetration test) and the measure of the propagation velocity of shear waves Vs.

In this paper the results of CPT tests will be considered, in which case the Cyclic Resistance Ratio is given in Eq.(5.6).

$$CRR = K_\alpha K_\sigma CRR_{\alpha=0,\sigma=1} \tag{5.6}$$

Where $CRR_{\alpha=0,\sigma=0}$ is the value of CRR for low stress state and horizontal ground level and a reference stress of 100kPa (1bar) (see Eq.(6)), $K\alpha$ is the correction coefficient for the slope of the ground and $K\sigma$ is the correction coefficient for the stress state.

$$CRR_{\alpha=0,\sigma=1} = \exp\left[\frac{q_{c1,n}}{540} + \left(\frac{q_{c1,n}}{67}\right)^2 - \left(\frac{q_{c1,n}}{80}\right)^3 + \left(\frac{q_{c1,n}}{114}\right)^4 - 3\right] \tag{5.7}$$

Since $\alpha = \tau_{st}/\sigma'_v$, i.e. equal to the ratio between tangential stress and vertical effective stress, $K\alpha$ is defined by an exponential expression function of the relative density, angle α and quality of the sand (quarz, feldspar, chalk etc.) with coefficients having a polynomial expression. These equations are taken from Idriss et al. (2008). The correction factor K_σ is a function of the effective stresses σ'_v and of the normalized CPT resistance $q_{c1,n}$.

5.3.1.1 Permanent displacement

The quantification of the displacements during liquefaction is a complex problem. However, the largest displacement will occur due to floatation of the pipeline in the liquefied sand and due to lateral spread in post-liquefaction condition, i.e. the lateral displacement of e.g. gently sloping ground as the result of the liquefaction. The horizontal level ground displacement can be computed by numerically integrating the expected shear strains along the depth of the soil layers. To perform a one-dimensional integration on the volumetric strain is of course a simplified approach. However, it is a general approach that has been extensively used in research and practice. Usually the integration over the depth is applied on the maximum shear strain given the linear dependency of maximum displacement on the shear strain (maximum potential displacement). Actual lateral displacements will depend on several other factors (ground slope, heterogeneity, etc.).

The simplified method developed by Seed (Idriss et al. 2008) relates the maximum shear strain to the safety factor against liquefaction defined as ratio between CRR and CSR. The expression of the maximum shear strain in Eq.(5.8) is also of semi-empirical nature and it is applicable in a limited range of Dr and CPT resistance ($D_r \geq 0.4$ and $q_{c1,n} \geq 69$).

$$\gamma_{max} = \begin{cases} 0, if\ FS \geq 2\ (\ no\ liquefaction\ ) \\ min\left(\gamma_{lim}, 0.035(2 - FS)\left(\frac{1-F_\alpha}{FS-F_\alpha}\right)\right), 2 > FS > F_\alpha \\ \gamma_{lim}, FS \leq F_\alpha \end{cases} \tag{5.8}$$

Where F_α and γ_{lim} can be computed as function of D_r or q_{cpt},n (see Idriss et al. 2008).

The maximum potential displacement during liquefaction is computed with a one-dimensional integration of γ_{max} along the depth. Herein, the computed displacement is then applied to the pipeline segment, together with an uplift buoyancy effect. It is also assumed that the liquefaction involves the pipe for a length equal to 10 times the external diameter.

5.3.1.2 Springs Interaction model

The pipeline shown as an example is considered as installed on the bottom of a trench at the depth of 2.3 m (pipe diameter 1219 mm). The interaction with soil sub layers is modelled by a set of nonlinear springs along the pipe (the segment length considered is 20 times the external diameter). The pipe is therefore constrained by springs on the top, the lateral sides and at the bottom (Helmholt et al. 2013). They differ from each other and depend on the soil properties of sub layers and top layer of soil (Fig. 5.2). Their properties are defined as depending on the passive, neutral and reduced vertical stresses of the soil, the vertical coefficient of subgrade reaction, and the ultimate bearing capacity of the soil layers above and below the pipe (Fig. 5.2 and Fig. 5.3).
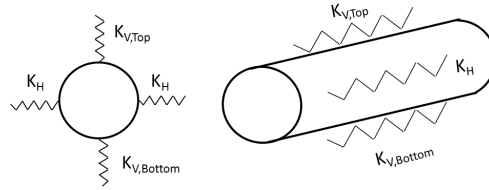
Fig. 5.2 Springs along the pipe.
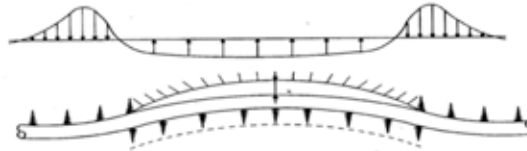
Fig. 5.3 Longitudinal view of pipeline displacements.

The stresses in the soil and its bearing capacity are related to the mechanical properties of the soil (saturated and effective unit weight, friction angle, cohesion, Young's modulus etc.) but also from some geometrical conditions such as external diameter, installation depth, groundwater level. The soil mechanical parameters are derived for two locations in the Netherlands northern region by means of Cone Penetration Test (CPT) and Triaxial tests. The W-Tube (Helmholt et al. 2013) tool is a TNO developed solver that computes the Finite Element Solution (FEM) for a 3D continuous, segmented and even a full pipe network installed in trench on a spring bed as described in 2.2.1. Loading is applied through prescribed soil displacements as well as through buoyancy forces. Pipeline geometry and material, constraints, length of segments, springs stiffness and external action (forces or displacement patterns) are the input for the solver that can be managed from Matlab.

5.3.1.3 *Pipeline Seismic Fragility*

The fragility function expresses the probability of exceedance P_{LS} of a certain limit state Y_{LS} with respect to a certain Intensity Measure (IM). The fragility is also known as conditional probability of exceedance of the limit state LS and can be defined in Eq. (5.9), where the intensity measure is denoted with S.

$$P_{LS}(s) = p(Y_{LS} > 1|S = s) =$$

$$p\left(S_{Y_{LS}=1} \leq s\right) = \Phi\left(\frac{\ln s - \mu_{\ln S_{Y=1}}}{\sigma_{\ln S_{Y=1}}}\right) \tag{5.9}$$

The parameters of the curve are the mean $\mu_{\ln SY=1}$ and standard deviation $\sigma_{\ln SY=1}$ of the logarithm of the seismic intensity S_Y that causes the achievement of the limit state $Y_{LS}=1$. Common practice is to derive the parameters $\mu_{\ln SY=1}$ and $\sigma_{\ln SY=1}$ from observational analysis. For the situation investigated there is an absence of observations due to the non-tectonic nature of the earthquakes and, therefore, a model is needed to simulate the behaviour of the pipe segments. Monte Carlo simulations are carried out to generate the necessary data to

perform a hypothetical observational analysis to compute the seismic fragility of the specific pipeline in the north of the Netherlands. In the following, the results of the benchmark study on two segments of the high pressure pipeline (diameter 1219 mm, welded steel X60, continuous) at two different locations are presented. In deliverable D6.1 the work will be extended to the full network of high pressure pipeline with valves and operational stations.

5.3.1.4   Stochastic simulations

The GMPE of Akkar et al. (2013) as in Eq. (5.2) is used as to sample peak ground acceleration and velocity of earthquake events occurring with a magnitude uniformly distributed in the range Mw (4 ÷ 6) and with source-site distance of 3 km. The two locations are considered independent from each other.

The full characterization of the soil layers is available in two locations in the region of Groningen, (Meijers 2014). The subsoil is characterized in the first 13 m of soil by alternate layers of loose sand, peat and clay and deeper layers of sand. The saturated unit weight of the sand and peat, effective unit weight, friction angle, Young's modulus, Cone Penetration Test (CPT) resistance is provided in Meijers (2014) for each layer of the stratigraphy at two locations and those values are considered as mean values in the single layer. The stratigraphic distribution of the layers is available at steps of 50 cm. The same discretization is used in the computations to compute the static tensional state in the soil layers. To compute the stiffness of the springs, the values of the soil parameters at 2.3 m depth are used (sand). Soil properties are sampled as uncorrelated with exception of the saturated and effective unit weight of each layer. The relative density is computed as function of the CPT resistance with the Lunne-Christoffersen relation. The main random variables are listed in Table 5.2.

Table 5.2 Random Variables in the model

Random variable	Mean	c.o.v.
Magnitude $Mw \propto U(4,6)$	5	0.057
Saturated unit weight of sand $\gamma_{sat} \propto N$	Varies with stratigraphy and location	0.10
Saturated unit weight of peat $\gamma_{sat} \propto N$	Varies with stratigraphy and location	0.10
Effective unit weight of sand $\gamma_{sat} \propto N$	Varies with stratigraphy and location	0.10
Effective unit weight of peat $\gamma_{sat} \propto N$	Varies with stratigraphy and location	0.10
Young Modulus of Sand $E \propto N$	$3.8 \cdot 10^3$	0.10

Friction angle $\varphi \propto N$	Varies with stratigraphy, location and soil 20°-35°	0.10
CPT resistance $CPT \propto N$	Varies with stratigraphy and location	0.20

Within the Monte Carlo procedure, two main limit state functions are computed:

- Potential of liquefaction

$$LS1 = CRR - CSR \tag{5.10}$$

- Pipe rupture for exceeding stressed (von Mises yielding criterion) caused by soil permanent ground deformations (pgd)

$$LS2 = f_y - \sigma(pgd) \tag{5.11}$$

Pipe rupture for transient strain and ovalization are also computed, but they are considered of less importance in common practice, due to the fact that the rupture is more likely to occur due to the effect of PGD.

At each simulation, the mechanical parameters of the soil layers and an event of a certain magnitude is sampled and from Eq. (5.2) PGA and PGAV are derived. CSR and CRR are computed and the exceedance of the LS1 is verified (Eq. (5.10)). If LS1 is exceeded, the lateral soil displacement is computed by integrating γmax along the depth. The displacement, geometry of the pipe and the calculated soil spring stiffness are used as input for the W-Tube FEM solver. The W-Tube solver computes longitudinal and cross section deformations and stresses that are used to verify if the limit state LS2 is exceeded (Eq. (5.11)).

5.3.1.5 Simulation Results

The results of the simulations are treated as an artificial dataset to derive the fragility functions for the two segments of the pipe at two independent locations. Fig. 5.4 and Fig. 5.5 show the probability of soil failure due to liquefaction conditioned on the PGA value (fragility or exceedance of limit state LS1) and the expected value of lateral soil displacement at location 1 and 2. Although the probability of soil liquefaction is high, the lateral spread at location 1 is small (in the order of the cm) while a larger spread is expected at location 2. The result is consistent with expectation, since the stratigraphy at location 1 is characterized by smaller layers of sand under an upper layer of peat and clay, which is absent at location 2. However, the result is judged as too conservative in relation to the large conservativism of the scaling factor MSF for events with short duration (Meijers 2014) and to the sensitivity of γlim to the value of the geotechnical parameters (mostly soil relative density).

Nevertheless, the predicted displacements do not affect the pipeline segment with 1.219 m diameter, for which no rupture is found. Therefore, liquefaction events can be expected, but of minor intensity and with no effect on this kind of pipeline. Fig. 5.6 and Fig. 5.7 show the maximum lateral displacement of the pipe with respect to the correspondent soil lateral

spread for the locations 1 and 2: the pipe displacement is of 1 and 2 order of magnitude lower that the lateral spread at location 1 and 2 respectively.

For the transient displacements, based on the effect of the shear waves (s-waves), rupture occurred with probability of $8.5 \cdot 10^{-3}$. Again, the formulation used (traction stresses linear proportional to the PGV) is quite conservative and more detailed modelling will be done for CI-B2 in order to obtain valid fragilities.
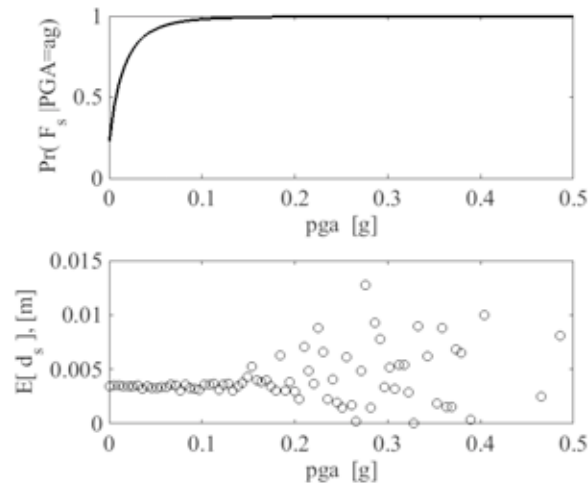
Fig. 5.4 Conditional probability of soil failure and expected simulated lateral soil displacement at location 1 with respect to PGA [g].
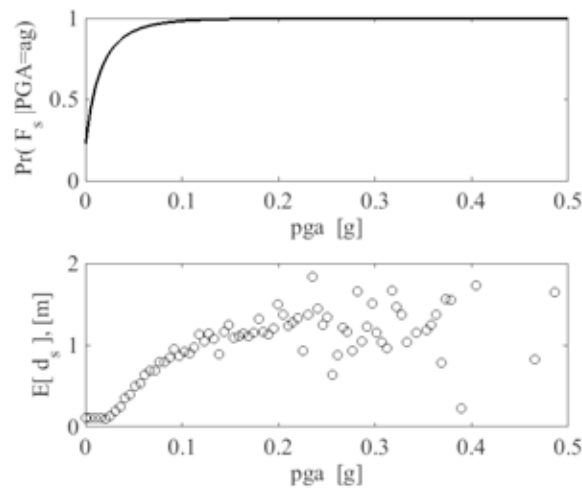
Fig. 5.5 Conditional probability of soil failure and expected simulated lateral soil displacement at location 2 with respect to PGA [g].
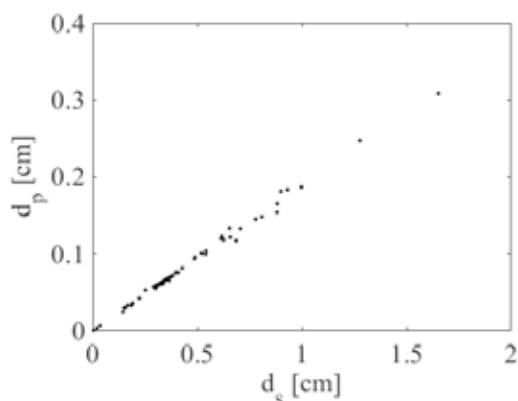
Fig. 5.6 Pipe horizontal maximum displacement with respect to lateral spread at location 1
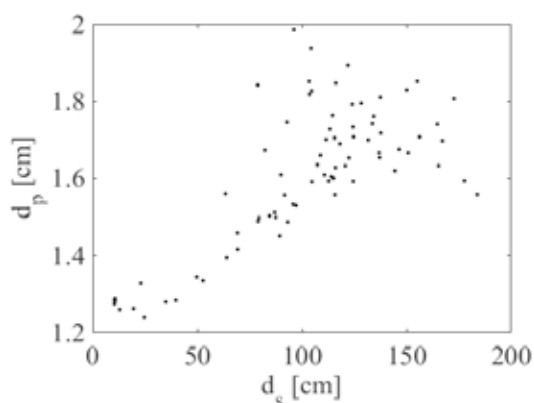
Fig. 5.7 Pipe horizontal maximum displacement with respect to lateral spread at location 2

Minor ovalization effects occur instead with high probability and with average ovalization 0.18%, largely smaller than the operational limit state of 5%.

5.3.1.6 Discussion

The limited simulation results, for the example presented, show how sand liquefaction can occur even at low values of PGA. However, the predicted lateral spread due to liquefaction causes only minor effects of deformation (ovalization) in the two pipe segments. Pipeline segment with smaller diameter and steel grade may show more severe ovalization or even some ruptures. Further modelling will be performed to completely investigate the behaviour of the pipeline network with different diameters and steel grades and with different width of the PGD. Strain based failure criteria for the pipe will be adopted, such that consistent fragility definitions are obtained with the ones presented in paragraph 5.2 for CI-B1.

5.3.2 Processing stations

Gehl et al., 2014 also review the fragility curves for processing stations. For the Groningen network some stations are open air, some are in buildings. Most buildings are relatively new and regular, either masonry or concrete. Following Gehl et al, 2014, the fault-tree procedure from SYNERG as applied for central Italy will be adopted: the cabins may be decomposed in structural components (i.e. buildings), regulators and mechanical equipment (heat

exchangers, boilers and bowls) in a fault-tree schematisation, as shown for example in Fig. 5.8. Since gas supply has to be maintained at all times, two installations can be mounted in parallel where each installation is characterized by a regulator and a monitor. The monitor is a safety device that has to be able to prevent the outlet pressure from exceeding safe thresholds in the case of complete failure of the regulator, taking over the function of the primary, normally active regulator. Besides, when boilers break down the gas flow is not ensured, since the freezing stops the system. On the other hand, reduction groups (i.e. GR) can be broken down in regulators and masonry housing (when it is present) and the corresponding fault-tree is detailed in Fig. 5.9.
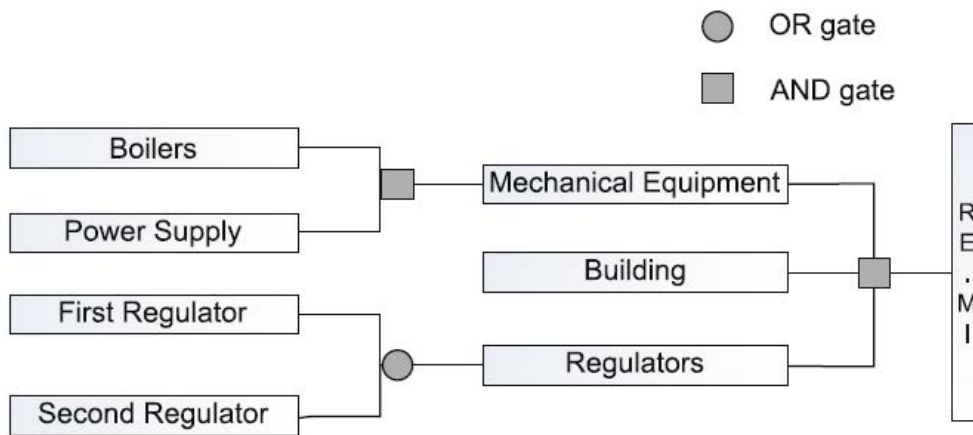
Fig. 5.8 Fault-tree decomposition of a RE.MI cabin (Esposito 2011)
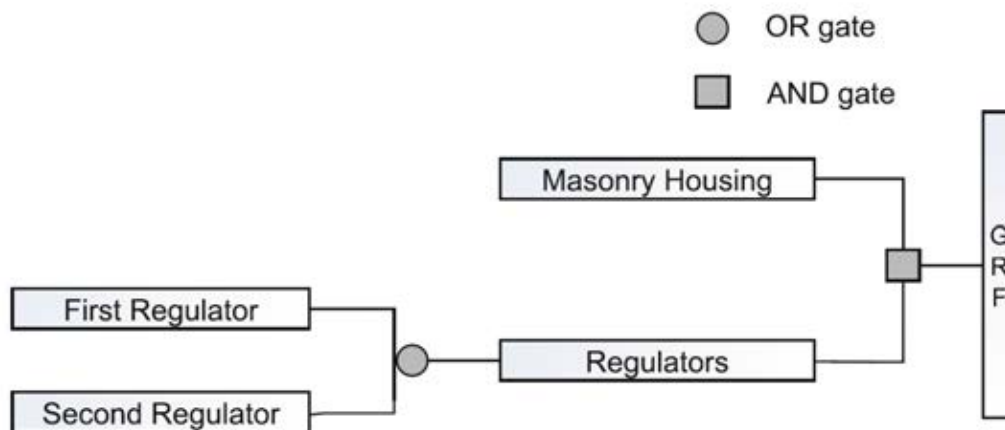
Fig. 5.9 Fault tree representation of a reduction group (Esposito 2011)

5.4 REVIEW OF FRAGILITY CURVES FOR THESSALONIKI PORT INFRASTRUCTURES (CI-B3)

A comprehensive review of existing fragility functions for the most critical components to the functionality of the port, namely waterfront structures and cranes, is provided herein. All existing fragility functions for waterfront structures and cranes were developed for the assessment of earthquake-induced damage (considering or not liquefaction). In the

framework of STREST analytical fragility curves for cranes subjected to tsunami loads have been derived as part of the Thessaloniki port case study (Deliverable D4.1, Salzano et al., 2015). Fragility functions for other components, e.g. building structures, liquid facilities etc, can be found in Pitilakis et al. (2014a).

5.4.1 Waterfront structures

Empirical lognormally distributed fragility functions for waterfront structures were proposed in HAZUS (NIBS, 2004) based on damageability of subcomponents, namely, piers, seawalls, and wharf. Fault tree logic and the lognormal best fitting technique were used in developing these fragility curves. They give the probability of reaching or exceeding certain damage states for a given level of permanent ground deformation (PGD).

Analytical methods have also been used for the seismic vulnerability assessment of waterfront structures.

Ichii (2003) and (2004) proposed several analytical fragility curves for the assessment of direct earthquake-induced damage to gravity-type quay walls using 2D dynamic finite element analysis, considering also the occurrence of liquefaction phenomena. The damage index (or engineering demand parameter) was defined in terms of the normalized seaward displacement. Fragility curves were derived in the form of log-normal probability distributions as a function of the peak basement acceleration with the aid of the maximum likelihood method. Different sets of fragility curves were suggested based on the aspect ratio of the wall, the normalized thickness of sand deposit as well as the equivalent N_{SPT} values of sand deposits below and behind the wall. The fragility curves were then used to establish relationships between the loss (in cost terms) and the excitation level.

Na and Shinozuka (2009) presented a methodology to estimate the effects of the earthquake on the performance of the operation system of a container terminal in seaports by integrating simulation models for terminal operation and fragility curves of port components in the context of seismic risk analysis. Two sets of fragility curves representing an original and a retrofitted wharf structure were presented. The authors considered PGA as ground motion intensity and used analytical approach using numerical model to construct the fragility curves. System fragility curves were developed based on fragility curves of independent wharf components.

Kakderi and Pitilakis (2010) proposed analytical fragility curves for waterfront/retaining structures for ground shaking without the occurrence of liquefaction (Fig. 5.1). Typical waterfront structures, with different geometry, foundation soil conditions and seismic excitations, were studied using appropriate finite element modeling. The corresponding damage levels were estimated with respect to the induced residual displacements and the seismic response of the soil-structure system. Fragility curves were constructed for the different types of gravity waterfront structures and foundation conditions as a function of the peak outcropping ground acceleration (PGA).
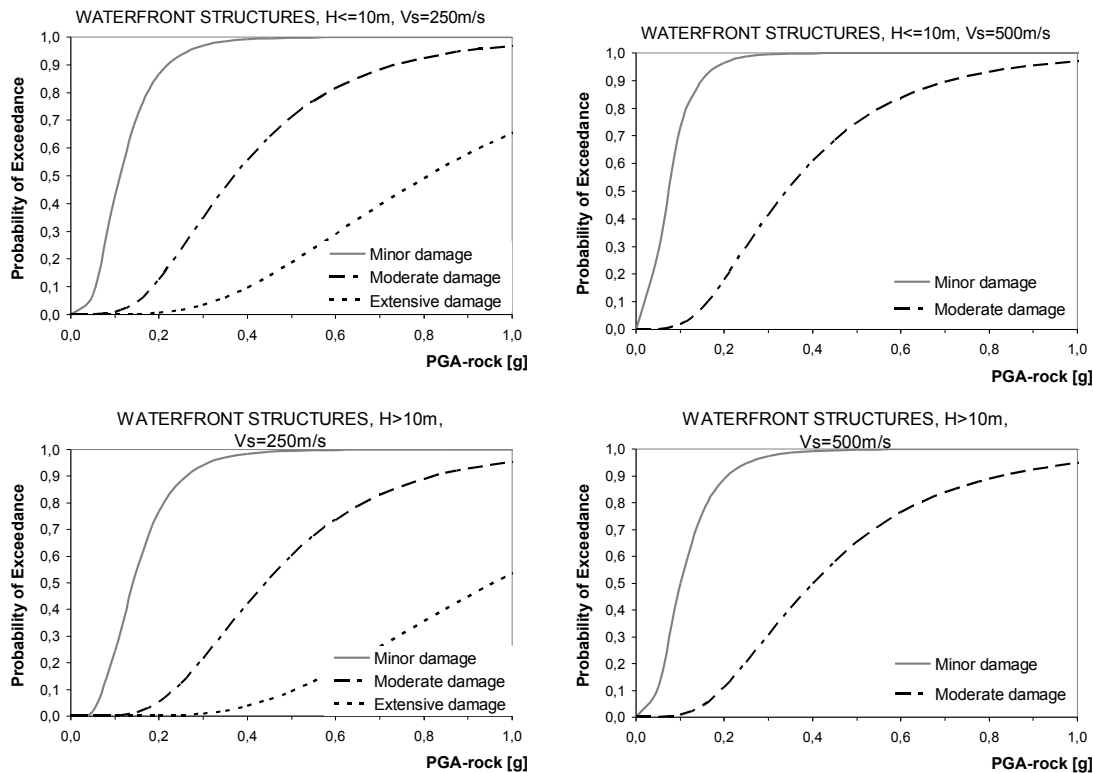
Fig.5.10 Fragility curves for waterfront structures subject to ground shaking according to Kakderi and Pitilakis (2010).

In the study performed by Ko et al. (2010), the seismic fragility analysis for the sheet pile wharves of the Hualien Harbor in Taiwan was performed using 2D nonlinear dynamic analysis. The damage index used was the maximum residual displacement at the top of the sheet pile wall subjected to different levels of peak ground acceleration (PGA) in the free field. Fragility curves were proposed in terms of two-parameter lognormal cumulative distribution functions.

Chiou et al. (2011) proposed a procedure for developing analytical fragility curves for typical pile-supported wharfs using the capacity spectrum method (CSM). The wharf deck displacement was used as wharf damage index and the peak ground acceleration (PGA) as intensity measure (IM). Fragility curves of the wharf were constructed through simple statistical analysis or, for practical applications, using shifted lognormal cumulative distribution functions.

Miraei and Jafarian (2013) developed analytical fragility curves for gravity quay walls. Dynamic 2D nonlinear dynamic analyses were carried out to capture the seismic response of such structures in terms of horizontal displacement at the top of the wall. The derived displacements were first validated with the recorded displacements of a previously conducted physical model test. The results of the numerical simulations are then statistically analyzed to derive fragility curves for the gravity quay walls. Various performance criteria including serviceable, repairable, and near collapse damages were considered to construct the fragility curves.

Torkamani et al. (2013) developed seismic fragility curves of an idealized pile-supported wharf with batter piles through a practical framework. Three engineering demand parameters (EDPs) were considered, namely the displacement ductility factor, the differential settlement between deck and behind land and the normalized residual horizontal displacement.

60

Incremental dynamic analysis (IDA) was used to estimate the seismic demand quantities. Analytical fragility curves were generated using the results of a series of 2D nonlinear dynamic analyses under multiple ground motion records. In addition, a sensitivity analysis using the first-order second-moment (FOSM) method was performed to evaluate of geotechnical parameters uncertainties in the seismic performance of the wharf.

5.4.2 Cranes/cargo handling equipment

The performance of cranes during earthquakes is critical, since crane damage and subsequent downtime has a major impact on indirect losses and post-disaster recovery of the port. In the following the generally limited contributions in seismic fragility analysis are provided.

Fragility curves describing earthquake-induced damage to cargo handling and storage components were provided in HAZUS (NIBS, 2004) based on expert judgment (Fig. 5.2). They are expressed as lognormal distribution functions and they are defined in terms of PGA and PGD to characterize damage due to ground shaking and ground failure respectively. Three damage states are defined, i.e. slight/minor, moderate and extensive/complete. A distinction is made between stationary (anchored) and rail-mounted (unanchored) cranes.

Kosbab (2010) presented an analytical method for application to seismic fragility analysis of container cranes. Nonlinear dynamic analyses were performed for the three representative container cranes, namely a large jumbo container crane (J100), an older jumbo container crane (LD100) and an older small container crane (LD50). Four limit states were defined in terms of maximum portal drift based on pushover analyses of 2D finite element model representations and engineering judgement. The first limit state was defined as derailment indicated a crane leg base movement relative to the crane rail while the other three levels of structural limit states were defined as immediate use, structural damage, and complete collapse. The spectral acceleration S_a, at the structure's fundamental mode with the structure's estimated damping level was used as IM for fragility analysis. Analytical lognormally distributed fragility curves were finally derived for the three representative container cranes based on the statistical exploitation of the results of the numerical analysis.
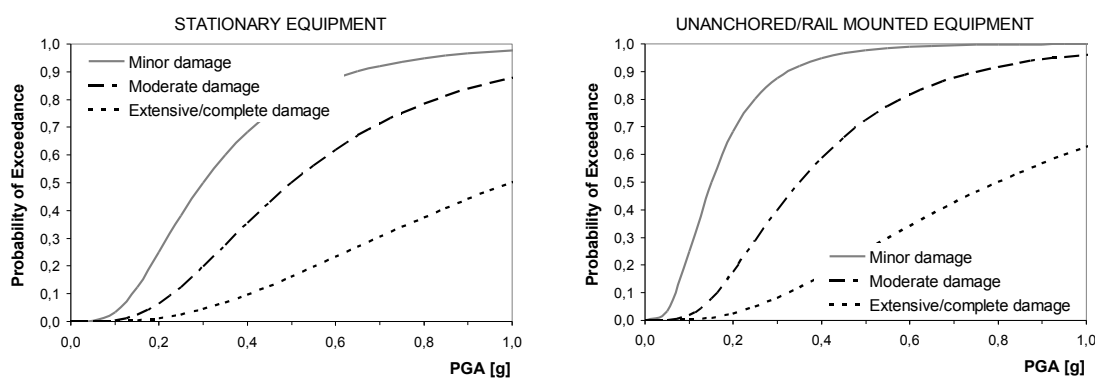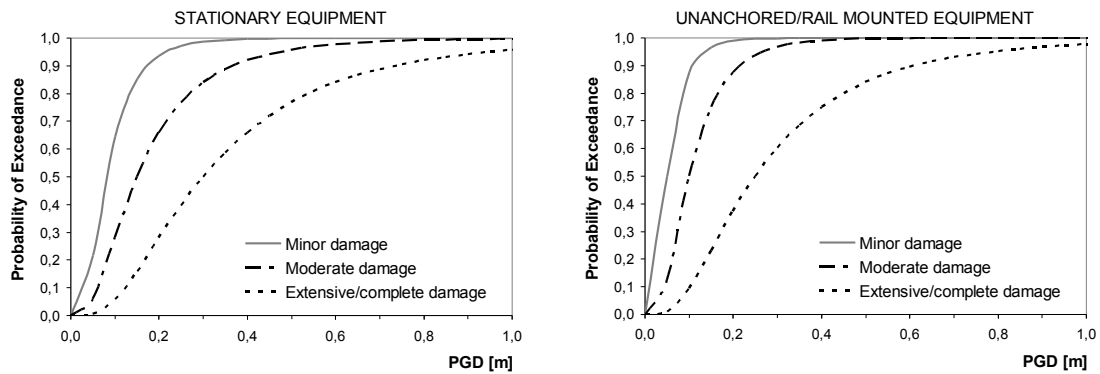
Fig.5.11 Fragility curves for cargo handling and storage components subject to ground shaking (up) and ground failure (down) according to NIBS (2004).

In the framework of D4.1 of STREST (Salzano et al., 2015), AUTH developed an analytical method to derive probabilistic fragility functions for container cranes and other critical infrastructures under tsunami forces as part of the CI-B3 case study (Port of Thessaloniki). The methodology was based on nonlinear numerical computations and adequate statistical analysis. Structural limit states were defined in terms of threshold values of material strain based on pushover analysis results. Lognornally distributed fragility curves were finally derived as a function of inundation depth (see Fig. 5.12). The new curves are exclusively proposed for tsunami (i.e. inundation depth) without considering other geotechnical hazards like the permanent ground displacements of the quay walls due to ground shaking and liquefaction. Further research is needed for these combined effects.
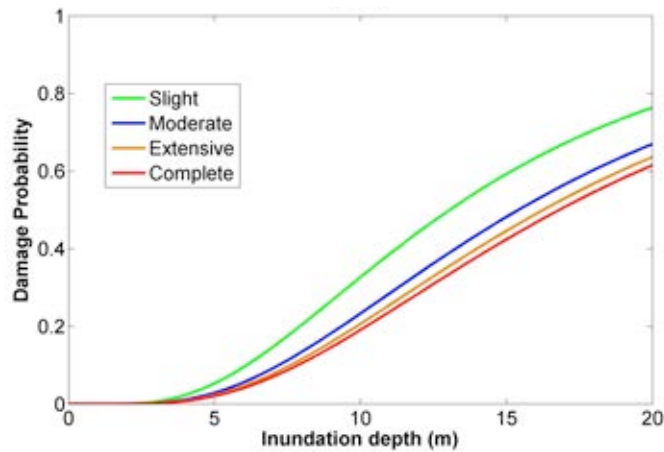
Fig. 5.12 Fragility curves for container cranes subject to tsunami.

6 Performance and loss assessment of complex geographically distributed CIs accounting for interdependencies

In a complex system, elements are interconnected and their relationship is multifaceted; their properties cannot be properly understood without assessing their interrelationship with each other as well as their relationship with the wider system and its environment.

When systems become overly complex, their behaviour cannot be easily predicted by traditional methods of analysis: breaking a system into its component parts and analyzing elements in detail. Additionally, a complex system can exhibit properties that cannot be understood by examining the system's individual components. Complex systems exhibit patterns, outcomes, and properties not present in any of their individual elements.

In this case, the performance of the whole infrastructure (CI facility) should be addressed using appropriate methods and evaluation measures, based on integrated models of critical infrastructure systems.

The quantitative measure of the performance of the whole system and its elements when subjected to a seismic hazard is given by Performance Indicators (PI's). They express numerically either the comparison of a demand with a capacity quantity, or the consequence of a mitigation action, or the assembled consequences of all damages (the "impact"). Performance indicators, at the component or the system level, depend on the type of analysis that is performed. Four main types of system evaluations can be considered:

- **Vulnerability analysis:** This level considers only the potential physical damages of the components of the systems, with no consideration of functionality of either the elements or the whole system.

- **Connectivity analysis:** Here the probability of the demand nodes to be connected to functioning supply nodes through undamaged paths is analyzed. In this approach the damaged components are removed from the network and the adjacency matrix is updated accordingly, thus pointing out the nodes or areas that are disconnected from the rest of the system. Connectivity analysis gives access to indices such as the connectivity loss (measure of the reduction of the number of possible paths from sources to sinks).

- **Capacity analysis**: The ability of the system to provide to the users the required functionality is quantified. For utility networks, graph algorithms and flow equations can be used to estimate capacitive flows from sources (e.g. generators, reservoirs) to sinks (i.e. distribution nodes), based on the damages sustained by the network components (from total destruction to slight damages reducing the capacity). Capacitive modelling yields more elaborate performance indicators at the distribution nodes (e.g. head ratio for water system, voltage ratio for electric buses) or for the whole system (e.g. system serviceability index comparing the customer demand satisfaction before and after the seismic event).

- **Fault-tree analysis**: It concerns CIs, where multiple conditions are necessary for the systems to ensure its function. This approach aims to evaluate the remaining

operating capacity of systems with multiple operators. The system is broken down into components, each one of them being connected with logic operators. It is generally used for the derivation of fragility curves for specific components that comprise a set of sub-components (e.g. health care facilities, water treatment plants).

Specifications on performance and risk assessment for the three spatially distributed CIs are given in the following.

6.1 PERFORMANCE AND LOSS ASSESSMENT OF CI-B1: MAJOR HYDROCARBON PIPELINES, TURKEY

Buried continuous welded steel pipelines as major hydrocarbon pipelines are commonly used as reliable and economic means to transport oil and gas across the world. Such pipelines generally cover long distances and their exposure to the earthquake threats while crossing active faults in earthquake-prone regions cannot be overlooked at the design stage. The high quality of continuous steel pipes makes them not sensitive to the shaking ground motions such as PGA and PGV but more vulnerable to the fault displacement at fault crossings. This chapter develops a full probabilistic risk assessment of pipeline failure at fault crossings. The proposed theory is implemented to the case study for a strike-slip fault. Two uncertainties from the earthquakes, i.e., fault displacement and fault-pipe crossing angles, are considered in the assessment. The influence of these uncertainties on the risk of pipe failure at strike-slip fault crossings is studied. The seismic risk of pipeline failure due to the actual fault rupture occurring at a distance far away from the mapped fault trace is also examined. This quantitative risk can be used as a useful reference for engineers to design and retrofit pipes at fault crossings.

6.1.1 Introduction

Buried continuous welded steel pipelines as major hydrocarbon pipelines are regularly used as reliable and economic means of transporting oil and gas across the world. Such pipelines generally cover long distances and their exposure to the earthquake threats while crossing active faults in earthquake-prone regions cannot be overlooked at the design stage. Unlike water pipelines, which are generally constructed as segmented pipes, the continuous steel pipelines are more likely to suffer the damage due to permanent fault deformations (PDFs) rather than the wave propagation. Many examples have demonstrated the failure of the pipelines due to the fault crossings during the past earthquakes (e.g. 1971 San Fernando, 1994 Northridge, 1999 Kocaeli and 2001 Alaska earthquakes). The failure of water, oil and gas pipelines caused massive human loss, enormous economic loss, widespread fires and environment pollution in these events. Therefore, the seismic hazard and risk assessment of the continuous pipelines due to fault crossings should be performed to mobilize the most efficient retrofitting techniques for risk mitigation.

The probabilistic seismic risk analysis of buried pipelines has been discussed in various studies since 1980s (e.g. McGuire 1988; Mashaly and Datta 1989; Pineda-Porras and Ordaz 2012; B. Omidvar et al. 2013; S Esposito 2014, M mousavi et al. 2014). The seismic risk assessment is generally achieved by using the empirical fragility functions, which conventionally relate the repair rate to ground shaking (e.g. Katayama et al. 1975; O' Rourke and Jeon 1999; ALA 2001; HAZUS 2004) or recently to ground strain (e.g. O' Rourke 2009; O' Rourke et al. 2014). However, these fragility functions are only applicable to the buried

segmented pipelines that are more sensitive to the transient ground shaking. The failure due to fault crossings for the continuous steel pipelines that are not vulnerable to the transient ground shaking has not been emphasized with sufficient details.

When a continuous pipeline is subjected to fault rupture, the resulting stresses along the pipeline are in a complicated mechanical process since they depend on many factors such as fault type, pipe material and pipe geometry with respect to fault strike, and soil property surrounding the pipe etc. Abundant studies in the literature have investigated about the pipeline mechanical behavior at fault crossings (e.g, Datta 1999; Vazouras et al., 2010; Vazouras et al., 2012; Karamitros et al., 2011; Karamitros et al., 2007; Uckan et al., 2015). Besides the development of probabilistic fault displacement hazard analysis (PFDHA) (Stepp et al., 2001; Youngs et al., 2003; Petersen et al., 2011) enabled us to assess the fault displacement hazard in a probabilistic manner. After developing probability-based hazard on permanent fault displacement, it is always possible to assess the probabilistic risk on the continuous pipeline system. Understanding the risk level in a pipeline for different fault crossing scenarios would enable the pipeline operator to take necessary actions to reduce pipeline vulnerability against different earthquake levels.

This section presents the theory and application of seismic risk assessment for buried continuous steel pipelines at fault crossings. The proposed approach aims to calculate the expected annual rate of pipeline failure due to permanent fault displacement. The chapter first describes the theory of probabilistic risk assessment of pipeline failure that is followed by its implementation for strike-slip faults. The presented case studies examine the influence of some critical variables in the risk assessment. The investigated variables includes these from seismic hazard such as different earthquake magnitude scenarios, mapping accuracy (Petersen et al. 2011), fault-pipe intersection angle and its uncertainty, and these properties of the pipeline and its surrounding soil such as pipe buried depth, ratio of pipe diameter to its thickness, soil condition surrounding the buried pipe.

6.1.2 Methodology

The seismic risk of pipelines due to fault rupture at the surface is represented by the annual probability of the pipeline failure. It is achieved by integrating the probabilistic fault displacement hazard, mechanical response of pipe due to fault displacement and empirical pipe fragility function. Since both tensile and compressive strains developed along the pipe during an earthquake can cause pipe's failure, the seismic risk of pipe failure should consider the aggregated effects of these two strain components. The formulae to calculate the seismic risk are given by Equations **(6.1)** and **(6.2)**.

$$\lambda = \lambda(FailTen) + \lambda(FailCom) \tag{6.1}$$

$$\lambda(Failure) = \iint_{D\,\alpha} P[\,failure \,|\, \varepsilon(d,\alpha,\boldsymbol{\theta})] f_D(d) f_A(\alpha) d(d) d(\alpha)$$

$$\approx \sum_{i=1}^{n} \sum_{j=1}^{m} P[\,failure \,|\, \mathrm{E} = \varepsilon_{i,j}(d_i,\alpha_j,\boldsymbol{\theta})] \Delta(v_{di}) P(\alpha_j) \tag{6.2}$$

where λ is total annual probability of pipeline failure at the fault crossing. The terms *λ(FailTen)* and *λ(FailComp)* represent the annual probabilities of pipeline failure due to tensile and compressive strains developed along the pipe at the fault crossing, respectively. *λ(Failure)* is either *λ(FailTen)* or *λ(FailComp)* depending on the state of strain in the pipe.

The probability expression in the integral represents the pipe's fragility function given a certain level of pipe strain, ε, that varies with the fault displacement (d) and the fault-pipe crossing angle (α). The probability distributions of fault displacement and fault-pipe crossing angle are represented by $f_D(d)$ and $f_A(\alpha)$. The fault displacement probability is the derivative of fault displacement hazard curve, $\lambda_D(d)$ (i.e., $d\frac{\lambda(d)}{d(d)}$. It indicates the mean annual number of events producing fault displacement exactly equal to a given displacement, d. $\lambda_D(d)$ can either be calculated from the probabilistic fault displacement hazard assessment (PFDHA; Petersen et al., 2011; Youngs et al., 2003) or Monte Carlo based simulations with random fields approach such as in chapter 4.2.1 (e.g. Weatherill et al., 2014). The probability distribution of fault-pipe crossing angle, α, represents location uncertainty in the ruptured fault segment and uncertainties involved with mapping quality and complexity of fault trace that translates into the location of future ruptures (Petersen et al., 2015). $f_A(\alpha)$ can be characterized by normal distribution. The vector $\boldsymbol{\theta}$ in the fragility function describes the parameters (e.g. buried depth, pipe diameter to thickness ratio and etc.) that can affect pipe's seismic response. The uncertainties in such parameters can be accounted for in the total risk by implementing their probability distributions to the integral term given in Equation (6.2).

The integration of above mentioned parameters would yield pipe's seismic risk at the fault crossings. The concept is similar to the conventional probabilistic seismic risk assessment (McGuire, 2004). When the terms in the risk integral are discretized, the integral expressions change into summation terms and the discrete probabilities $\Delta(v_{di})$ and $P(\alpha_j)$ are computed for the combinations v_{di} and α_j (i = 1… n and j = 1…m) where v_{di} is the discrete annual probability of fault displacement being equal to d_i. The $\Delta(v_{di})$ describes the annual probability of fault displacements being among the ith range of fault displacement.

6.1.3 Case studies

Several case studies has been applied in Eq 1-2 in order to show the implementation of the proposed theory and examine the effects of key parameters on the risk assessment of pipeline failure due to fault displacements at fault crossings. The investigated parameters in this section are generally characterized with two categories: seismic hazard parameters and pipeline design parameters, the values of which for case studies are described in Table 6.1. As discussed in the previous section, the pipeline failure risk due to fault displacement is obtained by integrating fault displacement hazard, pipeline mechanical response due to the fault displacement, and its fragility functions which will be introduced in the following sections. Then the resulting risk of pipeline failure will be discussed for the case studies characterized with different values of key parameters.

Table 6.1 The values of investigated parameters in sensitivity analysis for seismic risk assessment of pipelines due to fault displacements

Categories	Key parameters	Considered values
Seismic hazard parameters	Seismic activity	Two Earthquake scenarios in characteristic model: *Scenario1: Mw 7-7.5, slip rate = 15 mm/year* *Scenario2: Mw 7.5-8.0, slip rate = 20 mm/year*
	Fault-pipe crossing angle	A series of angles: 10° to 90° with 1° interval
	Uncertainty of fault-pipe crossing angle	Two standard deviation σ (2σ truncated Normal distribution): 2.5^o and 5°
	Mapping accuracy	One accurate mapping accuracy (Approximate accuracy): *Standard deviation = 43.82m*
Pipeline design parameters	Ratio of pipe diameter to its wall thickness (*D/t*)	Four *D/t*: *144; 96; 72; and 57.6*
	Pipe buried depth	Four depths: *1m; 1.5m; 2m; and 3m*
	Surrounding soil condition	Three types of surrounding soil: *Sand: friction angle=36°, cohesion= 0kPa* *Soft clay: friction angle=0°, cohesion= 50kPa* *Stiff clay: friction angle=0°, cohesion = 200kPa*

6.1.3.1   *Seismic hazard:*

Fault displacement along with ground shaking is the direct hazard from earthquakes. The continuous steel pipelines are not fragile to the ground shaking but more likely to suffer damage due to fault displacement as a result of fault surface rupture. So the fault displacement has been selected as the seismic hazard parameter to be investigated in this chapter. Fault displacement hazard can be assessed in probabilistic manner through probabilistic fault displacement hazard analysis (PFDHA) (Stepp et al., 2001; Youngs et al., 2003). Fault Displacement Prediction Equations (FDPE) proposed by Pertersen et al. (2011) is used within PFDHA. It is an advanced FDPE and targets several uncertainties for the prediction of fault offset: location of fault rupture according to mapping accuracy over the mapped fault; uncertainty of fault displacement given a magnitude earthquake; uncertainty of

the displacement along the length of the fault. Therefore these uncertainties are also considered within the case studies.

Two earthquake scenarios with different magnitude ranges and slip rates (given in Table 6.1) are investigated for a straight fictitious mapped fault characterizing with the pure characteristic earthquake recurrence model. The pipeline is assumed to cross the center of the strike slip fault, which is expected to be the worst case. MC-simulation analysis used in chapter 4.2.2 is used to achieve fault displacement hazard curves. The resulting hazard curves of fault displacements from 0.01m and 15m at the center of the fault for the two earthquake scenarios are shown in Fig. 6.1a. Besides fault displacement hazard curves on the mapped fault (fault distance = 0m), the hazard curves on the sites at distance (i.e., 50m, 100m and 150m) from the mapped fault (namely, fault distance) are also evaluated and plotted in Fig. 6.1a, through considering mapping accuracy incorporated in PFDHA proposed by Stepp et al., 2011.
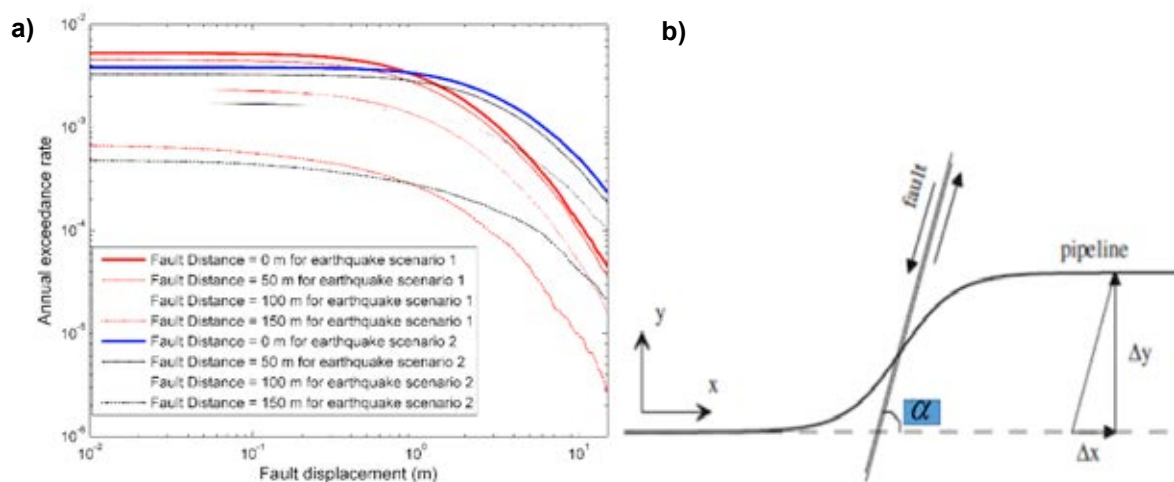
Fig. 6.1 a) seismic hazard curves: annual exceedance rate of fault displacement for sites at different fault distances over the mapped fault (fault distance: 0, 50, 100 and 150m) for earthquake scenario 1 and 2, b) Geometry illustration of a pipe and fault; α is the fault-pipe crossing angle, also used in Eq. 6.2; Δx and Δy are the tangential and normal components to the pipeline of strike-slip fault displacement, respectively.

6.1.3.2 Structures

Fig. 6.1b shows a buried pipe crossing the strike-slip fault. When the fault ruptures up to the ground surface, the pipeline will be subject to an imposed deformation pattern, shown in Fig. 6.1b, and may suffer high stresses and strains in critical locations, which can be well beyond the elastic range of pipe material and may lead to the pipe failure. The strain is largest near the fault rupture and drops with the distance away from the fault rupture. The largest tensile and compressive strains along the pipeline will be implemented in the integration described in equation **(6.2)** to calculate the risk of pipeline failure at the fault crossings.

In the case studies we use the analytical methodology of Karamitros et al. (2007) to calculate strains along the pipeline at the fault crossings during an earthquake. This method is appropriate to a wide range of application by introducing a number of refinements on the model. The cases studies apply S450 steel pipelines featuring an external diameter D of 0.9144m (36 in.) with four values of pipe wall thickness t, namely 6.35 mm (1/4 in.), 9.53 mm

(3/8 in.), 12.7 mm (1/2 in.) and 15.88 mm (5/8 in.). Accordingly, the corresponding diameter-to-thickness ratios *D/t* are equal to 144, 96, 72, and 57.6, respectively, which cover a wide range of oil and gas pipeline applications.

Soil condition surrounding buried pipes (i.e. the properties of surround soil) is also a critical factor affecting the seismic performance of pipeline imposed by fault displacements of earthquakes. We investigated three soil types: dense sand, soft clay and stiff clay soil. The interaction between soil and pipeline is modeled with bilinear elasto-plastic soil springs, which are defined in ALA 2001-2005. The investigated pipes are buried at four depths (i.e., 1m, 1.5m, 2m and 3m), given in Table 6.1. The soil spring properties for the each of soil types and buried depths are presented in Table 6.2. As one part of the calculation results, the maximum tensile and compressive strains along the pipeline with 9.53mm thickness for 1-to-3 m buried depth are shown in Fig. 6.2. It indicates that maximum compressive and tensile strains along the pipelines surrounded by sand soil are much more sensitive to buried depth than those by clay soil. As can be seen from Table 6.2, *Tu* does not change with buried depth and the *Qu* increases slightly with the rise of buried depth for the clay soil condition.

Table 6.2 Soil spring properties calculated with the guidelines ALA 2001-2005; H is pipe buried depth; T_u is maximum axial soil force per unit length of pipe for axial soil spring; Q_u is maximum lateral soil force per unit length of pipe for lateral soil spring; ΔT_u and ΔQ_u are displacement at T_u and Q_u, respectively. 0.5Δ is the displacement at T_u or Q_u for elastic-plastic soil springs used.

Soil condition	H (m)	T_u (kN/m)	$0.5\Delta_{Tu}$(mm)	Q_u (kN/m)	$0.5\Delta_{Qu}$ (mm)
Dense sand	1	18.2	2.5	159.3	29.1
	1.5	27.4	2.5	262	39.1
	2	36.5	2.5	378.3	49.15
	3	54.7	2.5	647.5	69.4
Soft clay	1	135.8	5	232	29.1
	1.5	135.8	5	258.7	39.1
	2	135.8	5	275.5	49.15
	3	135.8	5	295	69.4
Stiff clay	1	220.9	4	928.1	29.1
	1.5	220.9	4	1034.8	39.1
	2	220.9	4	1101.9	49.15
	3	220.9	4	1180	69.4
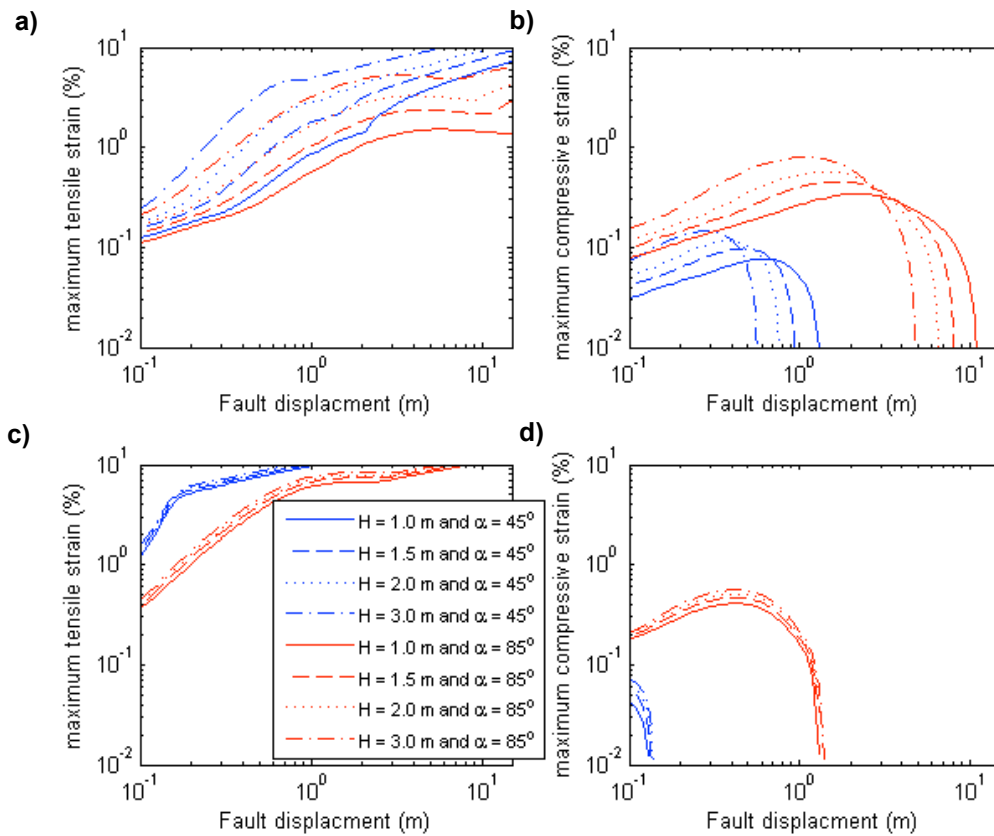
Fig. 6.2 Material behavior of the pipe with 0.9144 m diameter and 9.53 mm wall thickness, buried by dense sand (a, b), stiff clay (c, d) soil, due to variable fault displacements: maximum tension strain (a, c) and maximum compression strain (b, d); H and α represent pipe buried depth and fault-pipe intersection angle, respectively.

6.1.3.3 Pipe fragility relation

Pipe failure can be characterized by a cumulative probability of failure curve (normally referred to as a fragility curve), which is defined by a lognormal cumulative distribution function. The pipeline fragility curves relate the probability of pipeline failure (i.e., P[failure/$\varepsilon(d, \alpha, \boldsymbol{\theta})$] in Equation 6.2) to the tensile and compressive strains. Due to lack of relevant information on pipeline failure criteria, a simple criterion has been adopted herein to develop for longitudinal compression and tension strain associated with loss of pressure integrity. In order to develop the empirical fragility curve for pipeline failure in the compressive and tensile manner we fitted the fragility function to several sets of data given below. These sets of data are composed of several couples of maximum tension or compression strains along the pipeline at fault crossings and their corresponding probabilities of pipeline failure, respectively. We adopt the method of minimizing the sum of squared errors (SSE) to fit fragility function (described in Equation 12 in the study of Baker, 2015).

For the buried welded-steel pipelines with good-quality girth welds, which is considered in this section, it is known that the tensile strain equal to 3 and 10% are assumed to have 10 and 90% likelihood of failure, respectively (Wijewickreme et al., 2005). In order to control the left tail value of the fitted fragility curve, another set of data, that is 0% probability of failure vs. 1% tensile strain, is used in the curve fitting. These three sets of data are applied to fit

70

the fragility curve of pipeline tensile strains (the pipe fails due to its tension strain) and the result is displayed in Fig. 6.3a.

Using the same methods, the fragility curves for the pipe in compression (the pipe fails due to its compression strains) can be developed. Three sets of data are used to model the fragility curve. Each set of data contains a likelihood of pipeline failure due to compressive strain and the corresponding value of the compressive strain. The development of the pipeline fragility curve for compressive stains is more complicated, since the probability of pipeline failure due to compressive strain is estimated using the ratio of pipeline diameter D to pipe wall thickness t. Wijewickreme et al. (2005) assume that compressive strains corresponding to 10% and 90% likelihood of failure are assumed to be equal to 0.4/ (D/t) and 2.4/ (D/t), respectively. Similarly, to make the left value of the fitted fragility curve more reliable, we assume that the one-third of 0.4/ (D/t) compressive strain causes 0% likelihood of failure. The resulting fitted fragility curve of pipeline failure due to compressive strains is shown in Fig. 6.3b for different D/t values. The resulting mean values and standard deviations for developing the cumulative probability of the pipeline failure curve (fragility curve of compressive strain) for four values of D/t used in the case studies are presented in Table 6.3. These values will be used to calculate the pipeline seismic risk in the following subsection.
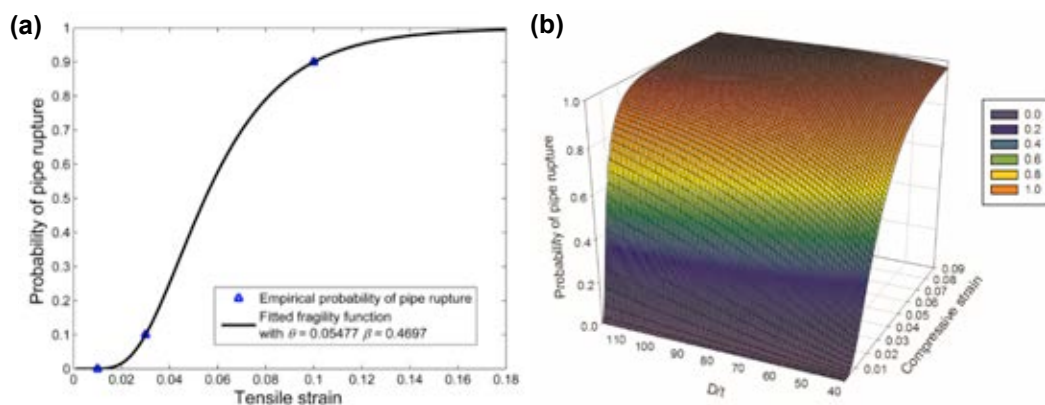
Fig. 6.3 Probability of pipeline failure due to its tensile strain (a) and due to its compressive strain (b).

Table 6.3 Fitting mean value and standard deviation of fragility curve for compressive strain of pipelines investigated herein

D/t	θ	β
57.6	0.0170	0.6987
72	0.0136	0.6987
96	0.0102	0.6987
144	0.0068	0.6987

6.1.3.4 Risk of pipeline failure due to fault displacement

Though integrating via Equations **(6.1)**-**(6.2)** using the aforementioned values of key parameters summarized in Table 6.1, this subsection shows and discusses the seismic risk of pipeline failure, expressed as annual probability of pipeline failure due to fault displacement. The results are presented in Fig. 6.4-Fig. 6.7. Note that the variability of fault-pipe crossing angles is considered only for the case study in Fig. 6.5, and the fault-pipe crossing angles are deterministic in other cases studies. The annual probability of the pipeline failure mentioned in Fig. 6.4-Fig. 6.6 means the pipeline fails due to the fault displacement hazard on the mapped fault (fault distance equals to zero). The seismic risk of the pipeline failure induced by the fault displacement hazard off the mapped fault (fault distance is not equal to zero) are also investigated in Fig. 6.7.

Fig. 6.4 compares the likelihood of pipeline failure per year when considering the contribution to the risk only from pipeline tensile strain and from both tensile and compressive strains imposed by fault displacements for pipelines at crossing angles from 10° to 90° for different surrounding soil conditions. In Fig. 6.4a, it is shown that considering the influence of compressive strains on the seismic risk significantly rises annual probability of failure for the pipeline crossing the mapped fault at angles from 70 to 90 degree, with surround sand soil. The influence of compressive strains on the risk of pipeline failure decreases with the buried depth, suggested by Fig. 6.4b. It is observed in Fig. 6.4c-d that this influence is relatively smaller for the clay soil condition compared to the sand condition. It also shows that the D/t ratio does not impact the fault-pipe crossing angle at which the annual probability of pipeline failure reaches the lowest. For example the angle corresponding to lowest probability of pipeline failure associated with potential tensile and compressive strains for surrounding sand soil is around 75°, shown in Fig. 6.4a. But this angle will become larger with increase of pipeline buried depth. The best fault-pipe intersection angle to achieve lowest risk of pipeline failure is from 75° to 80° for the sand surrounding soil.

Fig. 6.5 illustrates the risk of pipeline failure considering the uncertainty of fault-pipe crossing angles for pipelines featuring different *D/t* ratios when both compression and tension strain are considered. The uncertainty is considered by assuming the angles normally centered at the mapped fault-to-pipe intersection angles from 10° to 85° and 10° to 80° (displayed on horizontal axis in Fig. 6.5) with standard deviation σ equal to 2.5^o and 5°, respectively. It is observed that the consideration of variability of crossing angles does not effects the risks of pipeline failure for the pipelines surrounded by soft and stiff clay. However for the pipelines buried at 1m depth with sand soil condition, the variability of crossing angles causes the increment of risk of pipeline failure for mapped fault-to-pipe crossing angles from 70 to 85 degree. It is probably because the variability induces the risk from larger crossing angles (larger than 80 or 85 degree) which significantly result in increasing the risk of the pipeline failure. But this influence dissipates as the pipelines are buried deeper with sand soil condition. It is observed that the optimal crossing angles for the seismic risk of pipeline failure under sand soil condition are around 75° depending on the degree of variability for the crossing angle.
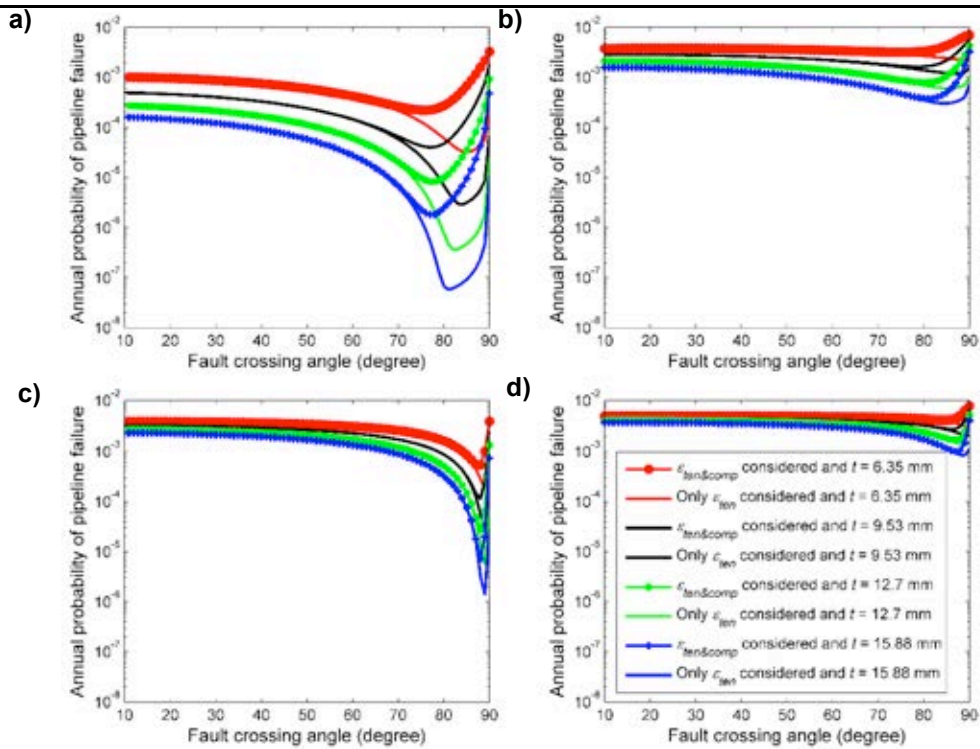
Fig. 6.4 Trend of annual probability of pipeline failure with fault crossing angles due to the results of considering compressive and tensile strains or only tensile strain along the pipeline buried under dense sand soil with depth equal to 1 m (a) and 1.5 m (b), and under soft clay(c) and stiff clay (d) soil with buried depth of 1 m; $\varepsilon_{Ten\&Comp}$ represents both tensile and compressive strain consideration, and ε_{Ten} is tensile strain consideration, and D indicates the diameter of the pipe.
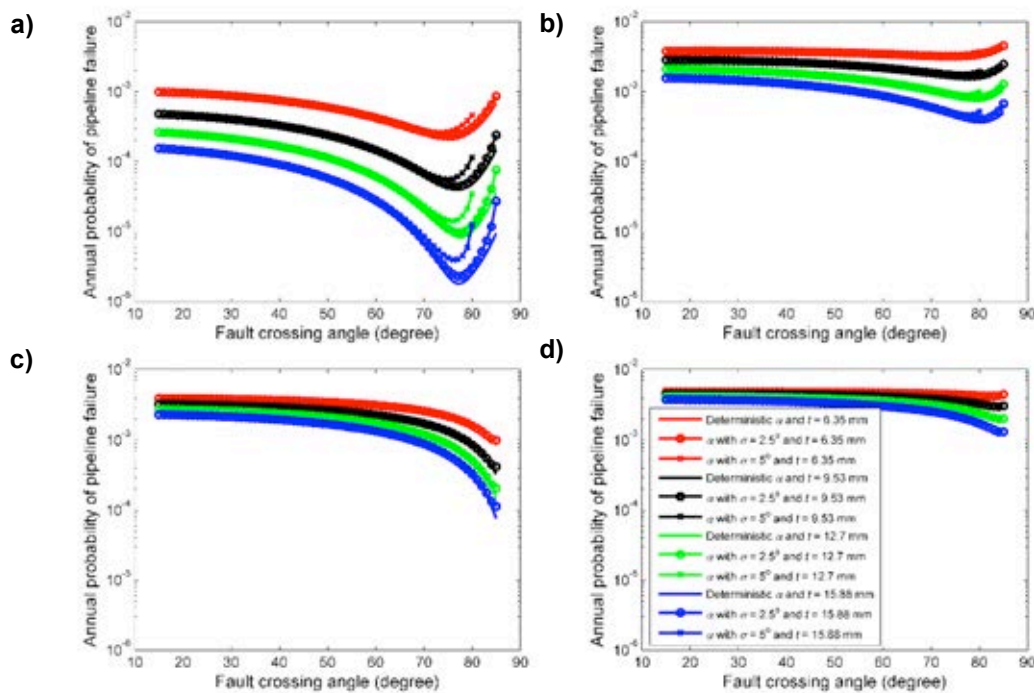
Fig. 6.5 Trend of annual probability of pipeline failure with deterministic fault crossing angle and crossing angle with variability on it, due to compressive and tensile strains along the pipeline buried under dense sand soil with depth equal to 1m (a) and 3m (b), and under soft clay(c) and stiff clay (d) soil with buried depth of 1m.

In the Fig. 6.6 we investigate the seismic risk of pipeline failure accounting for both compressive and tensile strains contribution during fault rupture when different earthquake scenarios are considered. It is observed from Fig. 6.6a-b that for sand soil condition the annual probability of pipeline failure in the earthquake scenario 2 is higher than that in the earthquake scenario 1 for the pipelines at crossing angles from 10° to 80°. However the risk of pipeline failure trends to be the same for the crossing angles larger than 80°. For the clay soil condition, the difference resulted from different earthquake scenario is not as explicit as for the sand soil condition.

It should be noticed that the annual probability of pipeline failure in earthquake scenario 1 even larger than earthquake 2 for the pipelines under the stiff clay soil condition for the fault crossing angles from 10° to 60°. It is probably because the strains along the pipeline imposed by fault displacement develop much faster under stiff soil condition than sand soil condition, which is shown in Fig. 6.2c. For example, the maximum tensile strain along the pipe reaches to around 7% for the displacement equal to 0.3 m for stiff clay soil condition. On the other hand, it is only less than 1% for the sand soil condition. The higher annual exceedance rate of small fault displacements (less than 1 m, illustrated in Fig. 6.1a) for the earthquake scenario 1 compared to earthquake scenario 2 results in a higher integration result in the risk in Equation **(6.2)**.
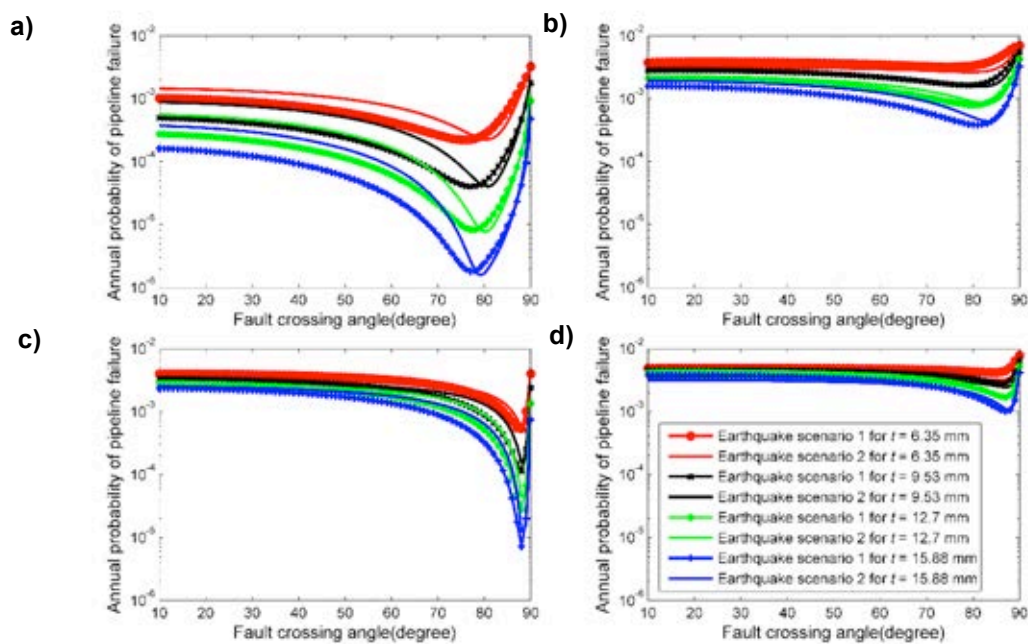
Fig. 6.6 Annual probability of pipeline failure vs. deterministic fault crossing angles, due to compressive and tensile strains along four considered pipelines (D = 6.35, 9.53, 12.7 and 15.88 mm) buried under dense sand soil with depth equal to 1m (a) and 3m (b) and under soft clay(c) and stiff clay (d) soil with buried depth of 1 m for different earthquake scenarios. (Scenario 1: M_w = 7.0-7.5 and slip rate = 15 mm/year; Scenario 2: M_w = 7.5-8.0 and slip rate = 20 mm/year).

Fig. 6.7 shows the trend of the annual likelihood of the pipeline failure due to fault displacement at sites with a fault distance for fault-pipe crossing angle equal to 80° when considering the contribution of both the compression and tension strains to the risk. It indicates that the risk of pipeline failure exponentially decreases with the fault distance, which is closest distance of a site to the mapped fault. However the risk due to the actual fault rupture away from the mapped fault does not explicitly reduce within 50 m fault distance, when the approximate mapping accuracy is considered. The risk of pipeline failure

for different crossing angles and surrounding soil types follows the same changing pattern with fault distance.
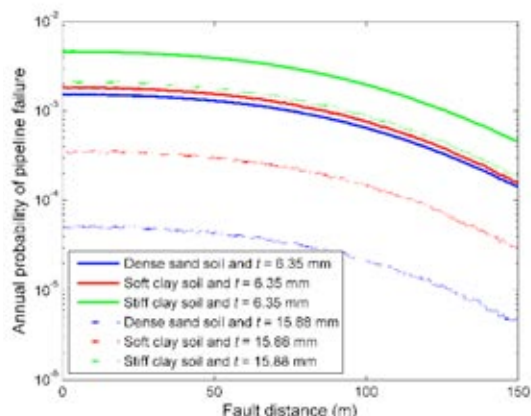
Fig. 6.7 Annual probability of pipeline failure vs. fault distance (the distance of a site away from the mapped fault), due to compressive and tensile strains along two considered pipelines (D = 6.35 and 15.88 mm) buried under dense sand, soft clay and stiff clay soil with depth equal to 3 m for 80° crossing angle and earthquake scenario1. (M_w = 7.0-7.5 and slip rate = 15 mm/year).

6.1.4 Conclusions

Continuous buried steel pipelines are normally used to transit the gas and oil from the sources to other places. As high quality pipelines, they are more sensitive and vulnerable to the permanent fault rupture rather than transient ground shaking during earthquakes. Therefore, this chapter develops a full probabilistic risk assessment of pipeline failure at fault crossings. The seismic risk of pipeline failure is expressed as the annual probability of pipeline failure at crossings. Through case studies, a set of key parameters have been investigated about the impact on the seismic risk of pipeline failure due to fault displacement, leading to the following conclusions:

(1) The compression strain significantly increase the annual probability of pipeline failure at fault crossings during earthquakes for sand soil for fault-pipe crossing angles from 70 to 90 degree, and this impact declines with the increase of the pipeline buried depth. However for soft and stiff clay the impact is not explicit until for the crossing degree close to 90°.

(2) Considering the variability of fault-pipe crossing angles evidently increases the seismic risk of pipeline failure when the pipeline having mapped fault-pipe crossing angles larger than 70° is buried at shallow depth under sand soil condition. However for the deep buried depth under sand soil condition and soft and stiff clay soil condition, the variability of crossing angles seem not influence on the risk of pipeline failure.

(3) Larger earthquake scenarios produce higher failure risk of pipelines having crossing angles less than 80°. However the annual exceedance rate of small values of fault displacement may significantly contribute to the risk of pipeline failure for stiff clay soil condition, probably leading a higher value of failure risk of pipelines having small crossing angles (less than 60° in this study).

(4) Considering the probability of pipeline failure, the optimal angles for the sand soil, which produce the lowest annual failure of pipelines having crossing angles are between 70° and 80°. They barely change with the D/t and buried depth. The optimal crossing angles for clay soil are larger than those for sand soil.

(5) The risk of pipeline failure at sites off the mapped fault may be important when the mapped fault is not accurate and described with high variability of mapping accuracy (the actual fault is assumed to be normally distributed over the mapped fault). This pipeline may have the almost the same level of failure risk within the tens or hundreds meters over the mapped fault, depending on the mapping accuracy. This quantitative risk of pipeline failure at the site off the mapped fault can be estimated with the proposed methodology.

Two important aleatory uncertainties from earthquakes are considered during the risk analysis: fault displacement and fault-pipe crossing angle. Uncertainty of pipeline parameters and soil, such as soil property, can also be taken into account in the pipeline failure risk by cooperating them in the integration shown in Equation 6.2 and following the same procedure as this chapter. We did not account for the epistemic uncertainty from the pipeline numerical modelling used to calculate the maximum compression and tension strains with given fault displacement and crossing angle. But in order to obtain more accurately strain the finite element analysis (e.g. Vazouras et al., 2012) or simplified finite element analysis (e.g. Uçkan et al., 2015) methods are necessary. However these methods would largely increase the computation penalty.

6.2 PERFORMANCE AND LOSS ASSESSMENT OF CI-B2: GASUNIE NATIONAL GAS STORAGE AND DISTRIBUTION NETWORK, HOLLAND

For the geographically distributed network selected, dedicated performance indicators are to be identified that express the character of supply and demand of gas delivery as well as the presence of redundancies. Multiple paths may exist from a demand node to one or more supply nodes. Redundancy will be beneficial for the Gasunie case as the man-induced earthquakes in Groningen are likely to induce only very local damage (not extending over a greater part of the network). Hence, in accordance with the introduction of this chapter, focus will be put on connectivity analysis and capacity analysis (apart from mere physical damages of the components of the systems). For these performance indicators definitions as presented in Esposito, 2011 for Serviceability loss (SR) and Connectivity loss (CL) will be used:

The Serviceability Ratio (SR), was originally defined by Adachi and Ellingwood (2008) for a water supply system. The index is directly related to the number of distribution nodes in the utility network, which remain accessible from at least one supply facility following the earthquake. It is computed as

$$SR = (\sum w_i X_i) / \sum w_i \qquad (6.3)$$

where SR is the serviceability ratio of the system defined on the domain [0,1], w_i is a weighting factor assigned to the distribution node i and X_i represents the functionality of facility i, which is modeled as the outcome of a Bernoulli trial (X_i = 1 if facility is accessible

from at least one supply facility), and summation is performed over all demand nodes (receiving stations).

Connectivity Loss (CL), Poljanšek et al., 2011, measures the average reduction in the ability of receiving stations to receive flow from sources (gas fields and LNG terminals) counting the number of the sources connected to the i-th station in the original (undamaged) network, $N^i_{source,orig}$ and then in the damaged network, $N^i_{source,dam}$. It is expressed by the following equation:

$$CL = 1 - (N^i_{source,dam} / N^i_{source,orig})_i \qquad (6.4)$$

The backbone of the performance and risk assessment will be the methodology of SYNER-G (Pitilakis et al., 2014b). The methodology was also followed by Esposito, 2011 for the seismic risk analysis of gas distribution networks.

It will include the "shakefields" method (Weatherill et al., 2014) for maps of sampled correlated seismic intensities at the sites of the nodes and branches in the gas distribution network. The Dutch Meteorological Institute (Dost et al. 2013), performed the data analysis and a Probabilistic Seismic Hazard Analysis (PSHA) with all data available until 2013. The Ground Motion Prediction Equation (GMPE) used for the prediction of the ground motion characteristics (peak ground acceleration and peak ground velocity), as function of the magnitude Mw and source-site distance R, is the GMPE of Akkar et al. (2014c) recently derived on a large dataset that includes shallow and low magnitude events and a correction factor to take into account the faults typology and amplification for local seismic response in soft soil that makes it more suitable for the typology of the events in the Groningen area.

The gas distribution network itself will be modelled as a graph composed by the set of nodes connected by edge links amongst each other. The stations, regulators groups and joints are thus represented by nodes while pipes are represented by links.

Through MC sampling of events, Fig. 6.8, annual exceedance curves of the performance indicators will be calculated, making use of fragility curves for pipelines and stations. An example of such a curve as taken from the work of Esposito, 2011, is presented in Fig. 6.9 for a study case in Italy.
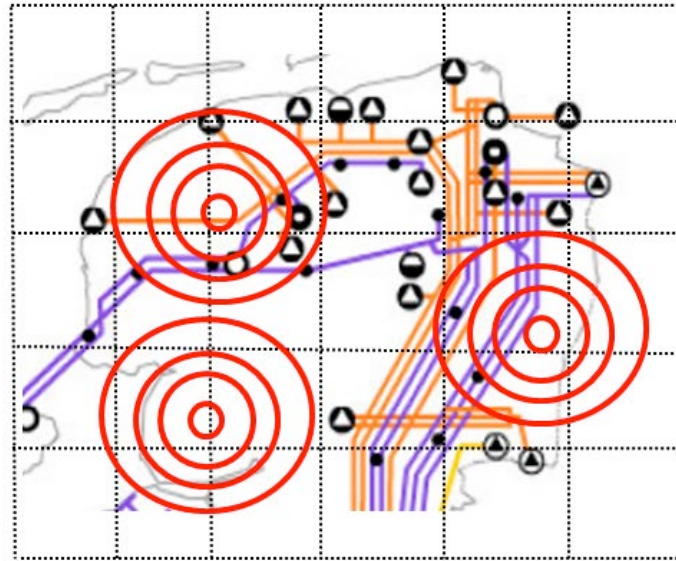
Fig. 6.8 Schematic representation of sampling earthquake events for the gas distribution net.
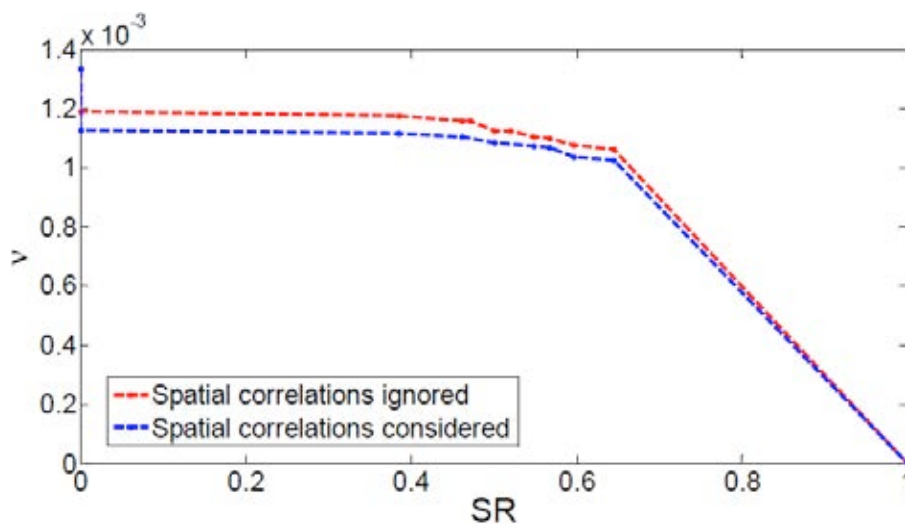
Fig. 6.9 Example of annual exceedance curve for serviceability ratio from Esposito, 2011

6.3   PERFORMANCE AND LOSS ASSESSMENT OF CI-B3: PORT INFRASTRUCTURES OF THESSALONIKI, GREECE

Port transportation systems are vital lifelines whose primary function is to transport cargos and people. They contain a wide variety of facilities for passenger operations and transport, cargo handling and storage, rail and road transport of facility users and cargoes, communication, guidance, maintenance, administration, utilities, and various supporting operations. Thus, harbors comprise complex systems consisting of several lifelines and infrastructures, which interact with each other and with the urban fabric. For the assessment of the complex system performance, contributions of all components, and their interactions, have to be appropriately accounted for.

Current engineering practice for seismic risk reduction of port facilities is typically based on design or retrofit criteria for individual physical components. However, the resilience and continuity of shipping operations at a port after an earthquake depends not only on the performance of these individual components, but on their locations, redundancy, and physical and operational connectivity as well, that is, on the port system as a whole. Moreover, since ports comprise geographically distributed systems, they are exposed to variable seismic ground motions, often presenting important incoherency (ground shaking effects) and to geotechnical hazards such as liquefaction, landslides and fault ruptures. Seismic risk analysis of such networks requires the consideration of the ground motion spatial correlation that forms the basis for the systemic risk analysis.

In the followings, a specific methodology and tools are presented for the assessment of the systemic performance and loss of harbors, simulating port operations and considering also the interactions among port elements. Performance and loss assessment of port infrastructure is mainly based on the general framework and methodology developed within the European program SYNER-G (Pitilakis et al., 2014b). This methodology potentially accounts also for epistemic uncertainty, taking into consideration uncertainty in models' parameters (through a hierarchical acyclical chain of probabilistic distributions). In addition, it can be applied within techniques like Logic Trees or Ensemble Modeling (see D3.1, Selva et al., 2015) to quantify also epistemic uncertainty. Even though the SYNER-G methodology has been specifically designed for seismic hazard only (Cavalieri et al., 2012; Argyroudis et al., 2015), it can be straightforwardly extended to other single natural hazards (that is, it can be adopted with minor changes to all ST levels involving single hazards). On the contrary, further developments are required if multiple hazards should be considered.

The objective of the analysis is to evaluate probabilities or mean annual frequency of events defined in terms of loss in performance of networks. The analysis is based on an object-oriented paradigm where systems are described through a set of classes, characterized in terms of attributes and methods, interacting with each other. The physical model for each network starts from the SYNER-G taxonomy and requires: a) for each system within the taxonomy, a description of the functioning of the system (intra-dependencies) under undisturbed and disturbed conditions (i.e., in the damaged state following an earthquake); b) a model for the physical and functional damageability of each component (fragility functions); c) identification of all dependencies between the systems (inter-dependencies); and d) definition of adequate Performance Indicators (PIs) for components and systems (Pitilakis et al., 2014b).

The computational modules include the following main models: a) *seismic hazard class* modelling earthquake events and corresponding seismic intensity parameters, b) *network class* modelling physical damages of networks' components and the overall system's performance and c) *interdependencies models* simulating specific interactions between systems. The hazard model provides the means for: i) sampling events in terms of location (epicentre), magnitude and faulting style according to the seismicity of the study region and ii) maps of sampled correlated seismic intensities at the sites of the vulnerable components in the infrastructure ('shakefields' method, Weatherill et al., 2014). When the fragility of components is expressed with different IMs, the model assesses them consistently. Probabilistic evaluation of the performance of networks is carried out by means of Monte Carlo simulations. For simplicity, the methodology is focused on performance without reparations (emergency phase). The final goal is to assess the exceedance probability of different levels of performance loss for each system under the effect of any possible seismic input. This output, represents the performance curve, and is the equivalent of risk curves for

non-systemic probabilistic assessments in single (e.g. PEER formula, Cornell and Krawinkler, 2000) and/or multi-risk (e.g. Selva, 2013) analysis. Disaggregation and correlation procedures are also used at probability level (e.g. design scenario) and loss level (e.g. unacceptable loss, as defined by stakeholders).

6.3.1 Systemic Vulnerability Methodology for Ports

For the assessment of the systemic vulnerability of harbors, it is essential to simulate port operations. Since most of the dry cargo in modern ports is containerized, focus has been given on the operation of container handling. However, bulk cargo is also important from the viewpoint of risk management on economic activities such as industrial and insurance market. Given that, in the aftermath of significant natural disasters such as an earthquake event, a port can operate as a "gate" for delivering the necessary assistance to the city, the importance of this analysis may also go beyond the strictly economic consequences. The passenger movement is also an important element to monitor a depression and recovery process of port function. However, there is not enough data on passenger movement to assess the vulnerability in past earthquake events. From this point of view, it would be difficult to develop simulation models for movement of passengers.

Therefore, only container and bulk cargo movements of ports are simulated. The assumption of discrete type of cargo handling (container or bulk cargo) per terminal is made (each terminal is assumed to be either container or bulk cargo). The elements studied include piers, berths, waterfront and container/cargo handling equipment (cranes). Waterfronts and cranes are the physical components of the harbor. Piers and berths are structural (functional) elements. Groups of several berths compose a pier. Each berth is a part of a waterfront designed to serve one ship, and it consists of a portion of a waterfront served by one or more cranes. The berth length is estimated based on the pier's operational depth. To quantify the capacity of berths, the capacity of cranes (lifts per hour/ tons per hour) is considered in the evaluation. The main Performance Indicator (PI) used is the *total cargo/containers handled and/or delivered (to the port's gate) in a pre-defined time frame per terminal and for the whole port system.* The main interdependency considered is between the cargo handling equipment and the Electric Power Network (EPN), in particular for the electric power supply to cranes. If a crane node is not fed by the reference EPN node (electric supply station) with power and the crane does not have a back-up power supply, then the crane itself is considered out of service. Road (RDN) closures are also another important dependency, since the delivering process of cargo/containers from the terminals to the port gates could be hampered.

The functionality of the harbor is assessed through several system-level Performance Indicators (PIs), as evaluated starting from the effects of seismic events (Fig. 6.10). The general outline of the method is the following:

i.   A set of shakefields seismic events sampled from the seismic hazard is defined.

ii. For each event defined in step (i):

   a) The fields for different intensity measures (shakefields) within the harbor area are sampled.

   b) For all components, physical damages are sampled from their probability of occurrence, as assessed through fragility curves and the modeled intensity measures (step ii,a). In case of components sensitive to both ground shaking (PGA, PSA) and

ground failure (PGD), like cranes, multiple IMs and damage occurrences are sampled independently, and the results are combined through a Fault Tree Analysis (OR gate).

c) Based on the sampled physical damages for each event (step ii,b), the functionality state of each component is assessed, taking also into account system inter- and intra-dependencies.

d) For all systems, the PIs are evaluated based on functionality states of their components (step ii,c) and the systemic analysis. The "moving average" (average over all simulated events) is then computed.

iii. The results of the simulation are estimated. In particular:

a) The mean annual frequency of exceedance (MAF) curve ("performance curve") for all PIs, based on the annual rates of seismic events (step i) and the evaluated PIs (step ii,d).

b) The rates of functionality (or damages) for each component, based on the results of steps ii,c (or ii,b).

c) The correlation between functionality states (or damages) and PIs, based on the results of steps ii,c (or ii,b) and ii,d.

d) Damages, functionality states and PIs are defined for specific events (selected through the MAF curves) corresponding to predefined return periods (step iii,a).

The set of events defined in step (i) must be large enough to obtain reasonably stable results. During the simulation, the process of convergence toward stable results is visually checked from the "moving average" of each PI (step ii,d).
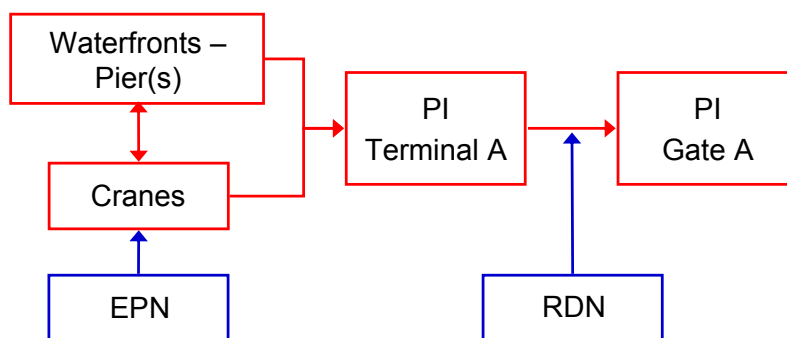
Fig. 6.10 Functionality simulation of port facilities.

In the followings, the PIs for the harbor system are described in detail.

6.3.1.1 Container Terminal

a) Terminal (container handling)

The terminal performance is measured in terms of:

"TCoH = total number of containers handled (loaded and unloaded) per day, in Twenty-foot Equivalent Units (TEU)"

For the harbor, the sum of the PIs relative to all container terminals is considered. The berth (one ship) length is estimated based on the pier's operational depth, inverting the following regression, which gives the depth of the waterfront as a function of the ship overall length (Pachakis and Kiremidjian, 2005):

$$Draft = \begin{cases} -0.100 + 0.056 \cdot LOA, & for \ LOA \leq 200m \\ 7.668 + 0.018 \cdot LOA, & for \ LOA > 200m \end{cases} \tag{6.5}$$

where Draft represents the depth of the waterfront, and LOA is the berth (ship) length.

In practice, for each waterfront, the minimum required berth length is estimated from equation 6.5. The waterfront is divided into the maximum possible number of berth(s) with length longer than the minimum length required; then, each crane is assigned to its closest berth.

For each crane, a demand node of the electric power system (EPN) is defined. This demand node is connected to an EPN substation through non-vulnerable lines. In case of failure of power supply, cranes can work with their back-up power supply, if available. The functionality of the demand node is generally based on EPN system analysis, and it can be based on either capacity or pure connectivity analysis.

To assess the functionality of components, the following rules are set:

- o The waterfront-pier (berth) is functional if damage (D) is lower than moderate (for each IMtype).

- o The crane is functional if damage (D) is lower than moderate and there is electric power supply (from the electric network or from the back-up supply).

- o The berth is functional if the waterfront and at least one crane is functional, otherwise its PI is set to 0.

If the Berth is functional, the PI is set to the sum of the capacities relative to the functioning cranes that contains. Note that, in case of more than one crane, they can work simultaneously to load/ upload containers from the same ship – the time the ship stays at each berth is then reduced.

- o $CraneCapacity_k$ = r*24 TEU/day (Twenty-foot Equivalent Units per day)
- o Berth : PI_{bi} = Σ_k * $CraneCapacity_k$
- o Pier : PI_{pm} = $\Sigma i \ PI_{bi}$
- o Terminal : PI_{tr} = $\Sigma_m \ PI_{pm}$
- o Harbor : PI_H = $\Sigma_r \ PI_{tr}$

where $CraneCapacity_k$ is the capacity of the kth crane, r is the crane productivity, PI_{bi} is the Performance Indicator of the ith berth, PI_{pm} is the Performance Indicator of the mth pier, PI_{tr} is the Performance Indicator of the rth terminal and PI_H is the Performance Indicator of the harbor. An assumption is made of 24 hours shifts.

b) Gate (container delivering)

The port performance at the gate is measured in terms of:

"TCoM = total number of containers' movements per day, in Twenty-foot Equivalent Units (TEU) for the whole harbor facility"

In this case the total number of containers' movements per day is equal to the sum of total number of containers handled per day (TCoH) in all the container terminals that are connected to the gate through the road system (RDN).

For the assessment of TCoM, in addition to the input parameters reported above, it is necessary to consider the road system that connects each terminal to the harbor's gate, with all its important components (i.e., bridges, overpass, tunnels), and of course the buildings and the storage units inside the harbor that may collapse and block the road system (Pitilakis et al., 2014b). The connectivity between terminals and harbor's gate is based on the *RDN* system analysis.

6.3.1.2 Bulk cargo terminal

a) Terminal (bulk cargo handling)

The terminal performance is measured in terms of:

"*TCaH = total cargo handled (loaded and unloaded) per day, in tones*"

For the harbor, the sum of all container terminals is considered.

For the cargo, the same methodology presented above for the container terminals is used, with the following modifications:

- o The crane productivity (r) is given in tones per hour.
- o Crane Capacity = r*24 tons/day (an assumption is made of 24 hours shifts).

b) Gate (bulk cargo delivering)

The port performance at the gate is measured in terms of:

"*TCaM = total cargo movements per day, in tones for the whole harbor facility*"

In this case, the total cargo movements per day are equal to the sum of total cargo handled per day in all the bulk cargo terminals that are connected to the gate through the road system. The methodology to assess TCaM, and the required additional parameters, is analogous to the ones described above for TCoM.

For the software implementation and the system's class modelling, the reader is referred to Pitilakis et al. (2014b).

6.3.2 Example application for Thessaloniki's Port

Thessaloniki's Port is described in detail in section 3.3. In the followings a pilot application performed within the research program SYNER-G (Pitilakis et al., 2014b) is presented as an example of a systemic analysis of spatially distributed systems under earthquake hazard. The full application of the stress test methodology will be performed in WP6.

For this pilot application, the seismic hazard is based on the shakefield method (Weatherill et al., 2014). Five seismic zones with M_{min}=5.5 M_{max} and =7.5 are selected based on the results of SHARE European research project (Giardini et al., 2013). Adopting the Monte Carlo simulation scheme, 10,000 runs are carried out. In particular, earthquakes are sampled from the seismic zones in terms of localization and magnitude and local intensity values at the sites of vulnerable components are evaluated.

In Thessaloniki's port, soil formations are characterized by very high liquefaction susceptibility, mainly due to loose, saturated, silty-sandy soils that prevail at the area. Previous studies performed in the area (SRMLIFE, 2007) indicate displacement values ranging between 0 and 30 cm for settlements and 0 and 6 cm for lateral spreading for a seismic scenario with 475 years return period. The geotechnical hazard approach proposed in HAZUS is used to sample permanent ground deformations (PGD) due to liquefaction for components whose fragility model requires one (e.g. quaywalls).

Following the methodological framework for the systemic analysis, waterfront structures, cargo handling equipment, power supply system, roadway system and buildings are examined.

Waterfront structures, of 6.5 km length, include concrete gravity quay walls with simple surface foundation and non-anchored components. The majority is block type gravity walls, while the new, actually under construction, part of Thessaloniki's port includes caisson type structures. Backfill soils and rubble foundation include material aggregates with appropriate grain size distributions. Waterfront structures are defined with 17 sides and 24 nodes (pier-nodes). Cargo handling equipment has non-anchored components without back-up power supply. 48 crane-nodes are considered in the analysis.

For the systemic analysis, two Terminals are considered; one container Terminal (6th pier) and one cargo Terminal (piers 2, 3, 4 and 5).

The electric power supply to the cranes is assumed to be provided from a demand node (substation) through non-vulnerable lines. These demand nodes are the distribution substations present inside the port facilities. They can be classified as low-voltage substations, with non-anchored components. Their functionality is determined from connectivity analysis of Thessaloniki's EPN system (Pitilakis et al., 2014b). The geographical representation of Thessaloniki's port waterfronts, cranes and electric power supply system is illustrated in Fig. 6.11. For this application, a pure connectivity analysis of EPN is performed.

The majority of the building and storage facilities are also considered in the analyses. In particular, 88 building structures are allocated in 4 building blocks (BC). The internal roadway network is rather simple with internal roads connecting the port gates to the terminals gates (Fig. 6.12).
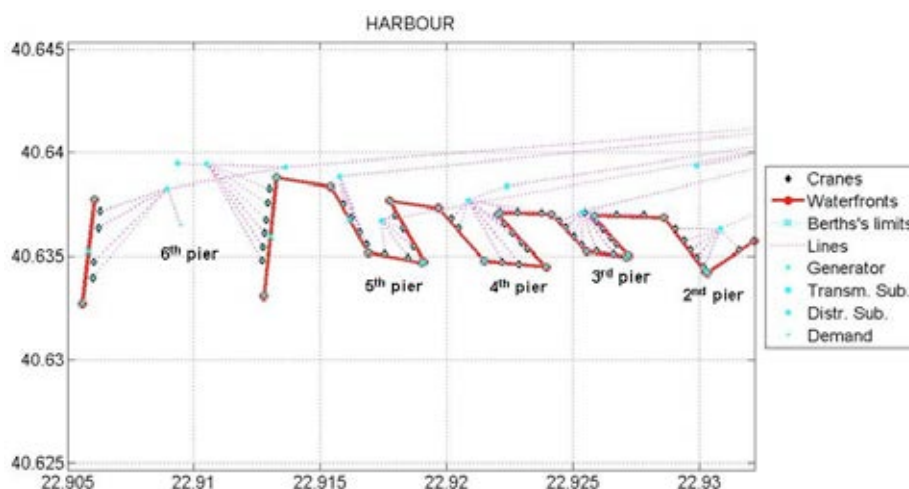
Fig. 6.11 Geographical representation of Thessaloniki's port waterfronts, cranes and electric power supply system.

Fig. 6.12 Internal road network of Thessaloniki's port.

Harbor's class modelling includes 72 nodes (pier-ends and cranes) and 17 edges (gravity type waterfronts). Cranes and waterfronts are vulnerable due to PGD and PGA. In addition, the EPN sub-network within the HBR is considered, consisting of 17 distribution substations (vulnerable components), 74 edges and 48 demand nodes (cranes). This sub-network is supplied by the EPN of the city and supplies electric power to cranes. Fragility models used are provided in Pitilakis et al., 2014b.

As mentioned above, the system's "performance curve" is one of the main results of the analysis performed. The Mean Annual Frequency (MAF) of exceedance values for all PIs are given in terms of normalized performance loss $(1-PI/PI_{max})$[1] in Fig. 6.13 which shows the MAF of exceedance curves ("performance curve") for TCoH and TCaH. For performance loss values below 20% TCaH yields higher values of exceedance frequency, while for performance loss over 20% TCoH yields higher values of exceedance frequency.

The comparison of the estimated performance curves for TCoH and TCoM (Fig. 6.14) shows no difference, meaning that no road closures are observed. We recall here that the only difference between these two PIs is the possibility to deliver containers from the pier to the gate. Thus, the interaction with building collapses and consequent road closures is not important to the port's overall performance in this particular case study.

---

[1] All PIs are normalized to the respective values referring to normal (non-seismic) conditions. These values refer to the maximum capacity of the port, since they are estimated assuming that all cranes are working at their full capacity 24 hours per day.
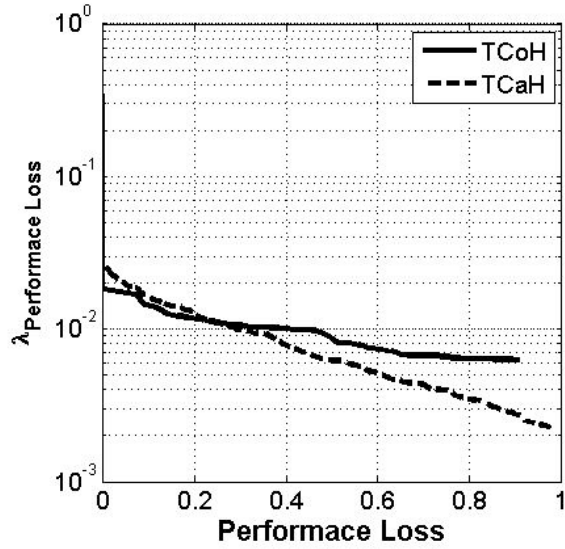
Fig. 6.13 MAF curves for TCoH and TCaH performance loss.
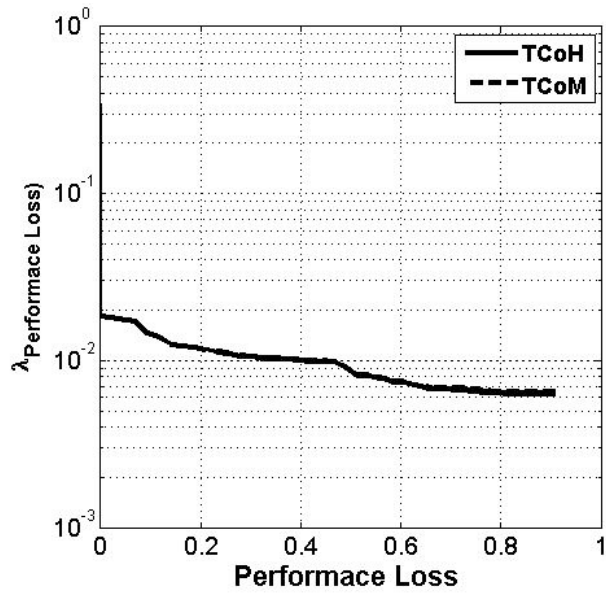
Fig. 6.14 MAF curves for TCoH and TCoM performance loss.

The importance of interactions between components is also pertained from the analysis results. Fig. 6.15 compares the estimated MAF of exceedance curves for TCoH when all and no interactions are taken into consideration in the analysis. Note that, for this particular application the interaction is effective only between EPN and cranes. The effect of this interaction can be very important for performance loss levels over 10% for TCoH. The TCoH performance loss is increased from about 20% to about 50% for $\lambda=0.01$ ($T_R=$ 100 years) when interactions are included in the analysis.
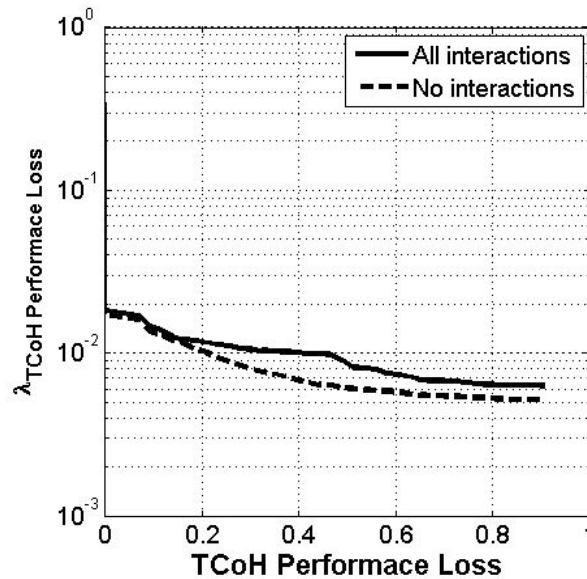
Fig. 6.15 MAF curves for TCoH for Thessaloniki's port, with and without interaction with EPN and building collapses.

Fig. 6.16 and Fig. 6.17 show the level of correlation between the TCaH and the distribution of damages in cranes and non-functionality of electric power distribution substations respectively. In this way the most critical components can be identified in relation with their contribution to the performance loss of the system. All cranes have medium (40-70%) to high (over 70%) levels of correlation, indicating their great importance to the functionality of the overall port system. A higher level of correlation is estimated for the EPN distribution substations, with 40% of the components having values greater than 70%.
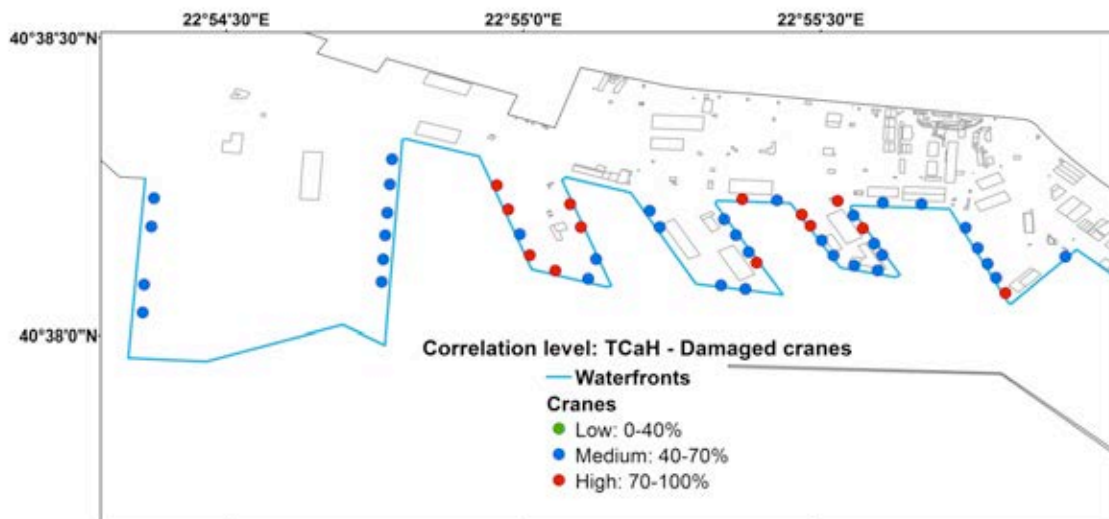
Fig. 6.16 Correlation of damaged cranes to port performance (PI=TCaH).
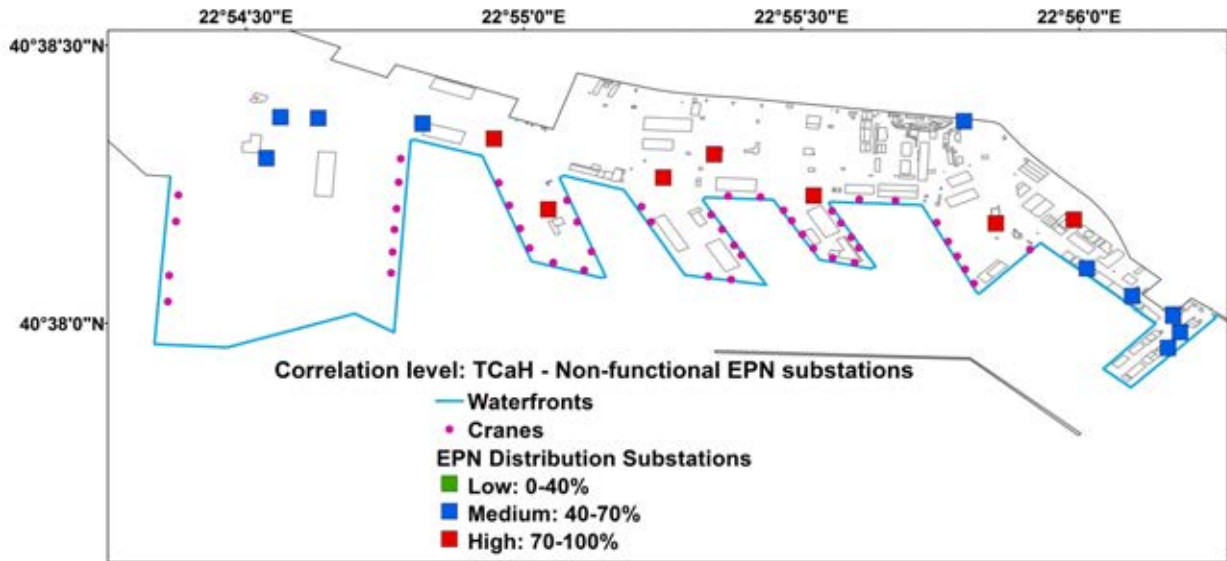
Fig. 6.17 Correlation of non-functional electric power distribution substations to port performance (PI=TCaH).

6.4   LOSS PROPAGATION AND CASCADING EFFECTS

Modern infrastructures exhibit the hallmark properties of so-called complex systems: large number of interacting components, emergent properties difficult to anticipate from the knowledge of single components, adaptability to absorb random disruptions, and highly vulnerable to widespread failure under adverse conditions (Dueñas-Osorio and Vemuru, 2009). The evidence from the literature suggests that cascades can be considered as a direct output of the evolution of complex systems.

For example, the widespread power outage due to the malfunction of an electric power substation, which occurred in the northeastern United States and parts of Canada in August 2003, interrupted the supply of water to several communities, leading to inconvenience and economic losses. Figures 6.18 and 6.19 illustrate how intra and inter dependencies resulted in cascading failures in the 2003 Northeast blackout (NIST, 2015). This example emphasizes how dependencies can significantly magnify the damage in an interacting network system.
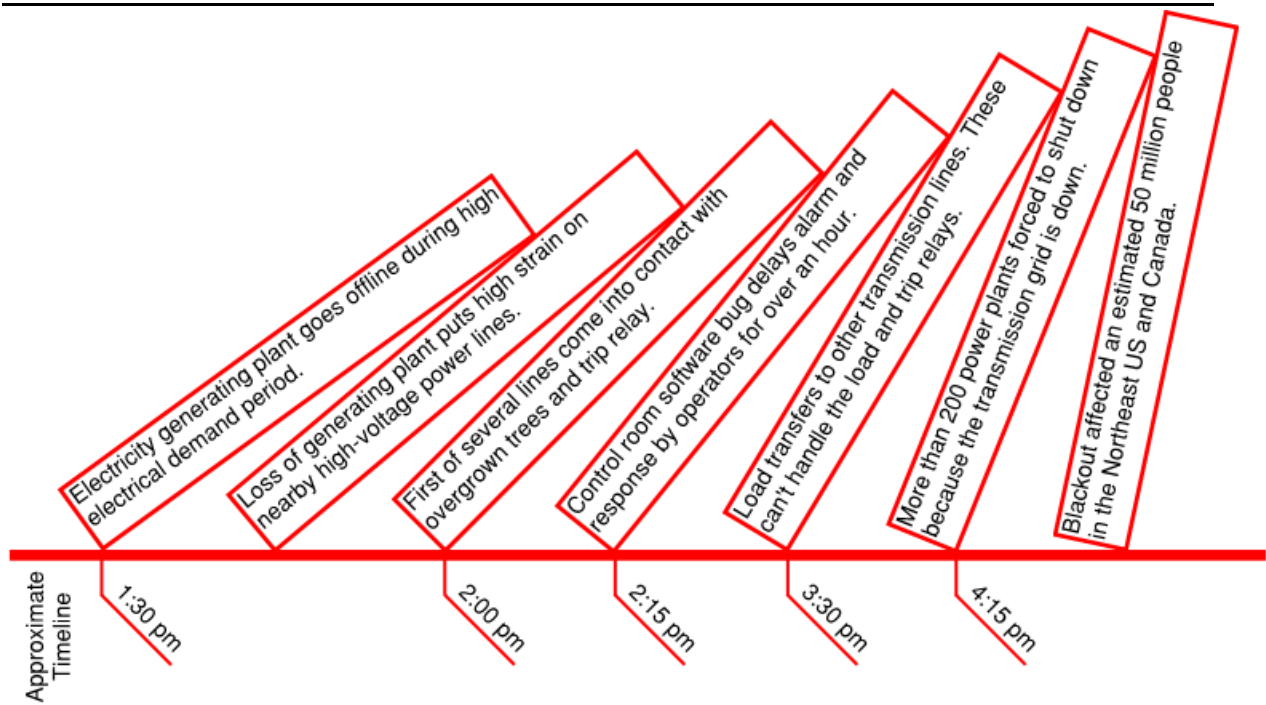
Fig. 6.18 Power system intra-dependence cascading failure in the 2003 Northeast blackout (NIST, 2015).

Fig. 6.19 Inter-dependence cascading failure in the 2003 Northeast blackout (NIST, 2015).

In order to explain a chain-sequence of interconnected failures, the word "cascading" is often associated with the metaphor of toppling dominoes, which may have a bearing on the cause-and-effect relationship that is a feature of most catastrophic events. According to Pescaroli and Alexander (2015) cascades are events that depend, to some extent, on their context, and thus their diffusion is associated with enduring vulnerabilities. They are subject to a process of amplification of damage over time, and this can be distinguished by the presence of subsidiary disasters. The path is non-linear, and branches are visible in terms of sub-disasters (Fig. 6.20).
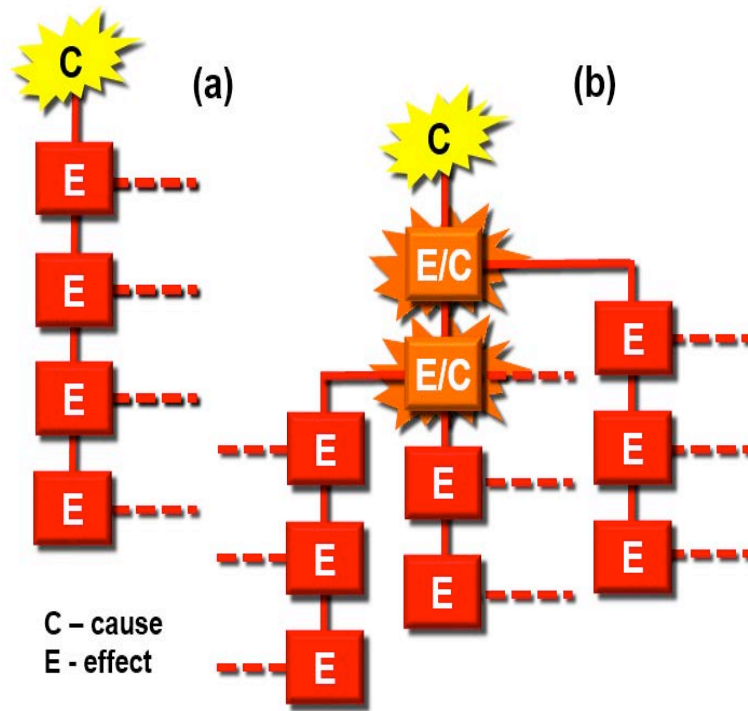
Fig. 6.20 Non-linear path of cascading, including amplification and subsidiary disasters, where C=cause and E=effect (Pescaroli and Alexander, 2015).

Pescaroli and Alexander (2015) provide a coherent definition of cascading effects and disasters": "*Cascading effects are the dynamics present in disasters, in which the impact of a physical event or the development of an initial technological or human failure generates a sequence of events in human subsystems that result in physical, social or economic disruption. Thus, an initial impact can trigger other phenomena that lead to consequences with significant magnitudes. Cascading effects are complex and multi-dimensional and evolve constantly over time. They are associated more with the magnitude of vulnerability than with that of hazards. Low-level hazards can generate broad chain effects if vulnerabilities are widespread in the system or not addressed properly in sub-systems. For these reasons, it is possible to isolate the elements of the chain and see them as individual (subsystem) disasters in their own right. In particular, cascading effects can interact with the secondary or intangible effects of disasters.*" Moreover, "*cascading disasters are extreme events, in which cascading effects increase in progression over time and generate unexpected secondary events of strong impact. These tend to be at least as serious as the original event, and to contribute significantly to the overall duration of the disaster's effects. These subsequent and unanticipated crises can be exacerbated by the failure of physical structures, and the social functions that depend on them, including critical facilities, or by the inadequacy of disaster mitigation strategies, such as evacuation procedures, land use planning and emergency management strategies. Cascading disasters tend to highlight unresolved vulnerabilities in human society. In cascading disasters one or more secondary events can be identified and distinguished from the original source of disaster.*" Cascade hazards are examined in section 6.5.

Similar definitions of cascading effects or failures are given in the literature by several researchers. According to Rosato et al. (2008), a cascading failure is a failure in a system of interconnected parts in which the failure of a part can trigger the failure of successive parts. Such a failure may happen in many types of systems, including power transmission,

computer networking, finance, human bodily systems, and bridges. Cascading failures usually begin when one part of the system fails. When this happens, nearby nodes must then take up the slack for the failed component. This in turn overloads these nodes, causing them to fail as well, prompting additional nodes to fail one after another in a vicious circle.

Adachi (2007) states since the functions of critical infrastructure systems are inter-dependent, the systems sometimes suffer unforeseen functional disruptions. The sequence of such failures leading to widespread outages is referred to as a cascading failure. When the fragility or functionality of a component or facility in a networked infrastructure system or the vulnerability of the system as a whole are considered, the performance of a facility in that networked system may be affected by the functionality of other facilities and connecting elements in interfacing systems.

Some examples of cascading failures after major earthquake events are given below:

Hengchun earthquake (Taiwan, 2006) principally affected Taiwan and involved limited loss of life and injury. Buildings collapsed, fires broke out, telephones ceased to function and the Maanshan Nuclear Power Plant was affected, but the situation was kept under control. In terms of cascading, the key aspect was that the earthquake damaged the submarine communication cables that served much of east and south-east Asia, with profound effects on communications and financial transactions in the area (Smith and Petley, 2009). In other words, it shows that an event of limited impact had amplified effects on damage to a single and localized infrastructure. It shows how the interdependencies of communication can contribute to the escalation of an event from the local to the regional and potentially global levels.

The Tohoku earthquake of 11th March 2011 is considered to be an outstanding example of a cascading disaster. It affected three prefectures in northeast Honshu, the main island of Japan. Although only about 100 people died as a direct result of the earthquake, about 18,000 were killed by the ensuing tsunami. The most enduring consequence of this may be radioactive contamination resulting from tsunami damage to the Fukushima nuclear reactors which, in the short term, caused the evacuation of 200,000 people from the surrounding area. As a result of damage to the global supply chain, vehicle production was affected, not only in Japan, but also in Europe. Fruit, vegetable and meat production from the agricultural areas of Fukushima was contaminated with radioactivity. Dams, utilities and coastal defences were destroyed, which complicated the recovery process. Outmigration compromised the labour force required to reconstruct the 443 sq. km of coastal land and settlements that had been devastated by the tsunami. Worldwide, the political agenda was heavily influenced by a heated public debate on nuclear safety: immediately after the disaster Germany decided to phase out its reactors by 2022, while in Italy more than 94 per cent of electors voted in a referendum to block the creation of new nuclear power plants. In other words, this event shows the occurrence of the probable worst scenario for the interaction between natural and technological hazards. The same physical event generated three different impacts that affected the vulnerability of humans and their geographical spaces, and hence, in effect, three different disasters occurred that amplified the impact while they progressed through time. On the one hand, the primary trigger (the earthquake) caused limited damages and its effects were reduced by preparedness and mitigation measures. On the other hand, it generated a clear chain of cascading effects that increased complexity in time and space due to the interaction of different hazards, threats, and vulnerabilities. In particular, the Fukushima Nuclear Accident was "a profoundly manmade

disaster – that could and should have been foreseen and prevented" (National Diet of Japan, 2012).

Research towards the direction of assessing cascading failures in complex infrastructures systems is limited. In most cases conventional methods used for the reliability assessment of infrastructure systems are adopted in complex systems as well. For example, Adachi (2007) uses a shortest path algorithm in order to compute the impact of cascading failures on serviceability of a networked system.

On the other hand, one can argue that such conventional methods, usually based on path-finding or connectivity-based analysis, can lead to significant underestimation of their expected performance. Connectivity based methods focus on finding enough connected components within the network so that supply and demand can be balanced. However, these methods are unable to capture flow dynamics within the network.

The study presented by Dueñas-Osorio and Vemuru (2009) uses numerical simulation methods to capture the effect of cascading failures on power transmission systems subjected to natural and intentional hazards. A ''cascading susceptibility'' metric is used to quantify the additional disruption to power systems as compared to conventional connectivity or path-based performance assessments. In this research, overloads due to cascading failures are modeled with a tolerance parameter in order to capture the relationship between network component flow capacity and flow demand levels, and monitor the system's propensity to become unstable.

However, all proposed methods are bound to limitations due to availability or not of required data. Different methods can provide more or less accurate estimates of cascading effects based on the available information, which in some cases, especially for extremely complex infrastructures, can be very limited.

6.5   MULTIPLE HAZARDS LOSS ASSESSMENT

Many parts of Europe are potentially under threat from a combination of natural hazards, namely earthquakes, volcanic eruptions, landslides, tsunamis, river floods, wildfires, winter storms, and both fluvial and coastal flooding. In both their occurrence and their consequences, different hazards are often causally related. Classes of interaction include triggered events, cascade effects and the rapid increase in vulnerability during successive hazards.

Scientists, engineers and civil protection and disaster management authorities usually treat these hazards individually. However, they sometimes occur in combination with each other, either at the same time, or when one type of event is triggered by another, e.g. landslides triggered by heavy rains or earthquakes. In addition, due to their physical nature, these natural phenomena cover a range of spatial and temporal scales while at the same time are affected by very different sources of uncertainty.

A literature review of how to define cascades in the context of disasters, incidents and emergencies reveals that the phenomenon considered is associated mainly with events in which a primary threat is followed by a sequence of "secondary hazards" (Mignan et al., 2014b). Conclusively, cascades tend to be dependent on their context and are dynamic systems, in which a branching tree structure originates from a primary event. Each branch can be considered to be event on its own and may be isolated from the main impetus,

resulting in something with its own importance, its own degree of damages, and its own consequences.

Currently, there is no clear definition of "multi-risk", neither in science, nor in practice (COM, 2010; Kappes et al., 2010; Mignan et al., in press). The only definition that exists concerns the requirements for multi-risk, which needs to consider multiple hazards and multiple vulnerabilities (Carpignano et al., 2009; Di Mauro et al., 2007; Marzocchi et al., 2012; Selva, 2013; Mignan et al., 2014b; Komendantova et al., 2014; Liu et al., 2015; Matos et al., 2015). In general, multi–risk represents a comprehensive risk defined from interactions between all possible hazards and vulnerabilities. Jaimes et al. (2015) provide a characteristic visualization of this perspective for a single structure (Fig. 6.21). For the presentation of the multi-risk framework, Komendantova et al. (2014) and Liu et al. (2015) used the concept of the Virtual City (MATRIX project, http://matrix.gpi.kit.edu/), which is illustrated in Fig. 6.22.
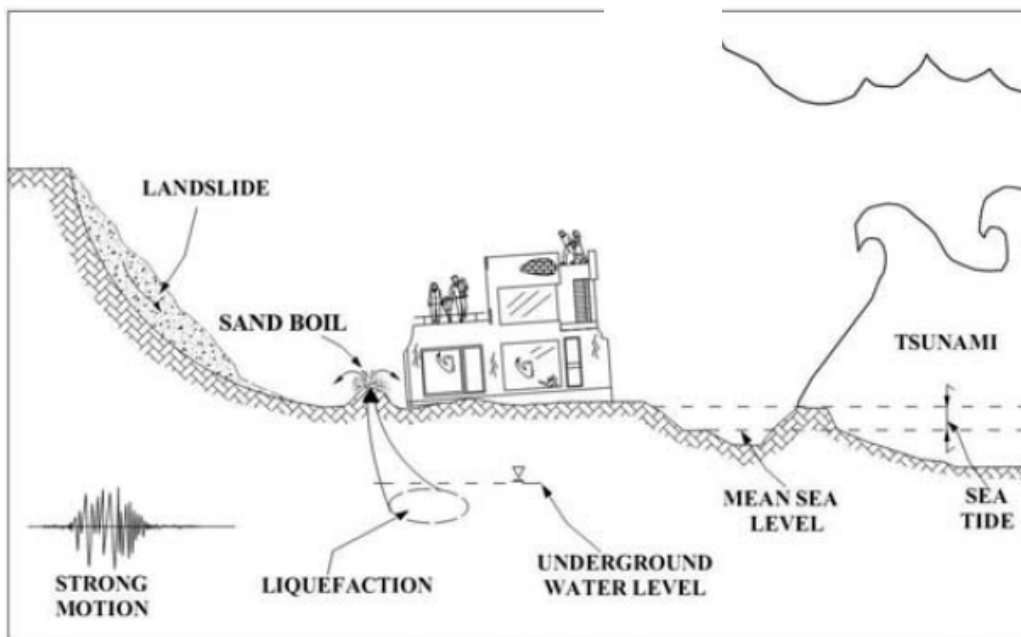
Fig. 6.21 Illustrative example of a house subjected to multiple simultaneous natural hazards induced by a single earthquake where the structure may suffer damage due to the action of strong motion, tsunami, liquefaction, and landslide (Jaimes et al., 2015).
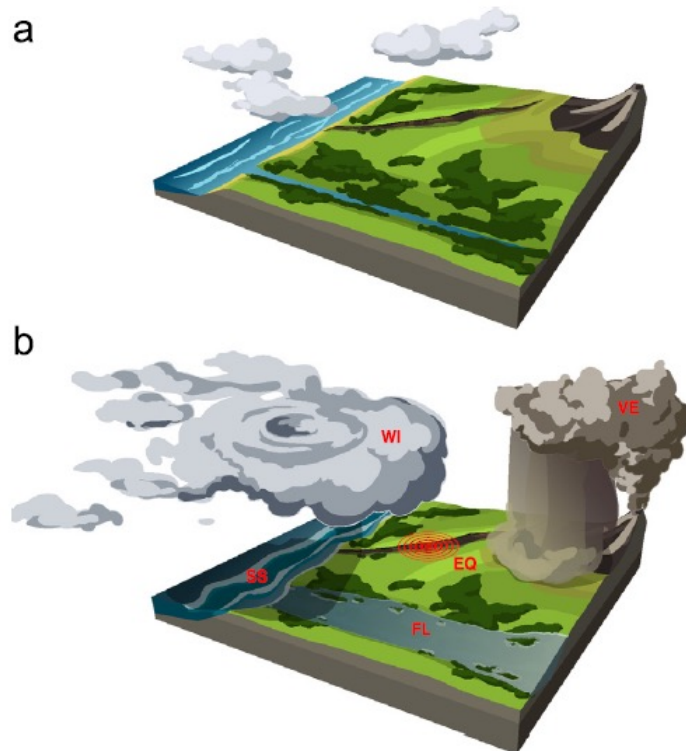
Fig. 6.22 Concept of the virtual city: Artistic representation of a virtual hazardous region. Top: Morphology of the 100 by 100 km region. Bottom: perils considered in this version are earthquakes (EQ), volcanic eruptions (VE), fluvial floods (FL), winds (WI) and sea submersions (SS). The virtual city can be located anywhere within this region (Komendantova et al., 2014); Liu et al., 2015).

So far, the initiatives on multi-risk assessment have developed methodological approaches that consider the multi-risk problem in a partial way, since their analyses basically concentrate on risk assessments for different hazards threatening the same exposed element; therefore, the main emphasis has been towards the definition of procedures for the homogenization of spatial and temporal resolution for the assessment of different hazards. For vulnerability instead, there is a stronger divergence on its definition and assessment methods; considering physical vulnerability, a more or less generalized agreement on the use of vulnerability functions (fragility curves) facilitates the application of such a kind of multi-risk analysis, however, for other kinds of vulnerability assessment (e.g. social, environmental, etc.) it is less clear how to integrate them within a multi-risk framework. In this framework, the final multi-risk index is generally estimated as a simple aggregation of the single indices estimated for different hazards. Other approaches consider a single hazard at a time and multiple exposed elements (e.g. buildings, people, etc.) for the vulnerability, which are combined and weighted according to expert opinion and subjective assignment of weights. Let us note that the recent Generic Multi-Risk (GenMR) framework (Mignan et al., 2014b) combines both hazard interactions and dynamic vulnerability and exposure in a same computational approach with the long-term aim of providing a comprehensive approach to multi-risk. So far, it has been applied in the context of STREST to hazard and system element interactions in the case of hydropower dams (Matos et al., 2015) as well as to earthquake clustering and damage-dependent vulnerability in northern Italy (see Mignan et al., 2015).

There are essentially two ways to approach multi-risk. The first considers the different types of hazards and vulnerabilities of a region and combines the results of various single risk layers into a multi-risk concept (Grünthal et al., 2006; Schmidt et al., 2011). This approach provides an overview of multiple risks, but neglects the interactions between the hazards and vulnerability, e.g. the frequent temporal and spatial interdependencies that often arise between the hazards and other elements of the risk chain. The second one considers the risk arising from multiple hazardous sources and multiple vulnerable elements coinciding in time and space (Di Mauro et al., 2007; Jaimes et al., 2015). In these cases, we refer to conjoint and cascading events. Conjoint events are when a series of parallel adverse events are generated by different sources, for example a windstorm occurring at the same time as an earthquake. Cascading events on the other hand are when an initial event (located inside or outside an area) triggers a subsequent event or series of events, for example an earthquake that then triggers landslides or tsunamis (Marzocchi et al., 2012). The second type explicitly considers spatial and temporal interactions between different hazards and their subsequent risk (Selva, 2013).

The "New Multi-Hazard and Multi-Risk Assessment Methods for Europe (MATRIX: http://matrix.gpi.kit.edu/)" is a recent European research project, which investigated multiple natural hazards and risks in a common theoretical framework. It integrated new methods for multi-type assessment, accounting for risk comparability, cascading hazards, and time-variant vulnerability.

Examples of the main results of the project, which can be used accordingly to tackle multi-hazard problems of geographically distributed CIs include a model of damage accumulation for simple structural systems, consisting a state-dependent modeling of vulnerability when seismic structural performance is affected by damage accumulation (Iervolino et al., 2013a; b) and a generic multi-hazard and multi-risk framework based on the sequential Monte Carlo method to allow for a straightforward and flexible implementation of coinciding and cascading events (Mignan et al., 2014b). The latter helps to better understand the different aspects of multi-hazard and multi-risk, to define a common terminology and to integrate knowledge from various types of models into a same framework and finally to develop a comprehensive model of multi-hazard and multi-risk to improve multi-risk management (including stress tests) (see STREST Deliverable D3.5 "Report on cascading events and multi-hazard probabilistic hazard scenarios", Mignan et al., 2015). In particular, Mignan et al. (2015) demonstrated that potential interactions among the different risks allow emerging new path and/or amplifying the impact of known paths toward the adverse events, which are hidden in any single-risk assessment (see also Mignan et al., 2014b; Matos et al., 2015). Thus, the impact of such potential effects should be evaluated carefully. In the context of the MATRIX project, methods to help practitioners to deal with multi-risk have also been developed, such as a multi-level framework (Liu et al., 2015) and communication tools (Komendantova et al., 2014; Mignan et al., in press).

Developing upon the generic multi-risk (genMR) framework proposed by Mignan et al. (2014) in the scope of the New Multi-Hazard and Multi-Risk Assessment Methods for Europe (MATRIX) project, probabilistic multi-hazard scenarios in which cascades of events emerge from natural hazard correlations was generated within STREST (see STREST Deliverable D3.5 "Report on cascading events and multi-hazard probabilistic hazard scenarios", Mignan et al., 2015). The characteristics of the cascades under various parametric conditions have been investigated and their possible inclusion in stress tests of critical infrastructures was discussed. Focus is made on three types of hazard interactions: (1) "intra-event" earthquake triggering based on concepts of dynamic stress to evaluate the maximum magnitude M_{max} of

cascading fault ruptures; (2) "intra-hazard" earthquake triggering based on the theory of Coulomb stress transfer to evaluate earthquake spatiotemporal clustering; (3) various "inter-hazard" interactions at dams (impact of earthquakes, floods, internal erosion, and malfunctions on dam and foundation, spillway, bottom outlet and hydropower system). Each hazard interaction type is applied to a specific site, respectively: Turkey (CI-B1: Hydrocarbon pipelines), northern Italy (CI-CI: Industrial district), and Switzerland (CI-A2: Dams). Based on this, the GenMR method is suggested to be a part of the stress test methodology developed in the STREST project.

7   Conceptual framework on factors influencing the resilience of CIs

7.1   RESILIENCE OF COMPLEX CRITICAL INFRASTRUCTURES

In this section we provide a state of the art review and a definition for the resilience of complex critical infrastructures. The literature on resilience and critical infrastructures is vast, however, here we aim to reduce the scope and present the elements that are relevant to the problem at hand.

In the system science literature, one of the first recognized uses of the expression "resilience" is attributed to C.S. Holling who, referring to population systems in Holling (1973), indicated by this term "a measure of the persistence of systems and of their abilities to absorb change and disturbance and still maintain the same relationships between populations or state variables". Through the last decades, the concept has been adapted to a number of different scientific contexts ranging from social sciences (Allenby and Fink 2005, Endfield, 2012) to power grids (Chen et al., 2009; Vyatkin et al., 2010; Quyang et al., 2012; Amin and Giacomoni, 2012), distribution networks (Turnquist and Vugrin 2013), transportation networks (Bocchini and Frangopol 2012; Vugrin et al., 2013), robotic systems (Gheorghe et al. 2010), nuclear plants (Villez et al., 2010) computers and computer networks (Trivedi et al., 2009) and building automation(Ji et al., 2011).

Nowadays, one of the most active research areas related to resilience is represented by the study of critical infrastructures, which have been defined as those "whose services are so vital that their incapacity or destruction would have a debilitating impact on the defence or economic security of any state: electric power, gas and oil production and distribution, telecommunications, banking and finance, water supply systems, transportation, health care, emergency and government services, food supply" (European Commission, 2004). The management of critical infrastructures has been receiving much attention in the last few decades. In the 1997 PCCIP Presidential Report (The President's Commission on Critical Infrastructure Protection (PCCIP, 1997) eight US critical infrastructures were identified in the perspective of protection enhancement: telecommunications, electric power systems, natural gas and oil, banking and finance, transportation, water supply systems, government services, emergency services. More recently, the concept of resilience is being explicitly included in some official statements related to critical infrastructures (Obama, 2013).

Analyzing and enforcing the resilience of a critical infrastructure nowadays encompasses the study of the capabilities of a system to resist and react to such events as natural hazards, artificial threats, unscheduled discontinuities of service, outages and a plethora of other context-dependent classes of adverse circumstances and perturbations, which we will refer to generally as disruptive events. However, in the context of the present work the focus is on the restorative capacity of measures of critical infrastructures and more specifically that of big ports.

Since an infrastructure is constituted by an interconnection of assets, the characterization of the complex relationship between the existing linkages and the resulting overall behavior of the system is a natural challenge. This issue arises as a top priority today, as critical infrastructures are becoming increasingly interconnected and interdependent. In this respect,

Bak and Paczuski (1995) introduced the concept of *self-organized criticality*, referring to large-scale systems which reach a highly interactive critical state where even minor perturbations can lead to damages and avalanches of all sizes.

We can notice a tendency to embed them into wide interdependent networks wherein information share (sensor networks, broadband communication and so on) plays a major role. Studies in network dynamics suggest that an assessment of the resilience of the single components is often not representative of the overall resilience of the complex system. These continuously evolving interdependent networks are governed by management actions often expressed by a heterogeneity of deciders who display a melange of cooperativeness and self-interest. Interestingly, in Axelrod et al. (2000) the key processes found in such kind of many-participants clusters are classified as:

- Variation: aimed at reducing the vulnerability at the level of a single participant;

- Interaction: this phenomenon can produce the spread of wrong opinions enforcing inappropriate actions;

- Selection: aiming at the selection of the most successful strategies and at the elimination of those that lead to failure, through learning and adaptive strategies.

Furthermore, referring to critical infrastructures, in Rinaldi et al. (2001) the authors identified the presence of adaptive behaviors, due to their components being influenced by past experiences. This feature is also related to the role of human presence and operation on these infrastructures, which is a subject of further research efforts in itself (Subotic et al. 2007; Oxstrand and Sylvander 2010; Boring and Gertman 2010; Blythe 2012).

The aim of this review is to pave the way for introducing resilience metrics in order to be able in the future to measure the efficiency of measures to improve resilience. This is pertinent for the work to be presented on stress tests for critical infrastructures, as it will be possible to have an indication of the resilience margins of existing critical infrastructures and evaluate resilience improvement measures.

7.2   RESILIENCE DEFINITIONS FOR CRITICAL INFRASTRUCTURES

The literature contains a number of different definitions of the concept of resilience. Some of them, proposed in past contributions, are reported in Manyena (2006), Haimes (2009) as well as in Henry and Emmanuel Ramirez-Marquez (2012), wherein their relevance to different reference contexts is taken into account, broadly ranging from psychology to infrastructure systems, networks and enterprises/organizations. As emphasized in Hollnagel et al. (2007) for our discussion the most interesting interpretation of the concept of resilience should ``cover the ability in difficult conditions to stay within a safe envelope and avoid accidents''. In this perspective, the reaction mechanisms mentioned above include for example restoration of service and reparation strategies, adaptation and learning processes. A definition of resilience which is in accordance with the latter observation was proposed in Vugrin et al. (2010): "given the occurrence of a particular disruptive event (or set of events), the resilience of a system to that event (or set of events) is the ability to reduce effectively both the magnitude and duration of the deviation from targeted system performance levels".

Attention should be paid to distinguish between the concepts of resilience and equilibrium stability. Holling (1973) emphasized that, while stability is typically related to the capability of a system to return to an equilibrium after a disturbance has taken place, resilience reflects

more closely the idea of persistence of a system in spite of adverse events. Along the same direction, in Hollnagel et al. (2007) it is stated that some systems exhibiting strong resilience are tuned "to favour small losses in common events at the expense of large losses when subject to rare or unexpected perturbations, even if the perturbations are infinitesimal". Thus, the two concepts can contrast reciprocally. Similarly, resilience should be kept distinct from fault-tolerance (Isermann, 2005; Albert et al., 2000) in the sense that its study includes a peculiar focus on the ability of a system to recover and possibly assume new operating conditions in response to disruptive events.

Nowadays, we can observe a trend towards a comprehensive interpretation of the concept resilience as a set of concurring factors. A now-classic paradigm in this sense has been proposed in Bruneau et al. (2003) and comprises:

- Robustness (McDaniels et al., 2008): the preservation of functionality under disruptive events;

- Redundancy (Ouyang et al., 2008; Ouyang et al., 2009; Whitson and Ramirez-Marquez, 2009): the presence of elements enabling the preservation of a desired functionality by means of substitution;

- Resourcefulness (Cimellaro et al., 2010): the ability to react and reorganize in the event of a disruption; the last observation has a connection with the definition of resilience as an "intrinsic capacity of a system, community or society predisposed to a shock or stress to adapt and survive by changing its non-essential attributes and rebuilding itself" (Manyena, 2006);

- Rapidity (McDaniels et al., 2008): the timely intervention in order to contain losses and avoid future disruptions.

In the literature, we can find further notions concurring to extending the notion of a system's resilience, including

- Foresight or preparedness (Haimes 2009): the capability of a system to recognize and anticipate the disruptive event;

- Efficiency (Fiksel 2003): performance with modest resource consumption;

- Cohesion (Fiksel 2003): existence of unifying forces or linkages;

- Vulnerability (Kröger and Zio, 2011; Ramirez-Marquez and Rocco 2012): the deterioration of the system's performances/functions due to a disruptive event;

- Recoverability (Ramirez-Marquez and Rocco 2012): the ability of systems to recover after a disruptive damaging event;

- Adaptability (Fiksel, 2003): flexibility to change in response to various pressures;

- Diversity (Fiksel, 2003): especially in complex system, a diversification in the forms and behaviours of the components can positively impact resilience.

For some hints about a possible aggregation of these instances into a comprehensive definition of resilience, see for instance the resilience assessment method proposed in Fisher et al. (2010).

7.2.1 Representation of a single disruptive event and related resilience metrics

When focusing specifically on the phases a system goes through during a disruption-recovery process, according to Vugrin et al. (2010) we can articulate the resilience properties of a system into three indicators:

- Absorptive capacity: the ability to absorb the impacts of perturbations and their consequences with little effort;

- Adaptive capacity: the capability to "change endogenously" during the recovery time through adaptation, exploitation of redundancies, etc.

- Restorative capacity: the aptitude to be repaired easily.

The latter, structured approach to the concept of resilience is matched by one of the typical representations used in the literature on resilient systems to describe a system's service function/performance indicator g(t) along time t across a single disruptive event, see Fig. 7.1.
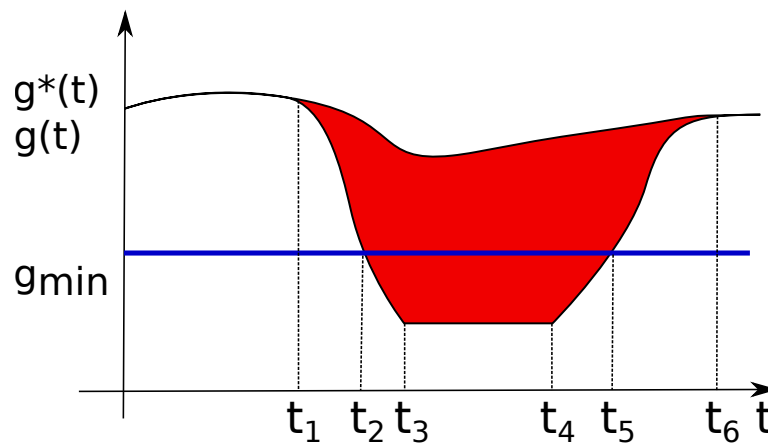
Fig. 7.1 Performance indicator g(t) across a single disruptive event

In this representation, we can identify a fall of operability starting at t_1, when g(t) departs from its reference value $g^*(t)$ due to a disruptive event occurring at t_1. Defining t_3 as the time instant at which g(t) reaches its minimum and assuming g(t) to be non-increasing in $[t_1,t_3]$, we define $t_2=\min_{t \in [t1,t3], \varphi(\tau)=gmin} t$, where g_{min} denotes the minimal operational level of the system. Then we have a time lapse $[t_3,t_4]$ until the start of the restorative action, where function g(t) is represented as a constant for simplicity. To conclude, time instant t_5 represents the return to functionality, while the full recovery is assumed to be reached at t_6, when g(t) reaches (or is suitably close to) $g^*(t)$ (Van Breda, 2001; Henry and Emmanuel Ramirez-Marquez, 2012). The shape assumed by g(t) in both the intervals $[t_1,t_3]$ and $[t_4,t_6]$ can vary according to the nature of the adverse event and of the recovery process. In the limit, the two processes can also be represented as instantaneous. On the other side, in many practical situations the damage process is much more rapid than the repair, see for instance Ouyang et al. (2012). Observe that $g^*(t)$ is a function of time and this feature also allows to account for resilient actions involving some adaptation mechanisms by the system. See also Cimellaro et al. (2010) for discussion about the mathematical definition of the recovery curves and Balchanos (2012), Balchanos et al. (2012) for some complementary definitions related to this representation.

In Bruneau et al. (2003), a framework was provided for measuring the resilience of a system to a specific (seismic) disruptive event whose effects are represented as in Fig. 7.1.

Accordingly, in Vugrin et al. (2009) a basic quantification of the loss of resilience denoted as systemic impact SI is defined as follows:

$$SI = \int_{t1}^{t6} [g*(t) - g(t)] dt$$

(7.1)

Based on this criterion, the authors build up a complex assessment method accounting for three complementary measures of resilience, i.e., reduced failure probabilities, consequences and time to recovery. The method enables to evaluate how resilience varies over time, as well.

More recently, see for instance Vugrin et al. (2009) and Vugrin and Camphouse (2011), the importance of resilience costs to the determination of resilience metrics has been taken into account explicitly, as typically resource availability are a tight bound to the recovery processes in practice. Thus, in the reference the total recovery effort TRE(t) is defined as

$$TRE = \int_{t1}^{t6} [RE(t)] dt$$

(7.2)

where RE(t) represents the instantaneous recovery effort spent into recover functionality. The authors propose to combine the above mentioned merit functions to synthesize suitable recovery actions.

The SI and TRE definitions are not the only ones found in the literature to assess the resilience properties of the system, see also Ouyang and Dueñas-Osorio (2012) for a metric affine to SI. Furthermore they advocate the use of a time-dependent resilience metric, in order to account for resilience improvement strategies and evolution mechanisms and Ouyang et al. (2012) introduce infrastructure resilience metrics incorporating multiple inter-related hazards.

While above we focused on a single disruptive event, the recent literature also addresses the impact assessment of disruptive events taking place over complex systems as critical infrastructures. Therefore, in the next section we deal with interdependence modeling and its implications on the resilience properties of a system.

7.3 MODELLING CRITICAL INFRASTRUCTURES AND INTERDEPENDENCIES FROM A RESILIENCE PERSPECTIVE

According to Vugrin et al. (2010), "given the occurrence of a particular disruptive event (or set of events), the resilience of a system to that event (or set of events) is the ability to reduce effectively both the magnitude and duration of the deviation from targeted system performance levels". In order to address resilience analysis and optimisation, in this paper we represent CIs (either individually, in parts or as conglomerates) as the set N of nodes of a directed graph, and the functional dependencies through the associated edge set $E \subseteq N \times N$, where edge $e_{ij} \subseteq E$ connects source node i to destination node j.

Typically CIs produce, store, transform and/or deliver specific types of resources/services. Correspondingly, we will attach to each node $i \in N$ of the network an inner dynamics associated to a generic operability state variable $x_i(t) \in [0,1]$, where 1 denotes full

operability. Defining $\bar{x}_i(t) \in (0,1)$ as the minimum acceptable value of x_i ensuring service, we also introduce the output variable

$$y_i(t) = \begin{cases} 1, \text{if } x_i(t) \geq \bar{x}_i \\ 0, \text{otherwise} \end{cases}$$
(7.3)

where $y_i(t) = 1$ indicates that node *i* is providing service at time *t*, while $y_i(t) = 0$ the opposite. This output variable is transmitted to all nodes in *N* connected to *i* through its outgoing edges. For simplicity, in this representation we assume that the same output signal is transmitted through all these edges. Correspondingly, as detailed below in this section, the inner dynamics of the nodes in the network will depend on the output variables of the respective source nodes and their combinations.

The latter, binary representation of interdependences is a peculiar feature which we exploit to represent the operability of the different nodes in a serviceability perspective. This allows the introduction of new semantics substituting traditional modelling paradigms based on the exchange of physical quantities (e.g. electricity, water, traffic flow, etc.) between assets and infrastructures.

We assume that the operability state $x_i(t)$ of each node $i \in N$, when exposed to the effects of a critical event affecting the network, depends on the following factors:

- its *static resilience*, which refers to the ability of node *i* to continue its operation despite the event, ensuring $x_i \geq \bar{x}_i$ as long as possible;

- its *dynamic resilience*, describing the ability of node *i* to promptly recover to a serviceable status after the impacting event.

The dynamics of each node $i \in N$ is assumed to be described by one of two possible operational modes, which are associated to the concepts of static and dynamic resilience introduced above:

$$\dot{x}_i(t) = \begin{cases} R_i(x_i(t), f_i), \text{if } u_i(t) = 0 \\ F_i(x_i(t), r_i), \text{if } u_i(t) = 1 \end{cases}$$
(7.4)

Herein, $f_i > 0$ is the static resilience parameter of node *i* and $r_i > 0$ its dynamic resilience parameter. For all $x_i \in [0,1]$, we have $F_i(x_i(t), f_i) \leq 0$, $F_i(0, f_i) = 0$ and $R_i(1, r_i) = 0$. These functions can be suitably specified to describe the failure mode and recovery mode, respectively. The choice of the active mode is determined by $u_i(t)$, which we define as follows:

$$u_i(t) = B_i\left(\{y_j(t) : j \in N, e_{ji} \in E\}\right) \wedge \left(\neg d_i(t)\right)$$
(7.5)

Herein, B_i is a Boolean function having as arguments the outputs of the source nodes associated to the incoming edges of node *i*. Finally, Boolean signal $d_i(t)$ is associated to external perturbations inducing triggering events and causing the activation of the failure mode of node *i*, when active (i.e. while $d_i(t)$=1).

To conclude, observe that the proposed representation is in accordance with the modelling framework proposed in Filippini and Silva (2013). In this paper, anyway, they use the terms

of static and dynamic resilience in order to provide a pragmatic dimension to these concepts: static resilience reflects the prevention measures that a CI operator puts in place in order to absorb the impact of a disruption affecting this node, while dynamic resilience reflects the response measures exploited in order to recover as quickly as possible from a disruptive event.

7.4 RESILIENCE ASSESSMENT IN THE PORT INFRASTRUCTURES OF THESSALONIKI (CI-B3)

In this section we propose an application of the proposed modeling methodology to the resilience assessment in the Port Infrastructures of Thessaloniki (CI-B3). We consider a scenario involving the disruption of electrical substations and cranes. Their dependencies are defined by giving the substation (node) which supplies electric power to each crane.

7.4.1 Description of the components and their interaction

In this subsection we introduce a description of the system's components (substations and cranes) in terms of their grouping, functional interlinking, recovery priorities and recovery resource allocation. Finally, we report a table with the relevant parameters estimated for the different components.

Substations

The importance of substations is classified with values ranging from 1 to 3 (highest to lowest). Since restoration times are in general short (few days) according to expert opinion, the recovery priority should be (for non-functional components) a combination of the classification of importance and the existence or not of back-up power supplying systems (if back-up systems exist the buffering time is greater than 0). The recovery priority could be defined based on Table 7.1. The number of available crews is assumed to be sufficient in order to restore in parallel all components.

Table 7.1 Recovery priorities for substations

Classification of importance	Substation with back-up systems (buffering time > 0)	Substation without back-up systems (buffering time = 0)
1	2nd recovery priority	1st recovery priority
2	3rd recovery priority	1st recovery priority
3	4th recovery priority	2nd recovery priority

Cranes

The importance of cranes is classified with values ranging from 1 to 5. In each of the five groups, there is a minimum number of cranes which should be functional in order to ensure a minimum performance level of the port in the case of an unexpected event and to prevent a total break-down of the port's functionality (in terms of served ships and transported cargos). This is assumed to be equal to the 2/3 of the total number of cranes in each category rounded up (Table 7.2).

Table 7.2 Requirements for minimum number of functional cranes in each crane classification group

Classification group	1	2	3	4	5
Minimum number of required functional cranes	4	4	8	10	2

The port authority has two mobile cranes that can be used in order to substitute any damaged cranes, with the exception of those located in dock 26 (classification of importance = 1).

The recovery priority could be based on the following rules.

- The two mobile cranes will be used in order to ensure the minimum number of functioning cranes (Table 7.2) in the category 2-5 (they cannot be used for cranes with class group=1), starting from the cranes with higher classification values. For example, if class group=2 (with total number of elements equal to 6) has 3 functional cranes, one mobile crane is used here to achieve the requirement for at least 4 functional cranes. The second mobile crane goes to the class group=3 (if there are less than 8 functional cranes).

- The recovery will begin with the non-functional cranes with classification of importance = 1, until the 2/3 of the total number of cranes is functional (in this case 4 cranes should be functional out of 6).

- The restoration continues for the cranes with lower classification values (2-5) until the minimum number of functional cranes is achieved in each of the five groups (2/3 of the total number in each category).

- When all crane classification groups (1-5) have the minimum number of functional cranes, the recovery will proceed to the rest components, starting with those with higher classification values.

- Finally the components that are substituted with the mobile cranes will be restored.

The same assumptions as for the substations could be made here, that is:

- When all components with higher recovery priority are restored, then the ones with lower recovery priority will follow.

- The number of available crews that can work simultaneously is assumed to be equal to 2. This means for example that is 1 crane is non-functional in class group = 1, the second crew will begin restoring one of the non-functional of the next class group that is group 2. On the other hand, if in one class group there are more than 2 cranes that need to be restored (for example 4), the crews will restore the first two, then the next two and then they will proceed with the restoration of the non-functional components of the next class group.

Parameter table

The values for the various fields in the attached table have been defined in collaboration with the port authority (ThPA). In several cases assumptions have been made, as the objective here is to demonstrate the applicability of the proposed modeling methodology to the resilience assessment.

Component ID	Type	Dock	Name	Description	Usage	Long (o)	Lat (o)	Voltage supply	Supplied from node	Component Damage State	D.S.	Component functionality (0/1)	Buffering time (h)	Recovery time (days)	St dev for recovery time (days)	Class of importance
1	Substation	-	Sub2	Closed type, 20.000V	In use	22,930835	40,636309	-	-	Moderate damages	MO	0	0	3	0,6	3
2	Substation	-	Sub3	Closed type, 20.000V	In use	22,925368	40,637145	-	-	Minor damages	MI	1	24	1	0,03	3
3	Substation	-	Sub4	Closed type, 20.000V	In use	22,920858	40,637689	-	-	Minor damages	MI	1	24	1	0,03	3
4	Substation	-	Sub5	Closed type, 20.000V	In use	22,915773	40,638857	-	-	Moderate damages	MO	0	0	3	0,6	3
5	Substation	-	Sub5A	Closed type, 20.000V	In use	22,917408	40,636728	-	-	Moderate damages	MO	0	0	3	0,6	3
6	Substation	-	Sub6	Closed type, 20.000V	In use	22,913632	40,639319	-	-	Moderate damages	MO	0	0	3	0,6	1
7	Substation	-	Sub6A,6B	Closed type, 20.000V	In use	22,909367	40,639505	-	6	Moderate damages	MO	0	24	3	0,6	2
8	Substation	-	Sub6G	Open type, 20.000V	In use	22,909652	40,638162	-	6	Moderate damages	MO	0	0	3	0,6	2
9	Substation	-	Sub6D	Open type, 20.000V	In use	22,909399	40,63578	-	6	Moderate damages	MO	0	0	3	0,6	2
10	Substation	-	Sub6E	Open type, 20.000V	In use	22,908355	40,639366	-	6	Moderate damages	MO	0	0	3	0,6	2
11	Substation	-	Sub-Worksite	Open type, 20.000V	In use	22,910817	40,63482	-	6	Moderate damages	MO	0	0	3	0,6	2
12	Crane	23	0	Mobile electric, non-anchored	In use	22,913643	40,638846	Low voltage	6	Moderate damages	MO	0	0	90	25	3
13	Crane	10	1	Mobile electric, non-anchored	In use	22,92997	40,634893	Low voltage	1	Moderate damages	MO	0	0	90	25	5
14	Crane	10	2	Mobile electric, non-anchored	In use	22,929717	40,635286	Low voltage	1	Moderate damages	MO	0	0	90	25	5
15	Crane	10	3	Mobile electric, non-anchored	In use	22,929257	40,635999	Low voltage	1	Moderate damages	MO	0	0	90	25	5
16	Crane	11	4	Mobile electric, non-anchored	In use	22,926671	40,637032	Low voltage	2	Moderate damages	MO	0	0	90	25	4
17	Crane	23	5	Mobile electric, non-anchored	In use	22,913993	40,638767	Low voltage	6	Moderate damages	MO	0	0	90	25	3
18	Crane	12	6	Mobile electric, non-anchored	In use	22,926495	40,635892	Low voltage	2	Moderate damages	MO	0	0	90	25	4
19	Crane	15	7	Mobile electric, non-anchored	In use	22,922742	40,63714	Low voltage	2	Moderate damages	MO	0	0	90	25	4
20	Crane	14	8	Mobile electric, non-anchored	In use	22,924669	40,636456	Low voltage	2	Moderate damages	MO	0	0	90	25	4
21	Crane	14	9	Mobile electric, non-anchored	In use	22,924417	40,636777	Low voltage	2	Moderate damages	MO	0	0	90	25	4
22	Crane	15	10	Mobile electric, non-anchored	In use	22,923919	40,6371	Low voltage	2	Moderate damages	MO	0	0	90	25	4
23	Crane	15	11	Mobile electric, non-anchored	In use	22,923632	40,63711	Low voltage	2	Moderate damages	MO	0	0	90	25	4
24	Crane	16	12	Mobile electric, non-anchored	In use	22,922464	40,636336	Low voltage	3	Moderate damages	MO	0	0	90	25	4
25	Crane	18	13	Mobile electric, non-anchored	In use	22,921188	40,635368	Low voltage	3	Moderate damages	MO	0	0	90	25	4

26	Crane	23	14	Mobile electric, non-anchored	In use	22,915098	40,638498	Low voltage	6	Moderate damages	MO	0	0	90	25	3
27	Crane	16	15	Mobile electric, non-anchored	In use	22,923405	40,635077	Low voltage	3	Minor damages	MI	1	24	1,5	1,5	4
28	Crane	17	16	Mobile electric, non-anchored	In use	22,923177	40,634588	Medium voltage	3	Minor damages	MI	1	0	1,5	1,5	4
29	Crane	17	17	Mobile electric, non-anchored	In use	22,922154	40,634711	Medium voltage	3	Minor damages	MI	1	0	1,5	1,5	4
30	Crane	18	18	Mobile electric, non-anchored	In use	22,920433	40,636426	Low voltage	3	Minor damages	MI	1	24	1,5	1,5	4
31	Crane	18	19	Mobile electric, non-anchored	In use	22,920191	40,63677	Low voltage	3	Minor damages	MI	1	24	1,5	1,5	4
32	Crane	20	20	Mobile electric, non-anchored	In use	22,918158	40,636597	Low voltage	5	Minor damages	MI	1	0	1,5	1,5	3
33	Crane	20	21	Mobile electric, non-anchored	In use	22,918648	40,635549	Low voltage	5	Moderate damages	MO	0	0	90	25	3
34	Crane	20	22	Mobile electric, non-anchored	In use	22,918893	40,635026	Low voltage	5	Moderate damages	MO	0	0	90	25	3
35	Crane	21	23	Mobile electric, non-anchored	In use	22,918443	40,634896	Low voltage	5	Moderate damages	MO	0	0	90	25	3
36	Crane	22	24	Mobile electric, non-anchored	In use	22,916773	40,635693	Low voltage	4	Moderate damages	MO	0	0	90	25	3
37	Crane	22	25	Mobile electric, non-anchored	In use	22,916548	40,636175	Low voltage	4	Moderate damages	MO	0	0	90	25	3
38	Crane	22	26	Mobile electric, non-anchored	In use	22,916075	40,637193	Low voltage	4	Moderate damages	MO	0	0	90	25	3
39	Crane	22	27	Mobile electric, non-anchored	In use	22,915783	40,637818	Low voltage	4	Moderate damages	MO	0	0	90	25	3
40	Crane	24	28	Mobile electric, non-anchored	In use	22,912965	40,638061	Medium voltage	6	Moderate damages	MO	0	0	90	25	2
41	Crane	24	29	Mobile electric, non-anchored	In use	22,912912	40,637465	Medium voltage	6	Moderate damages	MO	0	0	90	25	2
42	Crane	24	30	Mobile electric, non-anchored	In use	22,912852	40,636829	Medium voltage	6	Moderate damages	MO	0	0	90	25	2
43	Crane	24	31	Mobile electric, non-anchored	In use	22,912745	40,635563	Medium voltage	6	Moderate damages	MO	0	0	90	25	2
44	Crane	24	32	Mobile electric, non-anchored	In use	22,912691	40,634935	Medium voltage	6	Moderate damages	MO	0	0	90	25	2
45	Crane	24	33	Mobile electric, non-anchored	In use	22,912636	40,634253	Medium voltage	6	Moderate damages	MO	0	0	90	25	2
46	Crane	26	34	Container gantry crane, non-anchored	In use	22,906299	40,637047	Medium voltage	7	Moderate damages	MO	0	0	90	25	1
47	Crane	26	35	Container gantry crane, non-anchored	In use	22,90623	40,636412	Medium voltage	7	Moderate damages	MO	0	0	90	25	1
48	Crane	26	36	Container gantry crane, non-anchored	In use	22,906127	40,635585	Medium voltage	7	Moderate damages	MO	0	0	90	25	1
49	Crane	26	37	Container gantry crane, non-anchored	In use	22,905991	40,634493	Medium voltage	7	Moderate damages	MO	0	0	90	25	1
50	Crane	-	38	Transtainer for rail containers, non-anchored	In use	22,90922	40,637026	Medium voltage	7	Moderate damages	MO	0	0	90	25	1
51	Crane	15	39	Mobile electric, non-anchored	In use	22,922416	40,637151	Low voltage	2	Moderate damages	MO	0	24	90	25	4

7.4.2 Simulation results

The proposed modeling framework was applied to the description and simulation of the recovery scenario described in the previous section. To this end, two networks were constructed to represent the recovery process of the substations and the cranes while taking into account sequencing constraints and, where relevant, other constraints related to crew availability and supplementary resources (e.g. the mobile cranes used to cover the service during the restoration phase).

For instance, see in Fig. 7.2 the representation of the network associated to the substations. Observe the ranking of the nodes according to the recovery priority. Sequencing is obtained by imposing jointly the recovery of all substations within a given priority group prior to starting the recovery of the subsequent ones.
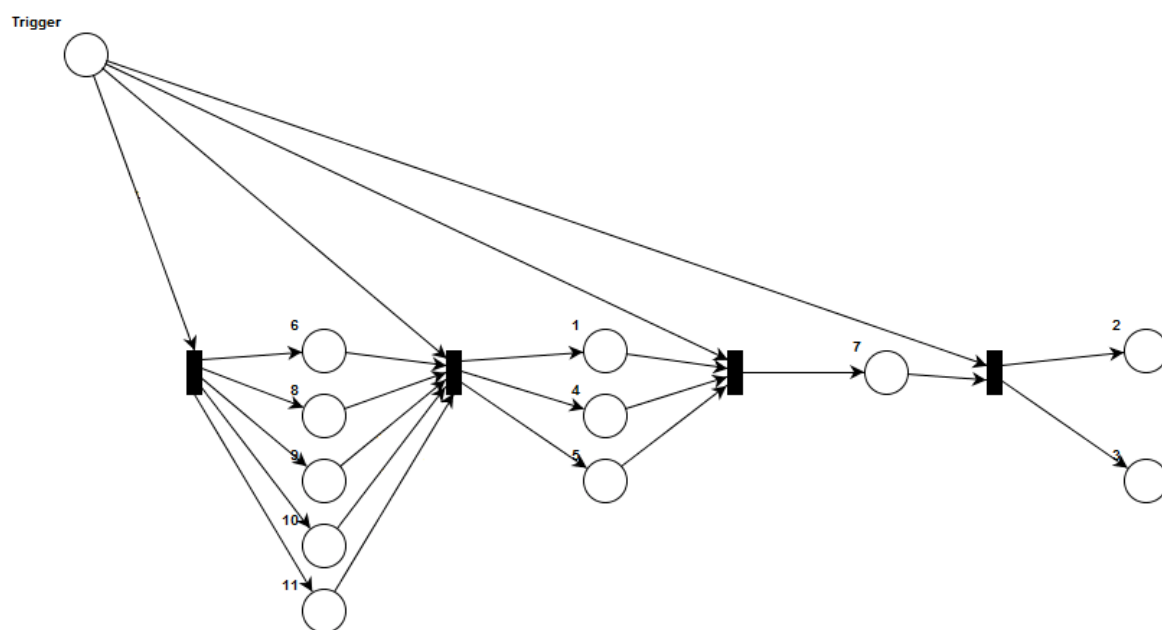
Fig. 7.2 Network used to represent the recovery process of the substations.

The structure of the network associated to the crane recovery process is more complex and it is omitted here for the sake of conciseness. Anyway, in Fig. 7.3, Fig. 7.4 we report the simulation results obtained for the different crane categories, in terms of allocation of substituting mobile cranes and crews. It can be observed that the model correctly represents the sequencing of the resource allocation, which follows the priority principle.
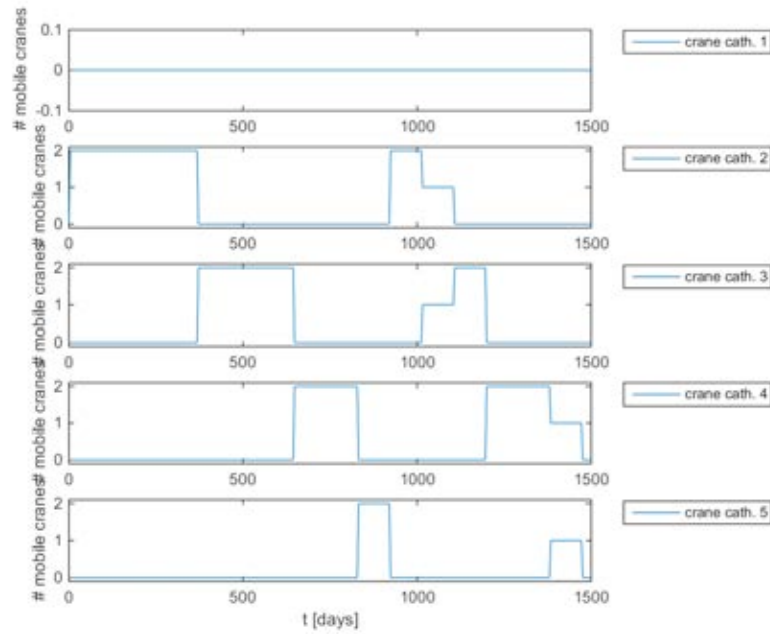
Fig. 7.3 Allocation sequence of mobile cranes by (standard) crane category.
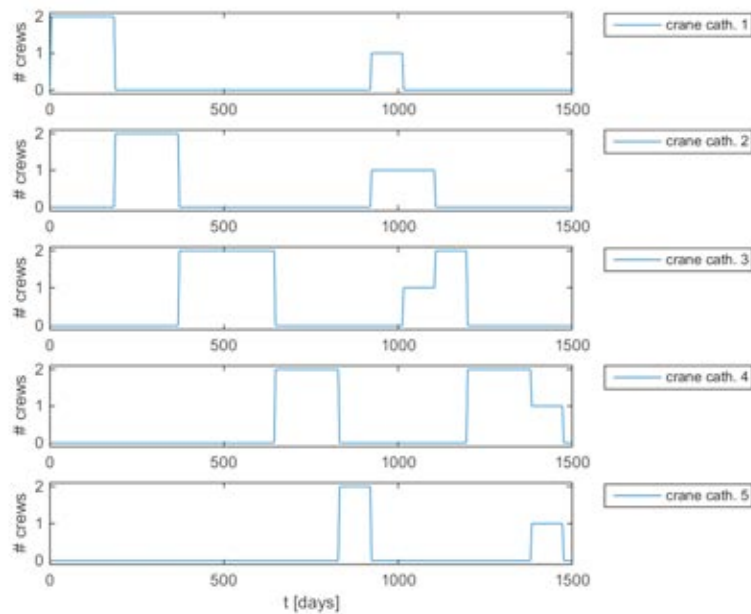
Fig. 7.4 Allocation sequence of crane recovery crews by crane category.

7.4.3 Visualization of the interdependencies analysis into GRRASP

In JRC, we have developed GRRASP (Geospatial Risk and Resilience Assessment Platform) in order to facilitate the analysis of critical infrastructures by stakeholders. GRRASP can be considered as a hybrid tool that brings together the power of GIS systems with mathematical models in order to provide a complete analysis environment with strong visualization and simulation capabilities. The GIS layer is implemented for data entry (where applicable) and for data/analysis results visualization. The computational engine is based on

Matlab® developed modules that have been compiled and can be used in stand-alone mode using the Matlab Runtime Compiler (available for download for free). This approach facilitates the interoperability between mathematical models and web based technologies (Apache, Tomcat, etc.) in order to take advantage of the power of the web.

GRRASP is based on a modular open architecture in order to render the system expandable and scalable to cope with future technology developments (e.g. cloud services). A server-client architecture is implemented in order to facilitate collaboration among users on common projects. Apart from the computational engine, GRRASP is based on a Postgres database where information relevant to models is stored and can be retrieved upon request by the end user. Geoserver, Tomact, Apache and Drupal technologies are used in order to enable to remote users to perform data input, run models and visualize results through their web browser.

GRRASP is developed having in mind the need for a collaborative environment however, data security is a prerequisite. The architecture implemented in GRRASP strongly considers this element. In addition to that, GRRASP allows (for certain modules) uploading proprietary data, invoking the necessary module, visualising the results and then cancelling all uploaded data. This is an additional level of data security that has been implemented in order to cope with the requirements of the CIP analysis community.

Making use of the open architecture of GRRASP we introduced in it our analysis module in order to run the simulations and visualize the results. The added value of this approach is that a stand-alone tool can be developed and disseminated to end users managing ports for assessing their resilience against a gamut of possible threats.

We first report the connection topology of substations and cranes (Fig. 7.5):
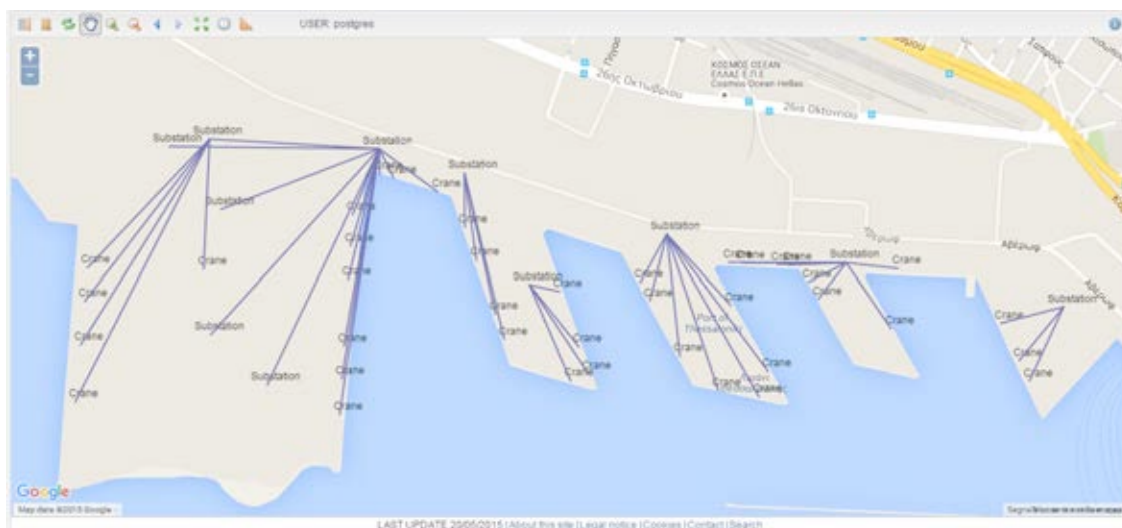
Fig. 7.5 Connection topology (substations to cranes).

The next figures (Fig. 7.6, Fig. 7.7, Fig. 7.8, Fig. 7.9) visualize the status of the network at different time instants, while the system is progressing towards the complete recovery. The size of the circles are related to the internal state of each node, while the colour expresses the operability in terms of the output variable (red if 0, green if 1).
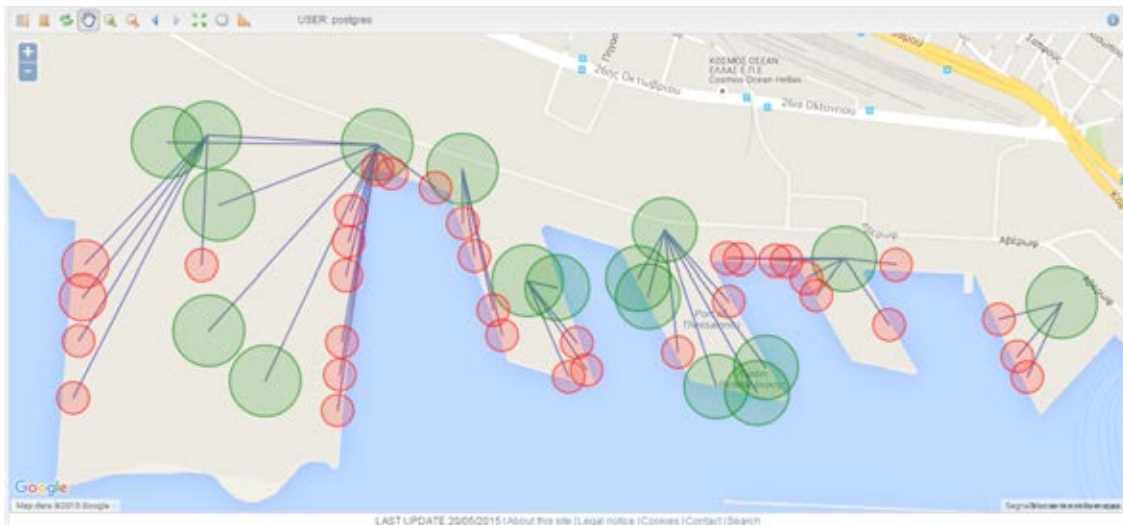
Fig. 7.6 Simulation results (t=8 days).
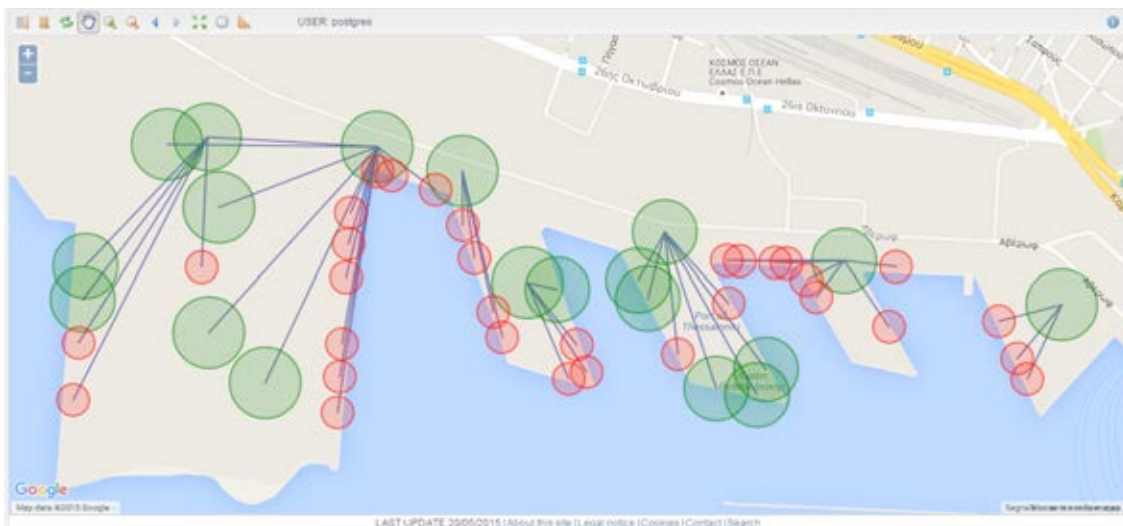
Fig. 7.7 Simulation results (t=25 days).
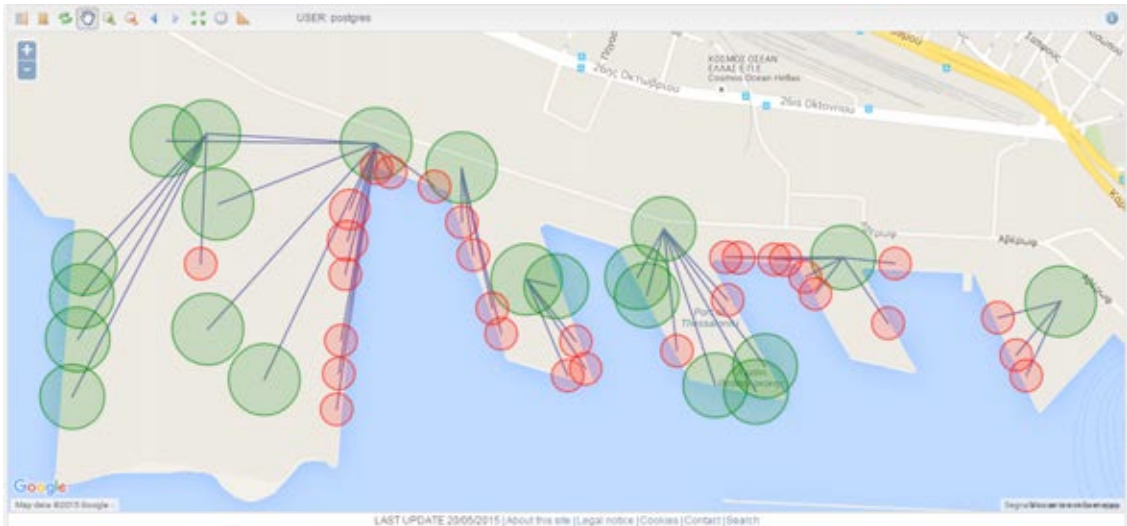
Fig. 7.8 Simulation results (t=51 days).
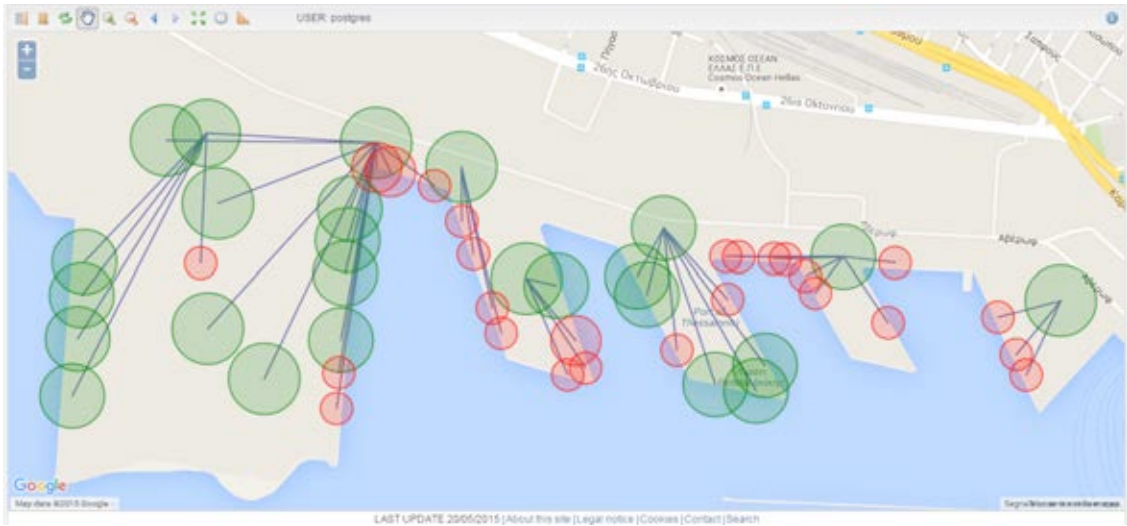
Fig. 7.9 Simulation results (t=102 days).

To conclude, in Fig. 7.10 we report the complete GRRASP interface (with satellite background image) during the same simulation stage as in the latter figure.
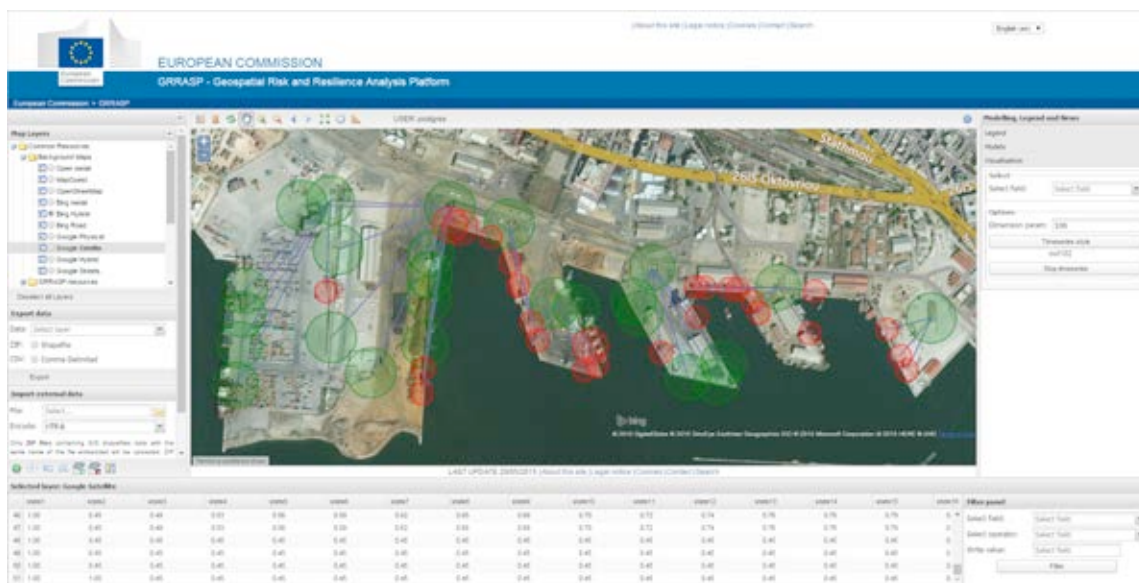
Fig. 7.10 GRRASP satellite background interface during the simulation stage.

8 Treatment of uncertainties

Large uncertainty affects any risk analysis. In the previous sections the treatment of uncertainties has been addressed through the specifications and applications for the three CIs. These were related for example to the spatially correlated ground motion intensities (Shakefield approach), the location and orientation of faults in areal sources, the fault-pipe crossing angle and other structural (e.g. pipeline, quaywalls) and soil parameters. The requirement of explicitly quantifying such uncertainty arises naturally when the analysis is of regulatory concern (SSHAC, 1997). In addition, it is critical in the context of multi-risk analyses (MATRIX: http://matrix.gpi.kit.edu/). Indeed, the comparison among different risks is meaningful only if uncertainty is explicitly quantified, since very different levels of confidence and uncertainty are expected for the different hazards and risks. Therefore, robust results in this comparison can be found only if also the confidence in all the assessments is explicitly quantified.

Two different types of uncertainties are typically defined in the context of hazard/risk analysis for natural hazards: the aleatory uncertainty, related to the intrinsic unpredictability of natural phenomena, and the epistemic uncertainty, related to the lacks in the knowledge about the processes that control the aleatory uncertainty. Even if different scientific positions exist about the possibility in distinguishing between these types of uncertainty (NRC, 1997; Bedford and Cooke, 2001; Jaynes, 2003), it is commonly thought that this distinction is useful in any case from a practical point of view. Indeed, it allows i) distinguishing reducible (through new studies) from not-reducible uncertainties (e.g. Marzocchi et al., 2015), and ii) communicating to decision makers the effective confidence of scientists in hazard/risk results (e.g. Paté-Cornell, 1996).

Aleatory uncertainty is typically quantified in any Probabilistic Hazard/Risk Analysis, as foreseen in Stress Test (ST)-levels 2a, 2b, 3a and 3b (see D3.1, Selva et al., 2015). The explicit quantification of epistemic uncertainty, in the form of a distribution describing "*the center, the body, and the range of technical interpretations that the larger technical community would have if they were to conduct the study*" (SSHAC, 1997), is required for ST-levels 2b, 3a and 3b. This quantification is usually performed only at the hazard level (see discussion in Marzocchi et al., 2015). At risk level, the "mean" hazard is typically assumed and no epistemic uncertainty is quantified. The reason for this is mainly practical. On one side, the application of techniques like Logic Trees is often computationally not affordable (e.g. Field et al., 2005; SYNER-G, 2010-2014). On the other side, multiple scientifically acceptable models for all the steps of the risk analysis are often not available (SYNER-G, 2010-2014). These considerations are particularly true for large geographically extended infrastructures. For example, only few models are available to model spatial correlations of intensity measures in seismic hazard. In addition, only in few cases is possible to have multiple scientifically acceptable fragility models for all the components of one CI (e.g. Pitilakis et al., 2014a), even if large epistemic uncertainty are expected to exist (Selva et al., 2013).

In D3.1 (Selva et al., 2015) of STREST, a specific procedure has been proposed to deal with the treatment of epistemic uncertainty at all ST-levels, namely EU@STREST. This procedure establishes the process through which multiple experts should participate and interact during a ST, in order to track potential scientific divergences within the extended technical community, and quantify the emerging epistemic uncertainty in the context of the

target ST. The goal of EU@STREST is the control of epistemic uncertainty (at ST-levels 2a and 3c), and its quantification (at ST-levels 2b, 3a, 3b) in the form of "*the center, the body, and the range of technical interpretations that the larger technical community would have if they were to conduct the study*" (SSHAC, 1997). EU@STREST is a flexible multiple-expert integration technique (e.g. SSHAC, 2013), in which epistemic uncertainty is treated and quantified by a combination of different techniques (Logic Trees, Bayesian/Ensemble modelling, classical expert elicitations). EU@STREST is designed to be applicable at all the potential ST levels, from single to multi-hazard/risk analyses. In addition, it allows for a large flexibility in its application, within a given well-defined multi-expertise framework.

The application of the EU@STREST process allows overcoming several of the aforementioned issues. In particular, classical expert elicitation techniques (Cook, 1991) are foreseen in EU@STREST to fill potential gaps in modelling procedures. The results of such elicitation experiments consist of the definition of single models that quantify also the relative epistemic uncertainty. Of course, this is not possible for all potential missing models, like for example the lack of alternative approaches in modelling spatial correlation of the seismic intensities. However, it can be applied for missing factors, like specific fragility models for few components.

The propagation and the quantification of epistemic uncertainty through ensemble modelling (Marzocchi et al., 2015) may also drastically reduce the computational effort required by STs. Ensemble modelling, one of the integration techniques proposed for EU@STREST, has been recently proposed to quantify epistemic uncertainty in hazard analyses (Marzocchi and Jordan, 2014; Marzocchi et al., 2015). This technique can be straightforwardly extended also to risk assessments, enabling a full exploration of epistemic uncertainty also in risk analyses. In addition, ensemble modelling can propagate the epistemic uncertainty arising from groups of alternative models, through an alternative tree resembling the logic tree, and/or single Bayesian models (Selva et al., submitted). In this way, ensemble modelling becomes a very flexible tool in which epistemic uncertainty in each step of the assessment (e.g. fragility of one component) may be quantified either through a set of alternative scientifically acceptable model (e.g. a set of alternative applicable fragility models and relative weights), and/or through single Bayesian models set from a group of alternative models (e.g. set of alternative applicable fragility models and relative weights used to set Dirichlet probability distributions, as in Selva et al., 2013), and/or single models directly arising from expert elicitation experiments that quantify epistemic uncertainty on the target model.

These techniques can contribute in quantitatively dealing with both the problem related to the computational effort, and the one related to the lack of multiple models. However, note that this possibility should be evaluated case by case, since it is not always possible to fill all the potential gaps existing for specific case studies. For example, there are cases in which a probabilistic hazard analysis is virtually impossible (for the lack of supporting data and models). Another example is when the missing model is too complicated to be filled through a direct expert elicitation. In such cases, the ST must be strongly simplified, like for example passing from probabilistic to scenario-based analyses (that is, passing from ST-level 3b to ST-level 3c). If this is required, the quantification of uncertainty may be partially, or even completely, neglected.

9   Discussion

The impact of several recent destructive events to critical infrastructures (CIs) highlighted the need to develop guidelines for the performance and consequences assessment of geographically distributed, non-nuclear CIs exposed to multiple natural hazards. The key components of this assessment are: characterization of the CIs including typology of their components and dependencies (intra and inter); identification of hazards to which the CIs components are exposed; vulnerability assessment that evaluates the extent to which a particular components can withstand the impact of the hazard; systemic analysis that measures the performance of the infrastructure under given hazards; resilience assessment that analyses the capabilities of a system to resist and react to such events as natural hazards; treatment of uncertainties that affect the previous assessments.

The report is focused to three representative case studies included in STREST project, CI-B1: Major Hydrocarbon Pipelines in Turkey, CI-B2: Gasunie National Gas Storage and Distribution Network in Holland and CI-B3: Port Infrastructures of Thessaloniki in Greece. Obviously, each system has different peculiarities and needs; therefore the methods and tools explicitly or implicitly composing a set of guidelines for the performance and loss assessment should be adapted or modified according to the specific CI under study.

For geographically distributed CIs, different hazard intensities may be experienced during the same event at the different locations where components are located. Such intensities cannot be assumed independent, since they are caused by the same source event. In addition, different components may be sensible to different intensity measures (IMs) related to the same hazard (e.g. for ground shaking, to PGA and PGV), or to secondary induced hazards (e.g. PGD for geotechnical hazards). Thus, it is necessary to model the potential spatial correlations of the hazard intensities as well as the spatial cross-correlation between different IMs. Monte Carlo based simulation techniques are commonly applied for PSHA of dynamic (e.g. PGA, S_a) and static (e.g. permanent fault displacement) IMs. In particular, the MC-based simulations are incorporated with multi-scale random fields (MSRFs) approach to account for the spatial correlation, near-fault forward directivity and conditional hazard (cross-correlation) in the variation of dynamic intensity measures. Probabilistic permanent fault displacement method proposed herein considers also the uncertainty in the location of the fault segment.

The vulnerability of CIs components is commonly assessed based on fragility functions which are depended on the typology of each component. A comprehensive review of fragility functions for the critical components of the selected CIs has been carried out and new fragility curves have been developed where necessary. Next, the performance of the whole infrastructure should be addressed using appropriate methods and evaluation measures, based on integrated models of critical infrastructure systems which are described in the deliverable. In such models, the complex dependencies between components and/or systems may be accounted for and the systemic performance of the infrastructures (systems or system of systems) and properly evaluated. Furthermore, loss propagation and cascading effects is another characteristic of complex systems; dependencies can significantly magnify the damage in an interacting network system leading to unforeseen systems' disruptions. The sequence of such failures leading to widespread outages is referred to as a cascading

failure. Research towards the direction of assessing cascading failures in complex infrastructures systems is still limited. Different methods can provide more or less accurate estimates of cascading effects based on the available information, which in some cases, especially for extremely complex infrastructures, can be insufficient. The desired level of accuracy dictated by stakeholders and decision makers is the key to define if cascading effects will be studied and to which level of detail.

Multiple hazard loss assessment is another important issue. In both their occurrence and their consequences, different hazards are often causally related. Classes of interaction include triggered events, cascade effects and the increase in vulnerability during successive hazards. Limited work has been done so far towards a uniform risk model of infrastructures considering multiple hazards as well as interactions between them. There are essentially two ways to approach multi-risk (either combination of the results of various single risk layers into a multi-risk concept or considering the risk arising from multiple hazardous sources and multiple vulnerable elements coinciding in time and space). Developing upon the generic multi-risk (genMR) framework developed by Mignan et al. (2014) in the scope of MATRIX project, a probabilistic multi-hazard scenarios in which cascades of events emerge from natural hazard correlations was generated within STREST (see STREST Deliverable D3.5, Mignan et al., 2015).

The concept of resilience is recently included in the risk assessment and management of infrastructures. Many factors and metrics are related to the resilience of interconnected systems and their ability to absorb, adapt or restore the impacts of external changes and stresses due to natural and man-made hazards. In the present report, focus is given in the evaluation of restorative capacity, and an application of the proposed methodology is demonstrated for the port infrastructures in Thessaloniki based on a recovery scenario after an earthquake event. An interface (GRRASP) for computation and visualization of results is introduced.

The proposal of global "all-purposes" guidelines is a quite challenging issue, considering the complexity of interconnected infrastructures, the inherent uncertainties in hazard, vulnerability and risk assessment models as well as the lack of integrated models for the multi-hazard loss assessment and the loss propagation due to cascading effects. However, the work done in STREST and in particular in D4.1-D4.2 is an important step forward providing a general framework of the potential guidelines (stressing also the importance of uncertainties) using as paradigm the representative case studies that are included in STREST project.

References

Adachi, T., Ellingwood, B.R. 2008. Serviceability of earthquake-damaged water systems: Effects of electrical power availability and power backup systems on system vulnerability. *Reliability Engineering and System Safety* 93 (1):78-88.

Adachi, T. 2007. *Impact of Cascading Failures on Performance Assessment of Civil Infrastructure Systems*. Dissertation submitted in partial fulfillment of the requirements of the Ph.D. degree, Georgia Institute of Technology.

Akkar, S., M.A. Sandıkkaya and BÖ. Ay 2014a. Compatible ground-motion prediction equations for damping scaling factors and vertical-to-horizontal spectral amplitude ratios for the broader Europe region. *Bulletin of Earthquake Engineering* 12(1): 517-547

Akkar, S., M.A. Sandıkkaya and BÖ. Ay 2014b. Erratum to: Compatible ground-motion prediction equations for damping scaling factors and vertical-to-horizontal spectral amplitude ratios for the broader Europe region. *Bulletin of Earthquake Engineering* 12(3): 1429-1430.

Akkar, S., M.A. Sandıkkaya and J.J. Bommer 2014c. Empirical ground-motion models for point-and extended-source crustal earthquake scenarios in Europe and the Middle East. *Bulletin of Earthquake Engineering* 12(1): 359–387.

Akkar, S., M.A. Sandıkkaya and J.J. Bommer 2014d. Erratum to: Empirical ground-motion models for point- and extended-source crustal earthquake scenarios in Europe and the Middle East. *Bulletin of Earthquake Engineering* 12(1):389–390.

Albert, R., Jeong, H., Barabási, A.-L., 2000. Error and attack tolerance of complex networks. *Nature* 406(6794):378–382.

Allenby, B., Fink, J., 2005. Toward inherently secure and resilient societies. *Science* 309(5737):1034–1036.

American Lifeline Alliance (ALA) 2005. *Design Guidelines for Seismic Resistant Water Pipeline Installations*. Report FEMA, NIBS and ALA 2005/03. G&E Engineering Systems Inc, 2005.

American Lifelines Alliance (ALA) 2001. *Seismic Fragility Formulations for Water Systems*, Part 1–Guideline, http://www.americanlifelinesalliance.org

Amin, S.M., Giacomoni, A.M., 2012. Smart grid, safe grid. IEEE Power and Energy Magazine, 10(1), pp.33–40.

Applied Technology Council (ATC) 1985. *Earthquake damage evaluation data for California*. Report No. ATC-13, Applied Technology Council, Redwood City, CA.

Applied Technology Council (ATC) 1991. *Seismic vulnerability and impact of disruption of life lines in the conterminous United States*. Report No. ATC-25, Applied Technology Council, Redwood City, CA.

Argyroudis, S, Selva, J, Kakderi, K, Pitilakis, K., 2014. Application to the city of Thessaloniki. In: Pitilakis K, Franchin P, Khazai B, Wenzel H (eds) SYNER-G: Systemic seismic vulnerability and risk assessment of complex urban, utility, lifeline systems and critical facilities. Methodology and applications. *Geotechnical, Geological and Earthquake Engineering* 31, doi: 10.1007/978-94-017-8835-9_7, Springer Netherlands.

Argyroudis, S., Selva J., Gehl, P. Pitilakis K. 2015. Systemic Seismic Risk Assessment of Road Networks Considering Interactions with the Built Environment. *Computer-Aided Civil and Infrastructure Engineering* 30: 524–540.

ASCE 1984. *Guidelines for the Seismic Design of Oil and Gas Pipeline Systems.* Committee on Gas and Liquid Fuel Lifeline, ASCE.

Assatourians, K., G.M. Atkinson 2013. EqHaz: An open‑source probabilistic seismic‑hazard code based on the Monte Carlo simulation approach. *Seismological Research Letters* 84(3): 516-524.

Atkinson, G.M. and K. Goda 2013. Seismic risk analysis and management of civil infrastructure systems: an overview, *Chapter 1. Handbook of Seismic Risk Analysis and Management of Civil Infrastructure Systems*. Cambridge, UK: Woodhead Publishing Ltd.

Axelrod, R.M., Axelrod, R., Cohen, M.D., 2000. Harnessing complexity, Basic Books.

Ayaram, N. and J.W. Baker 2010. Efficient sampling and data reduction techniques for probabilistic seismic lifeline risk assessment. *Earthquake Engineering and Structural Dynamics* 39(10):1109–1131

Aydan, Ö. 2011. *Characteristics of damage to transportation facilities induced by the ground shaking and the tsunami of the 2011 East Japan mega earthquak*e. Tokai University, Ocean Research Institute, Shizuoka, Japan.

Bak, P., Paczuski, M., 1995. Complexity, contingency, and criticality. *Proceedings of the National Academy of Sciences* 92(15): 6689–6696.

Baker, J. and N. Jayaram 2008. Correlation of Spectral Acceleration Values from NGA Ground Motion Models. *Earthquake Spectra* 24(1): 299–317.

Bal, I.E., J.J. Bommer, P.J. Stafford, H. Crowley and R. Pinho 2010. The influence of geographical resolution of urban exposure data in an earthquake loss model for Istanbul. *Earthquake Spectra* 26(3), 619–634.

Balchanos, M., Li, Y., Mavris, D., 2012. Towards a method for assessing resilience of complex dynamical systems. In *5th IEEE International Symposium on Resilient Control Systems*, Salt Lake City, UT, USA. pp. 155–160.

Balchanos, M.G., 2012. A probabilistic technique for the assessment of complex dynamic system resilience.

Bayless, J. and P. Somerville 2013. *Bayless-Somerville Directivity Model.* Report PEER 2013/09. Berkeley, Calif.: Pacific Earthquake Engineering Research Center, University of California.

Salzano, E. et al. 2015. *D4.1 – Guidelines for performance and consequences assessment of single-site, high risk, non-nuclear critical infrastructures exposed to multiple natural hazards*. STREST project: Harmonized approach to stress tests for critical infrastructures against natural hazards.

Bedford, T. and R. Cooke 2001. *Probabilistic risk analysis: foundations and methods*. Cambridge University Press.

Blythe, J., 2012. A dual-process cognitive model for testing resilient control systems. In *5th IEEE International Symposium on Resilient Control Systems*, Salt Lake City, UT, USA. pp. 8–12.

Bocchini, P., Frangopol, D.M., 2012. Restoration of Bridge Networks after an Earthquake: Multicriteria Intervention Optimization. *Earthquake Spectra* 28(2):426–455.

Boore, D.M., J.F. Gibbs, W.B. Joyner, J.C. Tinsley, D.J. Ponti 2003. Estimated ground motion from the 1994 Northridge, California, earthquake at the site of the Interstate 10 and La Cienega Boulevard bridge collapse, West Los Angeles, California. Bulletin of the Seismological Society of America 93(6): 2737–2751.

Boring, R.L., Gertman, D.I., 2010. A resilience-reliability crosswalk. In Proceedings of the 3rd IEEE International Symposium on Resilient Control Systems, Idaho Falls, ID, USA. pp. 129–134.

Bradley, B.A. 2011. Empirical correlation of PGA, spectral accelerations and spectrum intensities from active shallow crustal earthquakes. *Earthquake Engineering and Structural Dynamics* 40(15):1707–1721.

Bradley, B.A. 2012. Empirical correlations between cumulative absolute velocity and amplitude-based ground motion intensity measures. *Earthquake Spectra* 28(1): 17–35.

Bradley, B.A. 2012. Empirical Correlations between Peak Ground Velocity and Spectrum-Based Intensity Measures. *Earthquake Spectra* 28(1): 37–54.

Bruneau, M. et al., 2003. A framework to quantitatively assess and enhance the seismic resilience of communities. *Earthquake Spectra* 19(4):733–752.

Calvi, G. M., R. Pinho, G. Magenes, J.J. Bommer, L.F. Restrepo-Velez and H. Crowley 2006. Development of seismic vulnerability assessment methodologies over the past 30 years. *J Earthq Technol* 43(3): 75–104.

Carpignano, A., E. Golia, C. Di Mauro, S. Bouchon and J - P. Nordvik 2009. A methodological approach for the definition of multi-risk maps at regional level: first application. *Journal of Risk Research* 12(3-4): 513-534.

Cavalieri, F., P. Franchin, P. Gehl and B. Khazai 2012. Quantitative assessment of social losses based on physical damage and interaction with infrastructural systems. *Earthquake Engineering and Structural Dynamics* 41(11):1569–89.

CEN 2006. *European Committee for Standardisation*. Eurocode 8: design of structures for earthquake resistance. Part 4: deals with silos, tanks and pipelines, prEN 1998-4.

Chen, M. et al., 2009. Hierarchical utilization control for real-time and resilient power grid. In 21st IEEE Euromicro Conference on Real-Time Systems, Dublin, Ireland. pp. 66–75.

Chen, Q, A. Seifried, J.E. Andrade and J.W. Baker 2012. Characterization of random fields and their impact on the mechanics of geosystems at multiple scales. International *Journal for Numerical and Analytical Methods in Geomechanics* 36(2):140–165.

Cheng, Y., A. Lucchini and F. Mollaioli 2015. Correlation of elastic input energy equivalent velocity spectral values for ground motions. *Earthquakes and Structures* 8(5): 957-976.

Chioccarelli, E., S. Esposito, I. Iervolino 2012. Implementing conditional hazard for earthquake engineering practice: the Italian example. *In Proceedings of the 15th World Conference on Earthquake Engineering*, Lisbon, Portugal

Chiou, B.S.J. and P. Spudich 2013. *The Chiou and Spudich Directivity Predictor DPP*. Report PEER 2013/09. Berkeley, Calif.: Pacific Earthquake Engineering Research Center, University of California.

Chiou, J.-S., C.-H. Chiang, H.-H. Yang and S.-Y. Hsu 2011. Developing fragility curves for a pile-supported wharf. *Soil Dynamics and Earthq Engng* 31: 830–840.

Cimellaro, G.P. 2013. Correlation in spectral accelerations for earthquakes in Europe. *Earthquake Engineering and Structural Dynamics* 42(4): 623-633.

Cimellaro, G.P., Reinhorn, A.M., Bruneau, M., 2010. Framework for analytical quantification of disaster resilience. *Engineering Structures* 32(11):3639–3649.

COM 2010, 1626 final. *A Community approach on the prevention of natural and man-made disasters Commission Staff Working Paper*. Risk Assessment and Mapping Guideline for Disaster Management, Brussels.

Cook, R. 1991. *Experts in Uncertainty: Opinion and Subjective Probability in Science*. Oxford Univ. Press, New York.

Cornell, C. and H. Krawinkler 2000. *Progress and challenges in seismic performance assessmen*t. PEER News 2000, 3(2).

Cornell, C.A. 1968. Engineering seismic risk analysis. *Bulletin of the Seismological Society of America* 58(5): 1583-1606.

Costa, A., F. Dell'Erba, M.A. Di Vito, R. Isaia, G. Macedonio, G. Orsi, and T. Pfeiffer 2009. Tephra fallout hazard assessment at the Campi Flegrei caldera (Italy). *Bull. Volcanol.* 71:259–273, doi:10.1007/s00445-008-0220-3.

Crowley, H. and J.J. Bommer 2006. Modelling seismic hazard in earthquake loss models with spatially distributed exposure. *Bulletin of Earthquake Engineering* 4(3): 249-273.

Cubrinovski, M., R.A. Green, J. Allen, S.A. Ashford, E. Bowman, B.A. Bradley, B. Cox, T. Hutchinson, E. Kavazanjian, R. Orense, T. O'Rourke, M. Pender, M. Quigley and L. Wotherspoon 2010. Geotechnical reconnaissance of the 2010 Darfield (Canterbury) earthquake. *Bulletin of the New Zealand Society for Earthquake Engineering*, 43(4): 243–320.

Datta, T. K. 1999. Seismic response of buried pipelines: a state-of-the-art review. *Nuclear Engineering and Design* 192(2-3): 271-284.

Di Mauro, D., S. Lepidi, M. Di Persio, A. Meloni and P. Palangio 2007. Update on monitoring of magnetic and electromagnetic tectonic signals in Central Italy. *Annals of Geophysics* 50(1): 51-60.

Dost, B., Caccavale, M., van Eck, T., Kraaijpoel, D. 2013. Report on the expected PGV and PGA values for induced earthquakes in the Groningen area. Report KNMI (Koninklijk Nederlands Meteorologisch Instituut), Utrecht, The Netherlands.

Dueñas-Osorio, L. and S.M. Vemuru 2009. Cascading Failures in Complex Infrastructure Systems. *Structural Safety* 31:157–167.

Durukal, E. and Erdik M., 2008. Physical and Economic Losses Sustained by the Industry in the 1999 Kocaeli Earthquake, *Nat. Hazards* 46:153–178, DOI 10.1007/s11069-008-9218-6.

Eguchi, R. T. 1983. *Seismic vulnerability models for underground pipes.* Proc., Earthquake Behavior and Safety of Oil and Gas Storage Facilities, Buried Pipelines and Equipment, ASME, New York, 368–373.

Eguchi, R. T. 1991. Seismic hazard input for lifeline systems. *Struct. Safety* 10:193–198.

Eidinger, J. 1998. *Lifelines, water distribution systems in the Loma Prieta, California, earthquake of October 17, 1989.* Performance of the built environment e Lifelines. US Geological Survey Professional Paper 1552-A: 63-80.

Eidinger, J., and E. Avila 1999. *Guidelines for the seismic upgrade of water transmission facilities.* TCLEE Monograph, 15.

Endfield, G.H., 2012. The resilience and adaptive capacity of social-environmental systems in colonial Mexico. *Proceedings of the National Academy of Sciences* 109(10):3676–3681.

Esposito, S. and I. Iervolino 2011. PGA and PGV spatial correlation models based on European multievent datasets. *Bulletin of the Seismological Society of America* 101(5): 2532–2541.

Esposito, S. 2001. Systemic seismic analysis of gas distribution networks. *Ph.D. thesis*, University of Naples Federico II, Italy, Advisor: I. Iervolino. Available at: http://wpage.unina.it/iuniervo/

Esposito, S., I. Iervolino, A. d'Onofrio, A. Santo 2015. Simulation-Based Seismic Risk Assessment of Gas Distribution Networks. *Computer-Aided Civil and Infrastructure Engineering* 30(7): 508–523.

European Commission, 2004. COM (2004) 702 final Communication from the Commission to the Council and the European Parliament "Critical Infrastructure Protection in the fight against terrorism". Available at: http://europa.eu.int/eur-lex/lex/LexUriServ/site/en/com/2004/com2004_0702en01.pdf.

FEMA (Federal Emergency Management Agency) 2004. *Multi-hazard loss estimation methodology-earthquake model*: HAZUS MR4 technical manual, Washington DC.

Field, E.H., N. Gupta, V. Gupta, M. Blanpied, P. Maechling and T.H. Jordan 2005. Hazard calculations for the WGCEP-2002 earthquake forecast using OpenSHA and distributed object technologies. *Seismol. Res. Lett.* 76:161–167.

Fiksel, J., 2003. Designing resilient, sustainable systems. Environmental science & technology, 37(23), pp.5330–5339.

Filippini, R., Silva, A., 2013. A modeling framework for the resilience analysis of networked systems-of-systems based on functional dependencies. Reliability Engineering & System Safety, (0), p.-. Available at: http://www.sciencedirect.com/science/article/pii/S0951832013002676.

Fisher, R.E. et al., 2010. Constructing a resilience index for the enhanced critical in Frastructure Protection Program,

Fotopoulou, S. and K. Pitilakis 2013. Vulnerability assessment of reinforced concrete buildings subjected to seismically triggered slow-moving earth slides. *Landslides* 10:563–582. doi: 101007/ s10346-012-0345-5

Gehl, P., Desramaut, N., Arnaud Réveillère, A., Modaressi, H. 2014. Fragility Functions of Gas and Oil Networks. In K. Pitilakis et al. (eds.), SYNER-G: Typology Definition and Fragility Functions for Physical Elements at Seismic Risk, *Geotechnical, Geological and Earthquake Engineering* 27, DOI 10.1007/978-94-007-7872-6_7, Springer , Netherlands, pp. 197-218.

Geist, E.L. and T. Parsons 2006. Probabilistic analysis of tsunami hazards. *Nat. Hazards* 37:277–314.

Gheorghe, V. et al., 2010. Rolling robot with radial extending legs. In *3rd IEEE International Symposium on Resilient Control Systems*, Idaho Falls, ID, USA. pp. 107–112.

Giardini, D. et al. *Seismic Hazard Harmonization in Europe (SHARE)*. Online Data Resource, http://portal.share-eu.org:8080/jetspeed/portal/, doi: 10.12686/SED-00000001-SHARE, 2013.

Goda, K. and G.M. Atkinson 2009. Probabilistic characterization of spatially correlated response spectra for earthquakes in Japan. *Bulletin of the Seismological Society of America* 99(5): 3003-3020.

Goda, K. and H.P. Hong 2008. Spatial Correlation of Peak Ground Motions and Response Spectra. *Bulletin of the Seismological Society of America* 98(1): 354–365.

Grünthal, G., A.H. Thieken, J. Schwarz, K.S. Radtke, A. Smolka and B. Merz 2006. Comparative risk assessment for the city of Cologne - storms, foods, earthquakes. *Natural Hazards* 38(1-2): 22-44.

Haimes, Y.Y., 2009. On the definition of resilience in systems. *Risk Analysis* 29(4):498–501.

Helmholt, K., Courage, W., 2013. Risk management in large scale underground infrastructures. *7th Annual IEEE International Systems Conference, SysCon 2013*, 15-18 April 2013, Orlando, FL.

Henry, D., Emmanuel Ramirez-Marquez, J., 2012. Generic metrics and quantitative approaches for system resilience as a function of time. *Reliability Engineering & System Safety* 99:114–122.

Holling, C. S. 1973. Resilience and stability of ecological systems *Annual review of ecology and systematics*, vol. 4, pp. 1–23, 1973.

Hollnagel, E., D.D. Woods, and N. Leveson. 2007. Resilience Engineering (Ebk) Concepts and Precepts, Ashgate Publishing.

Honegger, D. G. and R. T. Eguchi. 1992. *Determination of the relative vulnerabilities to seismic damage for San Diego County Water Authority (SDWCA).* Water transmission pipelines.

Ichii, K. 2003. *Application of performance-based seismic design concept for caisson-type quay walls*. Ph.D. dissertation, Kyoto University.

Ichii, K. 2004. Fragility curves for gravity-type quay walls based on effective stress analyses. In *13th WCEE*, Vancouver, BC.

Idriss, I.M., Boulangier, R.W. 2008. Soil Liquefaction during earthquake, EERI monograph MNO-12 on earthquake engineering. Earthquake Engineering Research Institute, Oakland (CA), USA.

Iervolino, I., M. Giorgio and E. Chioccarelli 2013a. Closed-form aftershock reliability of damage-cumulating elastic-perfectly-plastic systems. *Earthquake Engng Struct. Dyn.*, 43(4): 613-625. doi: 10.1002/eqe.2363.

Iervolino, I., M. Giorgio and E. Chioccarelli 2013b. Gamma degradation models for earthquake-resistant structures. *Structural Safety* 45: 48-58.

Iervolino, I., M. Giorgio, C. Galassoand G. Manfredi 2010. Conditional hazard maps for secondary intensity measures. *Bulletin of the Seismological Society of America* 100(6): 3312–3319.

Iervolino, I., E. Chioccarelli and G. Baltzopoulos 2015. *D3.3 – Report on near-source hazard assessment and definition of reference scenarios for stress tests*. STREST project: Harmonized approach to stress tests for critical infrastructures against natural hazards.

IITK-GSDMA 2007. *Guidelines for seismic design of buried pipelines*. Kanpur, India: Indian Institute of Technology.

Isermann, R., 2005. Model-based fault-detection and diagnosis--status and applications. *Annual Reviews in Control* 29(1):71–85.

Jaimes, M., E. Reinoso and L. Esteva 2015. Risk analysis for structures exposed to several multi-hazard sources, *Journal of Earthquake Engng*, 19(2):297-312, DOI: 10.1080/13632469.2014.962673

Japan Society of Civil Engineering 2000. *Earthquake Resistant Design Codes in Japan*. Chapter 6: recommended practices for earthquake resistant design of gas pipelines.

Jayaram, N. and J.W. Baker 2009. Correlation model of spatially distributed ground motion intensities. *Earthquake Engineering and Structural Dynamics* 38(15): 1687–1708.

Jaynes, E.T. 2003. *Probability theory: the logic of Science*. Cambridge Univ. Press, New York.

Ji, K. et al., 2011. Prognostics enabled resilient control for model-based building automation systems. In Proceedings of the 12th Conference of International Building Performance Simulation Association. pp. 286–293.

Kakderi, K. and K. Pitilakis 2010. Seismic analysis and fragility curves of gravity waterfront structures. In *Fifth international conference on recent advances in geotechnical earthquake engineering and soil dynamics and symposium in Honour of Prof. I. M. Idriss*, Paper 6.04a.

Kappes, M., M. Keiler and T. Glade 2010. *From single- to multi-hazard risk analyses: a concept addressing emerging challenges*. In Malet, J.-P., Glade, T., Casagli, N. (Eds.), *Mountain Risks: Bringing Science to Society*. Proceedings of the International Conference, Florence. CERG Editions, Strasbourg, 351-356.

Karamitros, D. K., G. D. Bouckovalas and G. P. Kouretzis 2007. Stress analysis of buried steel pipelines at strike-slip fault crossings. *Soil Dyn Earthq Eng* 27(3): 200-211.

Karamitros, D. K., G. D. Bouckovalas, G. P. Kouretzis and V. Gkesouli 2011. An analytical method for strength verification of buried steel pipelines at normal fault crossings. *Soil Dyn Earthq Eng* 31(11): 1452-1464.

Katayama, T., K. Kubo, and N. Sato 1975. *Earthquake Damage to Water and Gas Distribution Systems.* Proceedings of the U.S. National Conference on Earthquake Engineering, Oakland, California, EERI, pp. 396-405.

Ko, Y.-Y., H.-H. Yang and C.-H. Chen 2010. Seismic fragility analysis for sheet pile wharves – case study of the Hualien harbor in Taiwan. In *Fifth international conference on recent advances in geotechnical earthquake engineering and soil dynamics and symposium in Honor of Prof. I.M. Idriss*, 6.05a

Komendantova, N., R. Mrzyglocki, A. Mignan, B. Khazai, F. Wenzel, A. Patt and K. Fleming 2014. Multi-hazard and multi-risk decision-support tools as a part of participatory risk governance: Feedback from civil protection stakeholders. *International J. Disaster Risk Reduction*, 8:50-67, doi: 10.1016/j.ijdrr.2013.12.006.

Kosbab, B.D. 2010. *Seismic performance evaluation of port container cranes allowed to uplift*. PhD thesis, School of Civil and Environmental Engineering, Georgia Institute of Technology.

Kröger, W., Zio, E., 2011. Vulnerable systems, Springer Editions.

Lekkas, E., E. Andreadakis, V. Alexoudi, E. Kapourani and I. Kostaki 2011. *The Mw=9.0 Tohoku Japan Earthquake (March 11, 2011) Tsunami Impact on Structures and Infrastructure*. Environmental Geosciences and Engineering Survey for Territory Protection and Population Safety (EngeoPro) International conference, Moscow, 97-103.

Liu, Z., F. Nadim, A. Garcia-Aristizabal, A. Mignan, K. Fleming and B. Q. Luna 2015. A three-level framework for multi-risk assessment, *Georisk: Assessment and Management of Risk for Engineered Systems and Geohazard*s 9:59-74, doi: 10.1080/17499518.2015.1041989.

Lorito, S., J. Selva, R. Basili, F. Romano, M.M. Tiberti and A. Piatanesi 2015. Probabilistic hazard for seismically induced tsunamis: accuracy and feasibility of inundation maps. *Geophys. J. Int.* 200:574–588, doi: 10.1093/gji/ggu408.

Loth, C. and J.W. Baker 2013. A spatial cross-correlation model of spectral accelerations at multiple periods. *Earthquake Engineering and Structural Dynamics* 42(3): 397–417.

Manyena, S.B., 2006. The concept of resilience revisited. Disasters, 30(4): 434–450.

Marzocchi W., M. Taroni and J. Selva 2015. Accounting for Epistemic Uncertainty in PSHA: Logic Tree and ensemble Modeling. *Bull. Seism. Soc. Am.* 105(4):2151–2159, doi: 10.1785/0120140131.

Marzocchi, W. and T.H. Jordan 2014. Testing for Ontological Errors in Probabilistic Forecasting Models of Natural Systems. *Proc. Nat. Acad. Sci.* 85:955-959.

Marzocchi, W., Ch. Newhall and G. Woo 2012. The scientific management of volcanic crises. *Journal of Volcanology and Geothermal Research* 247-248: 181-189.

Mashaly, E-SA and T.K. Datta 1989. Seismic risk analysis of buried pipelines. *Journal of transportation engineering* 115(3): 232-52.

Matos, J.P., A. Mignan and A.J. Schleiss 2015. Vulnerability of large dams considering hazard interactions: conceptual application of the Generic Multi-Risk framework, Proceedings of the 13th ICOLD International Benchmark Workshop on Numerical Analysis of Dams, Lausanne, Switzerland.

McDaniels, T. et al., 2008. Fostering resilience to extreme events within infrastructure systems: Characterizing decision contexts for mitigation and adaptation. Global Environmental Change, 18(2): 310–318.

McGuire R.K. 1988. *Seismic risk to lifeline systems: critical variables and sensitivities*. Proceedings of 9th World Conference on Earthquake Engineering, Tokyo-kyoto, Japan. pp 129-134

McGuire, R.K. 1976. *FORTRAN Computer Program for Seismic Risk Analysis*, USGS Open File Report 76-67.

Meijers, P., 2014. Effecten aardbevingen op kritische infrastructuur. Deltares Report 1208624-007. Delft, the Netherlands.

Mignan, A., L. Danciu, J.P. Matos and A. Schleiss 2015. *D3.5 – Report on cascading events and multi-hazard probabilistic scenarios*. STREST project: Harmonized approach to stress tests for critical infrastructures against natural hazards.

Mignan, A., N. Komendantova, A. Scolobig and K. Fleming. Multi-Risk Assessment and Governance, Handbook of Disaster Risk Reduction and Management, World Sci. Press & Imperial College Press, London (in press).

Mignan, A., S. Argyroudis and K. Pitilakis 2014a. *D2.4 – Report on lessons learned from on-going and completed EU project*s. STREST project: Harmonized approach to stress tests for critical infrastructures against natural hazards.

Mignan, A., S. Wiemer and D. Giardini 2014b. The Quantification of Low Probability-High Consequences Events: Part I. A Generic Multi-Risk Approach. *Natural Hazards* 73: 1999-2022, doi: 10.1007/s11069-014-1178-4.

Miraei, M. and Y. Jafarian 2013. Fragility curves for assessing the seismic vulnerability of gravity quay walls. *In COMPDYN 2013, In 4th ECCOMAS Thematic Conference on Computational Methods in Structural Dynamics and Earthquake Engineering* M. Papadrakakis, V. Papadopoulos, V. Plevris (eds.), Kos Island, Greece.

Miraglia, S., Courage, W., Meijers, P. 2015. Fragility functions for pipeline in liquefiable sand: a case study on the Groningen gas-network. In Haukaas, T. (Ed.) (2015). *Proceedings of the 12th International Conference on Applications of Statistics and Probability in Civil Engineering (ICASP12)*, Vancouver, Canada, July 12-15.

Mousavi, M., M. Hesari and A. Azarbakht 2014. Seismic risk assessment of the 3rd Azerbaijan gas pipeline in Iran. *Natural Hazards* 74(3):1327-48.

Musson, R.M.W. 1999. Determination of design earthquakes in seismic hazard analysis through Monte Carlo simulation. *Journal of Earthquake Engineering* 3(4): 463-474.

Musson, R.M.W., 2000. The use of Monte Carlo simulations for seismic hazard assessment in the UK. *Annali Di Geofisica* 43(1): 1–9.

Na, U. J. and M. Shinozuka 2009. Simulation-based seismic loss estimation of seaport transportation system. *Reliab Eng Syst Saf* 94(3): 722–731.

National Diet of Japan 2012. *The Official Report of the Fukushima Nuclear Accident Independent Investigation Commission, Executive Summary*. The National Diet of Japan, Tokyo. http://reliefweb.int/sites/reliefweb.int/files/resources/NAIIC_report_lo_res2.pdf (11 July 2014).

National Institute of Building Sciences (NIBS) 2004. *HAZUS-MH: user's manual and technical manuals*. Report prepared for the federal emergency management agency. National Institute of Building Sciences, Washington, DC.

National Institute of Standards and Technology (NIST) 2015. *Disaster resilience framework*. 75% Draft for San Diego, CA Workshop.

Neri, A., A. Bevilacqua, T. Esposti Ongaro, R. Isaia, W.P. Aspinall, M. Bisson, F. Flandoli, P.J. Baxter, A. Bertagnini, E. Iannuzzi, S. Orsucci, M. Pistolesi, M. Rosi and S. Vitale 2015. Quantifying volcanic hazard at Campi Flegrei caldera (Italy) with uncertainty assessment: 2. Pyroclastic density current invasion maps. *J. Geophys. Res. Solid Earth* 120:2330–2349, doi: 10.1002/2014JB011776.

Newmark, N.M., and W.J. Hall 1975. Pipeline Design to Resist Large Fault Displacement. *U.S. National Conference on Earthquake Engineering*, Ann Arbor, MI, pp. 416-425.

NRC, National Research Council Panel on Seismic Hazard Evaluation 1997. *Review of Recommendations for Probabilistic Seismic Hazard Analysis: Guidance on Uncertainty*

and Use of Experts. National Academy of Sciences, Washington, D.C., 84 pp., ISBN:0-309-56207-4.

O'Rourke, M. 2009. Analytical Fragility Relations for Buried Segmented Pipe. *Proc. of TCLEE 2009, Lifeline Earthquake Engineering in a Multihazard Environment*, ASCE, Oakland, CA, pp. 771-780.

O'Rourke, M. J. and G. Ayala 1993. Pipeline damage due to wave propagation. *Journal of Geotechnical Engineering,* 119:123-134.

O'Rourke, M. J., and X. Liu 1999. *Response of buried pipelines subjected to earthquake effects*. MCEER Monograph No.3. Buffalo, USA: University of New York.

O'Rourke, M.J. and X. Liu 2012. *Seismic design of buried and offshore pipelines*. MCEER Monograph MCEER-12-MN04,

O'Rourke, T., and S. Jeon 1999. Factors Affecting the Earthquake Damage of Water Distribution Systems. *In 5th U.S. Conference on Lifeline Earthquake Engineering*, TCLEE Monograph #16, ASCE, pp. 379-388.

O'Rourke, T.D., S.S. Jeon, S. Toprak, M. Cubrinovski, M. Huges, S. Ballegooy and D. Bouziou 2014. Earthquake Response of Underground Pipeline Networks in Christchurch, NZ. *Earthq Spectra*, 30(1): 183–204, DOI: 10.1193/030413EQS062M.

Obama, B., 2013. Presidential policy directive 21: Critical Infrastructure Security and Resilience. Available at: http://www.whitehouse.gov/the-press-office/2013/02/12/presidential-policy-directive-critical-infrastructure-security-and-resil.

Omidvar, B., M. Eskandari, E. Peyghaleh 2013. Seismic damage to urban areas due to failed buried fuel pipelines case study: fire following earthquake in the city of Kermanshah, Iran. *Natural Hazards* 67(2):169-92.

O'Rourke, M., E. Filipov, E. Uçkan 2014 Towards Robust Fragility Relations for Buried Segmented Pipe in Ground Strain Areas. *Earthquake Spectra*. doi: http://dx.doi.org/10.1193/032311EQS076M

Ouyang, M. & Dueñas-Osorio, L., 2012. Time-dependent resilience assessment and improvement of urban infrastructure systems. Chaos: An *Interdisciplinary Journal of Nonlinear Science* 22(3), p.33122.

Ouyang, M. et al., 2008. Emergency response to disaster-struck scale-free network with redundant systems. *Physica A: Statistical Mechanics and its Applications* 387(18): 4683–4691.

Ouyang, M. et al., 2009. Effects of redundant systems on controlling the disaster spreading in networks. Simulation Modelling Practice and Theory, 17(2), pp.390–397.

Ouyang, M., Dueñas-Osorio, L., Min, X., 2012. A three-stage resilience analysis framework for urban infrastructure systems. Structural Safety, 36, pp.23–31.

Oxstrand, J., Sylvander, C., 2010. Resilience engineering: Fancy talk for safety culture: A Nordic perspective on resilience engineering. In *3rd IEEE International Symposium on Resilient Control Systems*, Idaho Falls, ID, USA. pp. 135–137.

Pachakis, D. and Kiremidjian A. S. 2005. *Estimation of Downtime-Related Revenue Losses in Maritime Ports due to Earthquakes*. Blume Center Technical Report No. 146.

Pagani, M., D. Monelli, G. Weatherill, L. Danciu, H. Crowley and V. Silva 2014. OpenQuake Engine: An Open Hazard (and Risk) Software for the Global Earthquake Model. *Seismological Research Letters* 85(3):692-702.

Paté-Cornell, M.E. (1996). Uncertainties in risk analysis: Six levels of treatment. *Reliab. Eng. Syst. Saf.* 54:95–111.

PCCIP 1997. *Critical foundations: Protecting America's Infrastructures*. Report of the President's Commission on Critical Infrastructure Protection, Available from: http://www.fas.org/sgp/library/pccip.pdf.

Percher, M., 2014. Japan earthquake and tsunami of 2011: Survey of port and _arbour structures, Northern region, ASCE-COPRI Port and Harbor Facilities Survey Team, American Society of Civil Engineers.

Pescaroli, G. and D. Alexander 2015. *A definition of cascading disasters and cascading effects: Going beyond the "toppling dominos" metaphor*. In Planet@Risk, 2(3): 58-67, Davos: Global Risk Forum GRF Davos.

Petersen, M.D., T.E. Dawson, R. Chen, T. Cao, C.J. Wills, D.P. Schwartzand A.D Frankel. 2011. Fault displacement hazard for strike-slip faults. *Bulletin of the Seismological Society of America* 101(2): 805–825.

PIANC, 2001. Seismic design guidelines for port structures, World Association for Waterborne Transport Infrastructure.

Pineda-Porras O.A., and M. Ordaz 2012. Seismic Damage Estimation in Buried Pipelines Due to Future Earthquakes-The Case of the Mexico City Water System. *Earthquake-Resistant Structures - Design, Assessment and Rehabilitation-Chapter 5*. INTECH Open Access Publisher;

Pitilakis, K., H. Crowley and A. Kaynia (Eds) 2014a. *SYNER-G: Typology definition and fragility functions for physical elements at seismic risk. Buildings, lifelines, transportation networks and critical facilities.* Series title: Geotechnical, Geological and Earthquake Engineering, 27, Springer, Netherlands.

Pitilakis, K., P. Franchin, B. Khazai and H. Wenzel (Eds) 2014b. SYNER-G: Systemic seismic vulnerability and risk assessment of complex urban, utility, lifeline systems and critical facilities. Methodology and applications. Series: Geotechnical, Geological and Earthquake Engineering, 31, Springer, Netherlands.

Poljanšek, K., Bono, F., Gutiérrez, E., 2011. Seismic risk assessment of interdependent critical infrastructure systems: The case of European gas and electricity networks. *Earthquake Engineering and Structural Dynamics* 41(1):61-79.

Ramirez-Marquez, J.E., Rocco, C.M., 2012. Towards a Unified Framework for Network Resilience. In Proceedings of the CESUN 2012 International Engineering Systems Symposium, Delft, The Netherlands. pp. 18–20.

Rinaldi, S.M., Peerenboom, J.P., Kelly, T.K., 2001. Identifying, understanding, and analyzing critical infrastructure interdependencies. *IEEE Control Systems* 21(6), pp.11–25.

Rosato, V., L. Issacharoff, F. Tiriticco, S. Meloni, S. D. Porcellinis and R. Setola 2008. Modelling interdependent infrastructures using interacting dynamical models. *International Journal of Critical Infrastructures* 4: 63–79.

Rossetto, T., I. Ioannou and D. N. Grant 2013. *Existing empirical fragility and vulnerability relationships: compendium and guide for selection.* GEM technical report 2013-X, GEM Foundation, Pavia, Italy, April 2013, pp 62.

Rowshandel, B. 2013. *Rowshandel's NGA-West2 directivity model.* Report PEER Report 2013/09, Berkeley, Calif.: Pacific Earthquake Engineering Research Center, University of California.

Schmidt, J., I. Matcham, S. Reese, A. King, R. Bell, R. Henderson, G. Smart, J. Cousins, W. Smith and D. Heron 2011. Quantitative multi-risk analysis for natural hazards: a framework for multi-risk modelling. *Natiural Hazards* 58:1169–1192. doi: 10.1007/s11069-011-9721-z.

Selva, J. 2013. Long-term multi-risk assessment: statistical treatment of interaction among risks. *Natural Hazards* 67(2): 701-722, DOI:10.1007/s11069-013-0599-9.

Selva, J., A. Costa, W. Marzocchi and L. Sandri 2010. BET_VH: Exploring the influence of natural uncertainties on long-term hazard from tephra fallout at Campi Flegrei (Italy). *Bull. Volcanol.* 72(6):717–733, doi: 10.1007/s00445-010-0358-7.

Selva, J., M.I. Sarfraz, M. Taroni, W. Marzocchi, F. Cotton, W. Courage, L. Abspoel-Bukman, S. Miraglia, A. Mignan, K. Pitilakis, S. Argyroudis, K. Kakderi, D. Pitilakis, G. Tsinidis and C. Smerzini 2015. *D3.1 – Report on the effects of epistemic uncertainties on the definition of LP-HC events*. STREST project: Harmonized approach to stress tests for critical infrastructures against natural hazards.

Selva, J., R. Tonini, I. Molinari, M.M. Tiberti, F. Romano, A. Grezio, D. Melini, A. Piatanesi, R. Basili and S. Lorito (submitted). Quantification of source uncertainties in Seismic Probabilistic Tsunami Hazard Analysis (SPTHA).

Selva, J., S. Argyroudis and K. Pitilakis 2013. Impact on loss/risk assessments of inter-model variability in vulnerability analysis. *Nat. Hazards* 67:723–746.

Shahi, S., J.W. Baker 2011. An empirically calibrated framework for including the effects of near-fault directivity in probabilistic seismic hazard analysis. *Bulletin of the Seismological Society of America* 101(2): 742–755.

Shinozuka, M., M.Q. Feng, H.K. Kim, T. Uzawa and T. Ueda 2003. *Statistical analysis of fragility curves*. Technical Report MCEER-03-0002, State University of New York, Buffalo.

Smith, K. and D. Petley 2009. *Environmental Hazards. Assessing Risk and Reducing Disaster (5th edn)*. New York: Routledge.

Sokolov, V. and F. Wenzel 2011a. Influence of ground-motion correlation on probabilistic assessments of seismic hazard and loss: sensitivity analysis. *Bulletin of Earthquake Engineering* 9(5): 1339–1360.

Sokolov, V. and Wenzel, F. 2011b. Influence of spatial correlation of strong ground motion on uncertainty in earthquake loss estimation. *Earthquake Engineering and Structural Dynamics* 40(9): 993–1009.

Somerville, P.G., 2003. Magnitude scaling of the near fault rupture directivity pulse. *Physics of the Earth and Planetary Interiors* 137(1): 201–212.

Sørensen, M.B., M. Spada, A. Babeyko, S. Wiemer and G. Grünthal 2012. Probabilistic tsunami hazard in the Mediterranean Sea. *J. geophys. Res.* 117:B01305, doi: 10.1029/2010JB008169.

SRMLIFE 2007. Development of a global methodology for the vulnerability assessment and risk management of lifelines, infrastructures and critical facilities. Application to the metropolitan area of Thessaloniki. Research Project, General Secretariat for Research and Technology, Greece.

SSHAC, Senior Seismic Hazard Analysis Committee 1997. *Recommendations for Probabilistic Seismic Hazard Analysis: Guidance on Uncertainty and Use of Experts.* U.S. Nuclear Regulatory Commission, U.S. Dept. of Energy, Electric Power Research Institute; NUREG/CR-6372, UCRL-ID-122160, vol. 1-2.

SSHAC, Senior Seismic Hazard Analysis Committee 2013. *Practical Implementation Guidelines for SSHAC Level 3 and 4 Hazard Studies.* U.S. Nuclear Regulatory Commission; NUREG-2117, Revision 1.

Stafford, P.J., 2012. Evaluation of structural performance in the immediate aftermath of an earthquake: a case study of the 2011 Christchurch earthquake. *International Journal of*

Stepp, J.C., I. Wong, J. Whitney, R. Quittmeyer, N. Abrahamson, G. Toro, R. Youngs, K. Coppersmith, J. Savy and T. Sullivan 2001. Yucca Mountain PSHA Project Members. Probabilistic seismic hazard analyses for ground motions and fault displacement at Yucca Mountain, Nevada. *Earthquake Spectra* 17(1): 113–150.

Subotic, B., Ochieng, W.Y., Straeter, O., 2007. Recovery from equipment failures in {ATC}: Determination of contextual factors. *Reliability Engineering & System Safety* 92(7):858–870.

Suzuki K., 2002. Report on damage to industrial facilities in the 1999 Kocaeli earthquake, Turkey. *Journal of Earthquake Engineering*, 6(2): 275–296.

SYNER-G 2010-2014. Systemic Seismic Vulnerability and Risk Analysis for Buildings, Lifeline Networks and Infrastructures Safety Gain. European Collaborative research project (FP7/2007-2013). Available at: http://www.syner-g.eu.

The President's Commission on Critical Infrastructure Protection (PCCIP), 1997. Critical Foundations: Protecting America's Infrastructures.

Tomita T. and Yoem G., 2012. Tsunami damage in ports by the 2011 off Pacific Coast of Tohoku-Oki earthquake, In: *Proc. Int. Symposium on Engineering Lessons Learned from the 2011 Great East Japan Earthquake*, March 1-4, Tokyo, Japan.

Torkamani, H. H., K. Bargi, R. Amirabadi and N. J. McCllough 2014. Fragility estimation and sensitivity analysis of an idealized pile-supported wharf with batter piles. *Soil Dynamics and Earthquake Engineering* 61-62: 92–106.

Tothong, P., C.A. Cornell and J.W. Baker 2007. Explicit-directivity-pulse inclusion in probabilistic seismic hazard analysis. *Earthquake Spectra* 23(4): 867–891.

Trivedi, K.S., Kim, D.S., Ghosh, R., 2009. Resilience in computer systems and networks. In Proceedings of the 2009 ACM International Conference on Computer-Aided Design, San Jose, CA, USA. pp. 74–77.

Turnquist, M., Vugrin, E., 2013. Design for resilience in infrastructure distribution networks. *Environment Systems & Decisions*, pp.1–17.

Uckan, E., B. Akbas, J. Shen, W. Rou, F. Paolacci, and M. O'Rourke. 2015. A simplified analysis model for determining the seismic response of buried steel pipes at strike-slip fault crossings. *Soil Dyn Earthq Eng* 75: 55-65.

Van Breda, A.D., 2001. Resilience theory: A literature review. Pretoria, South Africa: South African Military Health Service.

Vazouras, P., S.A. Karamanos and P. Dakoulas 2012. Mechanical behavior of buried steel pipes crossing active strike-slip faults. *Soil Dynamics and Earthquake Engineering* 41:164-80.

Vazouras, P., S.A. Karamanos, P. Dakoulas 2010. Finite element analysis of buried steel pipelines under strike-slip fault displacements. *Soil Dynamics and Earthquake Engineering* 30(11):1361–76.

Villez, K. et al., 2010. Achieving resilience in critical infrastructures: A case study for a nuclear power plant cooling loop. *In Proceedings of the 3rd IEEE International Symposium on Resilient Control Systems*, Idaho Falls, ID, USA. pp. 49–52.

Vugrin, E.D., Camphouse, R.C., 2011. Infrastructure resilience assessment through control design. *International Journal of Critical Infrastructures* 7(3), pp.243–260.

Vugrin, E.D., Camphouse, R.C., Sunderland, D., 2009. Quantitative Resilience Analysis through Control Design, Sandia Report: SAND2009-5957, Unlimited Release, Printed September 2009.

Vugrin, E.D., Camphouse, R.C., Downes, P.S., et al., 2009. Measurement of System Resilience: Application to Chemical Supply Chains. In Proceedings of SIAM Conference on Mathematics for Industry: Challenges and Frontiers, San Francisco, CA, USA.

Vugrin, E.D., Turnquist, M.A., Brown, N.J.K., 2010. Optimal recovery sequencing for critical infrastructure resilience assessment, Technical Report SAND2010-6237. Albuquerque, NM: Sandia National Laboratories.

Vugrin, E.D., Turnquist, M.A., Brown, N.J.K., 2013. Optimal recovery sequencing for enhanced resilience and service restoration in transportation networks, *Int. Journal of Critical Infrastructures* 10(3/4):218-246.

Vyatkin, V. et al., 2010. Toward digital ecologies: Intelligent agent networks controlling interdependent infrastructures. In Proceedings of the First IEEE International Conference on Smart Grid Communications, Gaithersburg, MD, USA. pp. 589–594.

Wang, M. and T. Takada 2005. Macrospatial Correlation Model of Seismic Ground Motions. *Earthquake Spectra* 21(4):1137–1156.

Wang, Y., S. Au, Q. Fu 2010. Seismic risk assessment and mitigation of water supply systems. *Earthquake Spectra* 26(1): 257–74.

Weatherill, G., S. Esposito, I. Iervolino, P. Franchin and F. Cavalieri 2014. Framework for seismic hazard analysis of spatially distributed systems, in: K. Pitilakis et al. (eds). SYNER-G: Systemic seismic vulnerability and risk assessment of complex urban, utility, lifeline systems and critical facilities. Methodology and applications. Springer, Netherlands, 57-88.

Weatherill, G., V. Silva, H. Crowley and P. Bazzurro 2015. Exploring the impact of spatial correlations and uncertainties for portfolio analysis in probabilistic seismic loss estimation. *Bulletin of Earthquake Engineering* 13(4): 957-981.

Wells, D.L.1994. Coppersmith KJ. New empirical relationships among magnitude, rupture length, rupture width, rupture area, and surface displacement. *Bulletin of the Seismological Society of America* 84(4): 974–1002.

Wesson, R.L. and D.M. 2001. Perkins Spatial correlation of probabilistic earthquake ground motion and loss. *Bulletin of the Seismological Society of America* 91(6): 1498-1515.

Whitson, J.C., Ramirez-Marquez, J.E., 2009. Resiliency as a component importance measure in network reliability. *Reliability Engineering & System Safety* 94(10): 1685–1693.

Youngs, R.R., W.J. Arabasz, R.E. Anderson, A.R. Ramelli, J.P. Ake, D.B. Slemmons, J.P. McCalpin, D.I. Doser, C.J. Fridrich, III. FH. Swan, A.M. Rogers, J.C. Yount, L.W.Anderson, K.D. Smith, R.L. Bruhn, L.K. Knuepfer, R.B. Smith, C.M. dePolo,. K.W. O'Leary, K.J. Coppersmith, S.K. Pezzopane, D.P. Schwartz, J.W. Whitney, S.S. Olig and G.R. Toro 2003. A methodology for probabilistic fault displacement hazard analysis (PFDHA). *Earthquake Spectra* 19(1): 191–219.

Youngs, R.R., W.J. Arabasz, R.E. Anderson, A.R. Ramelli, J.P. Ake, D.B. Slemmons, et al. 2013. A methodology for probabilistic fault displacement hazard analysis (PFDHA). *Earthquake Spectra* 19(1):191-219.